2017

Novel Photonic Resonance Arrangements Using Non-Hermitian Exceptional Points

Hossein Hodaei
University of Central Florida

NOVEL PHOTONIC RESONANCE ARRANGEMENTS USING NON-HERMITIAN EXCEPTIONAL POINTS

by

HOSSEIN HODAEI

B.S. Isfahan University of Technology, 2011
M.S. Sharif University of Technology, 2013
M.S. University of Central Florida, 2016

A dissertation submitted in partial fulfillment of the requirements
for the degree of Doctor of Philosophy
in CREOL/The College of Optics & Photonics
at the University of Central Florida
Orlando, Florida

Spring Term
2017

Major Professor: Mercedeh Khajavikhan

ABSTRACT

In recent years, non-Hermitian degeneracies also known as exceptional points (EPs) have emerged as a new paradigm for engineering the response of optical systems. EPs can appear in a wide class of open non-Hermitian configurations. Among different types of non-conservative photonic systems, parity-time (PT) symmetric arrangements are of particular interest since they provide an excellent platform to explore the physics of exceptional points. In this work, the intriguing properties of exceptional points are utilized to address two of the long standing challenges in the field of integrated photonics- enforcing single mode lasing in intrinsically multimode cavities and enhancing the sensitivity of micro-resonators.

In the first part of this work, I will describe how stable single mode lasing can be readily achieved in longitudinally and transversely multi-moded microring cavities through the systematic utilization of abrupt phase transitions at exceptional points. This technique will be first demonstrated in a parity-time laser that is comprised of a gain cavity coupled to an identical but lossy counterpart. A detailed study of the behavior of this system around the exceptional point will be presented. Furthermore, we report the first experimental realization of a dark state laser in which by strategically designing the spectral locations of exceptional points, widely tunable single-mode lasing can be attained even at high pump levels. Despite the presence of loss in such open laser systems, the slope efficiency remains virtually intact. Our results demonstrate the potential of exceptional points as a versatile design tool for mode management in on-chip laser configurations.

In the second part of my dissertation, I will show how the exceptional points and their underlying degeneracies can be used to significantly boost the intrinsic sensitivity of microcavities. I will demonstrate the enhanced sensitivity in a binary PT-symmetric coupled cavity arrangement that is biased at an exceptional point. Then I will report the first observation of higher-order exceptional points in a ternary parity-time symmetric microring laser system with a judiciously tailored gain-loss distribution. The enhanced response associated with this ternary system follows a cubic root dependence on externally introduced perturbation, which can in turn be detected in the spectral domain. Using such arrangements, more than one order of magnitude enhancement in the sensitivity is observed experimentally. These results can pave the way towards improving the performance of current on-chip micro-cavity sensors.

To Fatemeh.

ACKNOWLEDGMENTS

Firstly, I would like to express my earnest gratitude to my advisor Prof. Khajavikhan for her continuous support throughout my PhD, for her patience, motivation, trust, and knowledge. Her guidance made my years at CREOL the most educative and rewarding.

Besides my advisor, I would like to thank Prof. Christodoulides, who I had the great opportunity to work with and learn a lot from.

I would like to thank the rest of my thesis committee Professors LiKamWa and Abdolvand for their insightful comments, help, and encouragement.

Also thanks to my fellow colleagues and friends: Billy, Absar, Amin, Polo, Steffen, Mydia, Jinhan, Enrique, Matthias, Ali, and many others who helped to make a friendly and collaborative research environment.

Last but not the least, I would like to thank my family: my wife, my parents, and my brothers for supporting me spiritually during my PhD and my life in general.

TABLE OF CONTENTS

LIST OF FIGURES

CHAPTER 1: INTRODUCTION

Non-Hermitian degeneracies, also known as exceptional points (EPs) represent singularities in parameter space where the eigenvalues involved and their corresponding eigenstates tend to simultaneously coalesce [1]–[4]. In the last decade, the physics and properties of such degeneracies have been intensively studied particularly as a result of the emergence of PT-symmetric configurations in optics [5]. In this regard, the abrupt nature of the phase transitions encountered around EPs has been shown to lead to a number of intriguing and counter-intuitive phenomena such as loss-induced transparency [6], unidirectional invisibility [7]–[10], band merging [5], [11], [12], and topological chirality [13], [14], to mention a few. In this work, we used these non-Hermitian degeneracies to address some of the existing challenges in the on-chip micro-cavity lasers and sensing applications. This dissertation contains two main segments; first we show that the properties associated with the exceptional points can be utilized as an effective design tool to obtain desired functionalities like single mode operation in integrated semiconductor microring laser systems, and second we demonstrate that the sensitivity of PT-symmetric micro-cavity arrangements to external perturbations can be dramatically enhanced by exploiting the physics of EPs.

Microring resonators exhibit several attractive features such as high Q-factors, small footprints, and simplicity of fabrication [15]–[18]. These qualities make them a promising candidate for on-chip laser sources. However, despite their small size, microrings tend to support several modes with comparable quality factors. The ensuing multi-mode operation

compromises the coherence and spectral purity of the laser, which in turn can cause power fluctuation and instability. In this respect, controlling the modal content of laser cavities has been a long standing challenge in laser science and engineering [19], [20]. This problem becomes particularly acute in semiconductor laser arrangements where the gain spectrum is rather broad [21] and thus multimode operation is inevitable. During the years, a number of schemes have been proposed to enforce single mode behavior in semiconductor laser systems. These include the use of external cavities [22]–[25] and intra-cavity dispersive elements [26]–[30], specially modulating the pump [31], or by extreme confinement of light in sub-wavelength structures using metallic cavities [32]–[34]. However, implementing such techniques can sometimes become exceedingly demanding, especially in micro-scale monolithically integrated lasers. Thus, devising alternative methods for mode management in integrated settings is of great importance.

Due to their small size and high quality factor, micro-cavities have also been employed as on-chip sensors in various configurations [35], [36]. Perturbing such resonance structures through an external effect can induce a shift or splitting of the corresponding eigenvalues- something that can be exploited for detection purposes. In Hermitian settings, like single-resonator optical gyroscopes [37] and microcavity sensors [35], [38], the induced separation in the eigen-spectrum is at most of the same order as the perturbation ϵ itself (where $|\epsilon| \ll 1$). This type of response is typically manifested in shifting of the resonance frequencies via index or gain variations. In recent years, there has been a growing realization that non-conservative systems operating around degeneracies or exceptional points can

provide a new avenue towards enhanced sensing capabilities [39]. In such configurations, the eigenfrequency splitting can be accentuated by orders of magnitude given that it follows a $\epsilon^{\frac{1}{N}}$-dependence, where N represents the order of the exceptional point involved. In general, the dimensionality of an EP is determined by the number of eigenvalues that simultaneously coalesce at this point. What makes this class of singularities so reactive to variations is the fact that in addition to the eigenvalues, all the corresponding eigenvectors also tend to merge at this point in parameter space. In essence, around EPs, the system suddenly loses dimensionality because the vector space becomes severely skewed. Given the dependency on $\epsilon^{\frac{1}{N}}$, it is clear that the sensitivity of the system will increase with the order of the exceptional point used- a property highly desirable in detection applications.

In this dissertation, PT-symmetric coupled resonator arrangements are proposed, fabricated, and characterized using a InP-based semiconductor gain platform. Mode management techniques based on the physics of exceptional points are successfully employed to achieve single mode operation at high pump powers. Furthermore, the enhanced sensitivity associated with second and third order exceptional points is demonstrated in binary and ternary PT-symmetric photonic molecules. In this regard, the structure of this document is as follows. Chapter 2 provides a brief introduction to PT-symmetry in the realm of optics and photonics. In chapter 3, some of the main aspects of microring resonators are discussed, and the dynamics of the energy transfer between two coupled microrings is investigated. In chapter 4, the PT-symmetric dual microring laser arrangement is introduced, and details of different operation regimes along with the design

considerations are presented. Longitudinal and transverse mode selection in such PT-symmetric lasers is studied in chapter 5. Chapter 6 proposes a potential approach to improve the modulation speed of PT-symmetric semiconductor lasers based on the notion of exceptional points. In chapter 7, a theoretical model of the dark state laser along with the experimental demonstration of single mode lasing and wide-range wavelength tuning in this structure is provided. In chapter 8, the response of binary and ternary PT-symmetric photonic molecules to external perturbations and the associated enhanced sensitivities are investigated when the systems are biased at their exceptional points. The details of techniques used for the fabrication and characterization processes are provided in chapter 9. Finally, chapter 10 concludes this work.

CHAPTER 2: PARITY-TIME (PT) SYMMETRY IN OPTICS

In 1998, it was discovered that a wide class of non-Hermitian Hamiltonians can exhibit entirely real eigenvalues if they commute with the parity-time ($\hat{P}\hat{T}$) operator [40]. To some extent, this counterintuitive result is against the commonly held view that real eigenvalues are only associated with Hermitian observables [4]. Starting from the aforementioned premise, one can directly show that a necessary (but not sufficient) condition for PT symmetry to hold is that the complex potential involved in such a Hamiltonian should satisfy $V(x) = V^*(-x)$ [40]–[44]. In other words, the real part of the complex potential must be an even function of position, while the imaginary must have an odd spatial distribution. In such configurations the eigenfunctions are no longer orthogonal, i.e., $\langle m|n\rangle \neq \delta_{mn}$, and hence the vector space is skewed. Even more intriguing is the possibility for a sharp symmetry-breaking transition once a non-Hermiticity parameter exceeds a certain critical value [40]. In this latter regime, the Hamiltonian and the $\hat{P}\hat{T}$ operator no longer display the same set of eigenfunctions (even though they commute) and as a result the eigenvalues of the system are no longer entirely real. More importantly, this broken PT-symmetry phase is associated with the appearance of the so-called exceptional points [45].

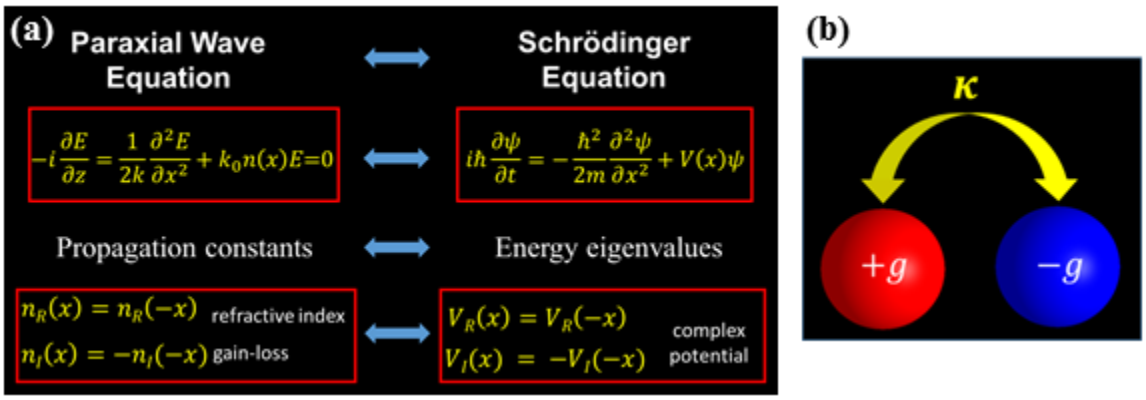

Figure 1. (a) Isomorphic relations between the Schrödinger equation and the paraxial equation in optics (b) Schematic of a binary PT-symmetric system.

While the implications of these mathematical theories are still a matter of debate (since the realization of complex potentials in quantum mechanics is inherently out-of-reach), it has been recently recognized that photonics can provide a fertile ground where PT symmetry concepts can be experimentally investigated [5]. The transition from quantum mechanics to optics can be formally justified by considering the isomorphism between the Schrödinger equation and the paraxial wave equation (see Fig. 1(a)). In this regard, the complex refractive index profile plays the role of an optical potential, *i.e.* $V(x)=k_0(n_R(x)+in_I(x))$. In optical systems, PT symmetry demands that the spatial distribution of the refractive index is an even function ($n_R(x)=n_R(-x)$), whereas the imaginary component (representing gain or loss) is an odd function of position ($n_I(x)=-n_I(-x)$). One can also show that in high contrast settings, where the electrodynamic problem must be treated fully vectorially, the condition for PT symmetry is expressed through the complex permittivity, *e.g.* $\varepsilon(\boldsymbol{r})=\varepsilon^*(-\boldsymbol{r})$ [46]. Nonetheless, since in most systems the imaginary part of the

complex refractive index function is considerably smaller than its real counterpart, the PT condition in these two scenarios is almost equivalent.

To elucidate some of the physics of exceptional points, we here provide a simple example of such a non-Hermitian PT-symmetric arrangement: a binary PT-symmetric system. For example, in optics this can describe two coupled resonators or waveguides, one exhibiting gain while the other experiences an equal amount of loss. In the case of two cavities, energy exchange occurs in time, while for a coupled waveguide arrangement, it takes place in space. A schematic of such a configuration is depicted in Fig. 1(b). In the case of two identical coupled single mode resonators, the field evolution dynamics can be described by:

$$\begin{cases} i\frac{da}{dt} - i\frac{g}{2}a + \kappa b = 0 \\ i\frac{db}{dt} + i\frac{g}{2}b + \kappa a = 0 \end{cases}. \qquad (2.1)$$

Here a and b represent the modal field amplitudes in the gain and loss cavities, respectively, g stands for the gain/loss coefficient, and κ is the coupling strength. This system supports two supermodes with distinct characteristics depending on the ratio between gain/loss (g) and coupling (κ). When $g/2\kappa < 1$, the two eigenvalues are real and are given by $\lambda_{1,2} = \pm\cos(\theta)$ where $\theta = sin^{-1}(g/2\kappa)$ and the corresponding eigenvectors are $|1\rangle = [1 \quad e^{i\theta}]^T$ and $|2\rangle = [1 \quad -e^{-i\theta}]^T$. Note that these eigenvectors are not orthogonal in spite of the fact that the spectrum is real. In this case, neither of the two modes experiences a net gain or loss *i.e*. they remain neutral, and hence they oscillate.

On the other hand, the characteristics of the supermodes drastically change as soon as the gain-loss contrast exceeds the coupling strength ($g/2\kappa > 1$). In this regime, the

eigenvalues are expressed by $\lambda_{1,2} = \pm\sinh(\theta)$ where $\theta = cosh^{-1}(g/2\kappa)$, and their corresponding non-orthogonal eigenvectors turn out to be $|1\rangle = [1 \quad ie^{\theta}]^T$ and $|2\rangle = [1 \quad ie^{-\theta}]^T$, indicating that the symmetry of each mode is broken such that one of them resides mostly in the gain cavity while the other one inhabits the lossy resonator. As a result, one of the eigenmodes enjoys amplification whereas the other experiences attenuation. Obviously, the supermode that mostly occupies the gain/loss region is amplified/attenuated. Figure 2 displays the complex eigenvalues as a function of $g/2\kappa$.

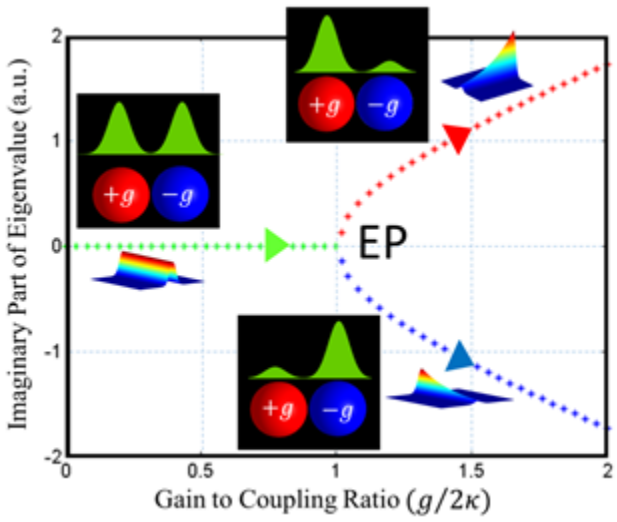

Figure 2. The imaginary part of the eigenvalue with respect to the gain/loss to coupling ratio for a PT-symmetric binary system. Beyond the exceptional point (PT-symmetry breaking point), one of the supermodes experiences amplification, while the other attenuation.

The transition point ($g/2\kappa = 1$) between these two different regimes is called the exceptional point, or EP. At this crossing, the dimensionality of the vector space is abruptly reduced from 2 to 1. This is evident from the fact that the two eigenvectors become entirely identical $[1 \quad i]^T$ and neither oscillate nor vary exponentially.

The above example demonstrates the role that the exceptional points can play in controlling light transport. Initial theoretical and experimental works carried out by several groups indicate that light propagating through non-Hermitian or PT-synthetic media can exhibit surprisingly unusual behavior [6]–[10], [5], [12], [42], [45], [47]–[67]. Among the numerous properties that such systems can display are: absorption enhanced transmittivity, unidirectional invisibility, double refraction, and band-merging. Most of these arrangements are designed to exploit the abrupt transitions at their associated exceptional points in order to achieve the desired functionalities.

CHAPTER 3: MICRORING RESONATORS

Microring resonators possess several interesting features like high quality factors, small footprints, and simplicity of fabrication. Therefore, they are one of the popular components in many integrated photonic devices such as sensors [35], [36], [38], modulators [68]–[70], filters [71]–[73], etc. Furthermore, the reflection-free nature of these cavities makes them an ideal choice for laser applications. In the first part of this chapter, we provide a study of spatial and temporal modal content of ring resonators utilized in our work. These microrings are comprised of six InGaAsP quantum wells in their high contrast active region and surrounded by low index dielectrics, i.e. SiO_2 and air. In the second section, the dynamics of energy transfer between two adjacent identical microrings is characterized using continuous wave coupled mode analysis.

3.1. Modal content of a microring resonator

A schematic and the cross-section of the microring cavity used in our experiments is shown in Fig. 3. The height of the waveguide is determined by the thickness of quantum well layers and it is set to be 210 nm. The width of the waveguide is designed to be 500 nm in most of our experiments to insure single transverse mode behavior. Figure 4 depicts the electric field amplitude for transverse electric (TE) and transverse magnetic (TM) polarizations in this structure, which is obtained by COMSOL finite element simulations. The interaction of the TM modes with the active region is negligible due to their very low confinement and also the orientation of the quantum wells, hence these modes are extraneous in our analyses and

experiments. On the other hand, the TE polarized modes have a considerable overlap with the active region and consequently enjoy a much lower lasing threshold.

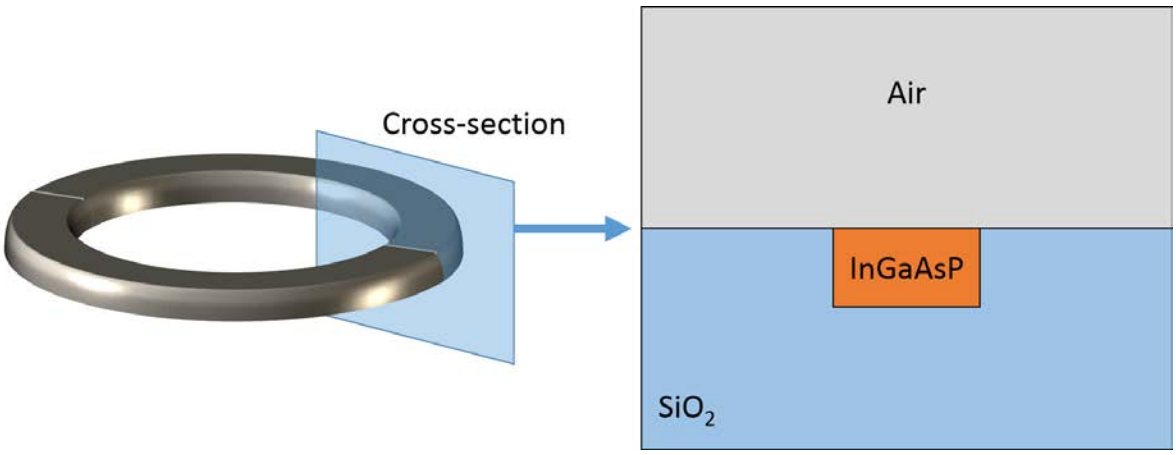

Figure 3. A schematic of the microring resonator used in this work along with its cross-section.

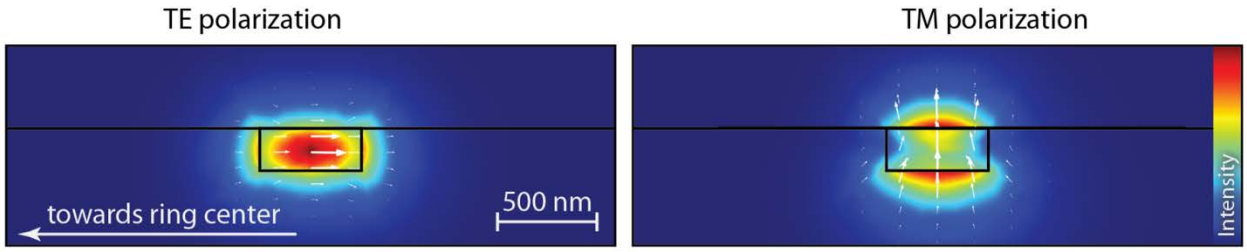

Figure 4. Field amplitude of the TE and TM polarizations in a single transverse mode waveguide. The overlap of the mode with the active guiding region is much larger in the TE case.

Every spatial mode of the waveguide is associated with a series of longitudinal resonance modes in the ring. In a passive cavity, the linewidth of these resonances is only determined by the quality factor. However, the resonance linewidth is a more complicated function of the Q-factor, output power, modal confinement, and nonlinearities in a lasing cavity. Different longitudinal modes are separated in the spectral domain by the free spectral

range or FSR ($\Delta\omega$) of the resonator. In the following, an analytical method is presented to find this value for a microring resonator with a radius of R and a refractive index of $n_{eff} = n(\omega)$ (Fig. 5).

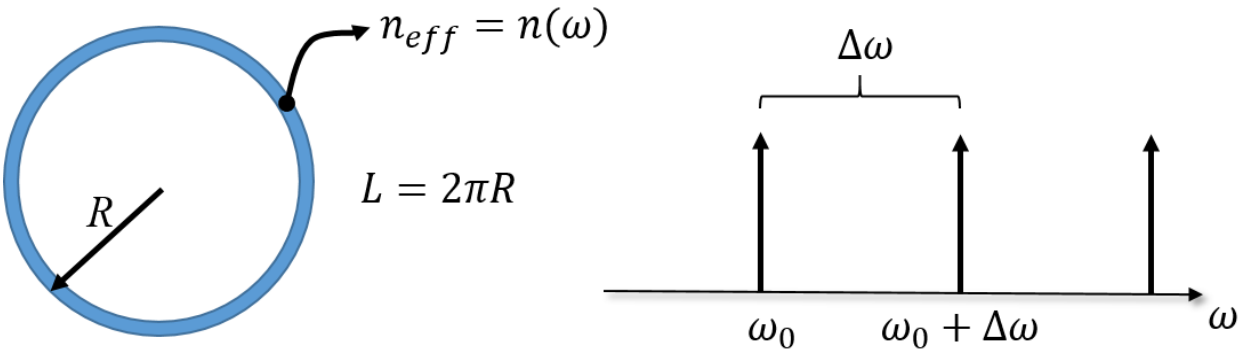

Figure 5. A 2D schematic of a microring resonator with a radius of R, and a dispersive effective refractive index of $n(\omega)$ along with its spectrum showing the FSR of $\Delta\omega$.

The propagation constant for the microring shown in Fig. 5 can be written as $\beta = \omega n(\omega)/c$. Using this expression one can simply find the group index of the structure to be:

$$n_g = \mathrm{c}\frac{d\beta}{d\omega} = n(\omega) + \omega\frac{dn(\omega)}{d\omega} \qquad (3.1)$$

On the other hand, any longitudinal resonance must satisfy the phase condition in the cavity, i.e. $\beta L = 2m\pi$. Therefore, for two subsequent longitudinal modes, one can write,

$$\frac{\omega_0 n(\omega_0)}{c} L = 2m\pi \qquad (3.2)$$

and

$$\frac{(\omega_0+\Delta\omega)n(\omega_0+\Delta\omega)}{c} L = 2(m+1)\pi \qquad (3.3)$$

By subtracting Eq. (3.2) from Eq. (3.3) and substituting $n(\omega_0 + \Delta\omega)$ by its Taylor series expansion around ω_0, one can find,

$$\frac{(\omega_0+\Delta\omega)(n(\omega_0)+\frac{dn}{d\omega}\Delta\omega)-\omega_0 n(\omega_0)}{c} L = 2\pi \qquad (3.4)$$

$\Delta\omega$ is simply derived from Eq. (3.4) to be,

$$\Delta\omega = {}^{2\pi c}/_{L} \times \frac{1}{n(\omega_0)+\omega_0\frac{dn}{d\omega}}. \qquad (3.5)$$

As indicted in Eq. (3.1), the denominator of Eq. (3.5) in fact represents the group velocity of the waveguide. In this respect, the expression for the FSR of a ring resonator is given by,

$$\Delta\omega = {}^{2\pi c}/_{L n_g}. \qquad (3.6)$$

The group index and effective index of the fundamental TE mode of the arrangement shown in Fig. 4 is plotted in Fig. 6 for the range of wavelengths from 1500 to 1600 nm. While the effective index acquires a value around 2.5, the group index of such a structure is approximately 4. This translates to a FSR of ~10 nm for a microring with an outer radius of 10 μm.

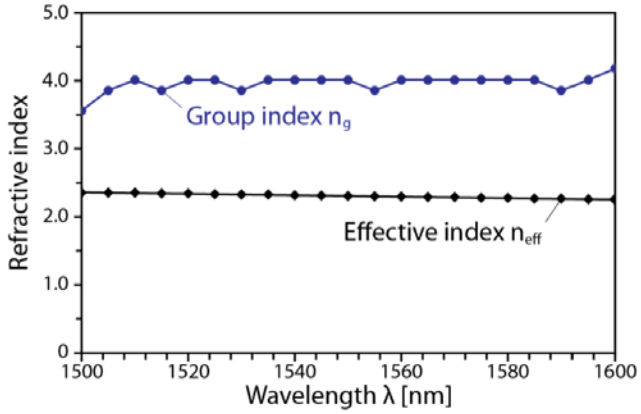

Figure 6. The group index and effective refractive index of a waveguide with a width of 500 nm and a height of 210 nm.

When higher order transverse modes are desired, the width of the ring's cross-section can be increased. In this study, the width of the transversely multi-moded microrings is chosen to be 1.5 μm. This way, the structure can support three distinct spatial resonant modes. Figure 7(a) shows the corresponding mode profiles in the cross-section of a ring with outer radius of 6 μm. Surprisingly, the peak of the mode is shifted towards the ring's center as a result of the curvature. However, the confinement still decreases for higher order transverse modes. The resonance wavelength of the associated longitudinal resonances are depicted in Fig. 7(b) for the wavelength range from 1520 to 1610 nm. Note that these resonance wavelengths are approximately calculated via finite element method, and their value can change in the order of a couple of nanometers by slight variations of the refractive indices of the involved materials.

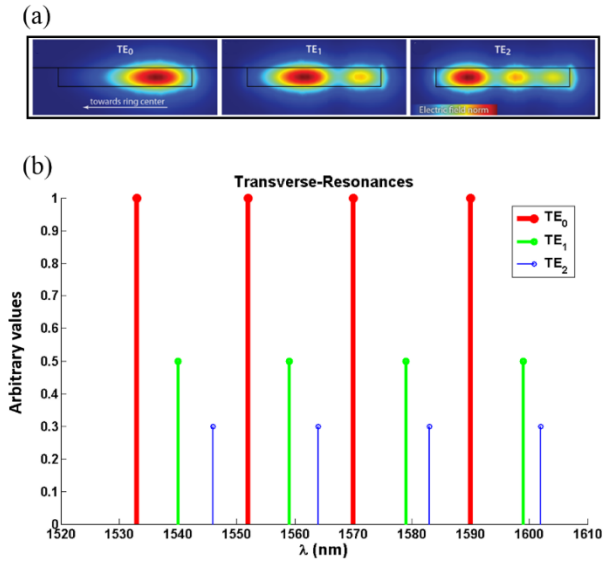

Figure 7. (a) Mode profiles of different spatial resonances in a microring resonator with a radius of 6 μm and width of 1.5 μm. (b) The wavelength resonances of longitudinal resonances associated with the three different spatial distributions shown in (a).

3.2. Energy transfer dynamics between two coupled microrings

In this section we employ spatial coupled mode analysis to investigate the dynamics of energy transfer between two coupled microrings. Moreover, we provide the results of experimental characterization of the coupling factors. This value can be extracted from the lasing spectrum of two adjacent rings when they are both pumped.

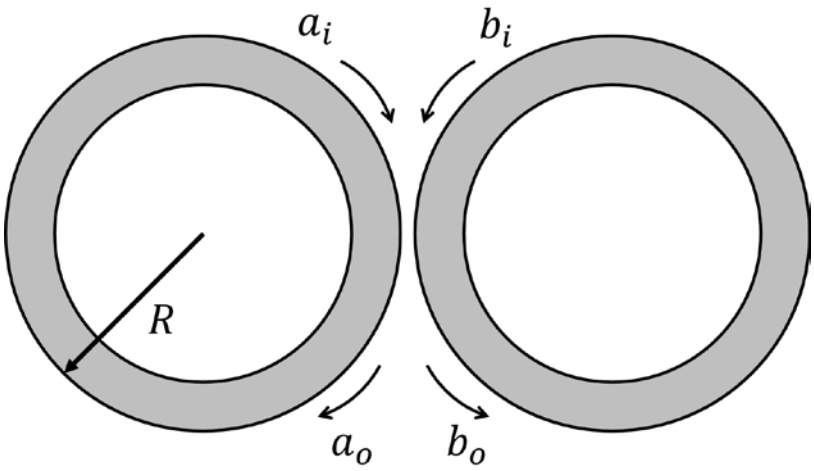

Figure 8. Two coupled microrings. The coupling region can be treated as a phase matched directional coupler with length of l_{eff} and spatial coupling constant of K.

A schematic representing a dual coupled microring structure is depicted in Fig. 8 in which two identical, passive, and transversely-single-mode resonators of radius R, are evanescently coupled to each other. The field distribution in the two rings can then be described via a system of spatial coupled mode equations. Here, we assume that the coupling strength is approximately constant over an effective coupling distance l_{eff}- locally it can be treated as a phase-matched directional coupler. Therefore, the modal amplitudes in the two cavities ($a(z)$ and $b(z)$) within the coupling region are governed by the following relations,

$$\begin{cases} a_o = a_i \cos\left(\mathrm{K}l_{eff}\right) + ib_i \sin(\mathrm{K}l_{eff}) \\ b_o = ia_i \sin\left(\mathrm{K}l_{eff}\right) + b_o \cos(\mathrm{K}l_{eff}) \end{cases} \quad (3.7)$$

where K represents the spatial coupling constant which is a function of the field overlap between the two resonators. Similarly, light propagation in the closed path of the two resonators demands that

$$\begin{cases} a_i = a_o \exp(i\phi) \\ b_i = b_o \exp(i\phi) \end{cases} \quad (3.8)$$

where $\phi = \omega n_{eff} L/c$ is the accumulated phase of the mode in one round trip. In this equation, ω is the resonance frequency, n_{eff} is the effective refractive index of the mode, $L = 2\pi R$ is circumference of the ring, and c is the speed of light in the vacuum. Using (3.7) and (3.8), one can show that:

$$\begin{pmatrix} -1+\exp(i\phi)\cos(\mathrm{K}l_{eff}) & i\exp(i\phi)\sin(\mathrm{K}l_{eff}) \\ i\exp(i\phi)\sin\left(\mathrm{K}l_{eff}\right) & -1+\exp(i\phi)\cos(\mathrm{K}l_{eff}) \end{pmatrix} \times \begin{pmatrix} a_o \\ b_o \end{pmatrix} = 0 \quad (3.9)$$

In order for this system to have nontrivial solutions, the determinant of the matrix in Eq. (3.9) should be equal to zero. This leads to

$$\cos(\phi) = \cos\left(Kl_{eff}\right). \quad (3.10)$$

The above equation can be solved to directly find the resonant frequencies of the system. In this case, one can simply find ϕ to be

$$\phi = \frac{\omega n_{eff} L}{c} = 2m\pi \pm \mathrm{K}l_{eff} \quad (3.11)$$

Here, different values of m represent different longitudinal modes, while the term $\mathrm{K}l_{eff}$ determined the mode splitting due to the coupling induced breaking of the degeneracy. The frequency splitting is twice the temporal coupling strength and can be derived from Eq. (3.11) to be,

$$\delta\omega = 2\kappa = \frac{2\mathrm{K}l_{eff}c}{n_{eff}2\pi R} \qquad (3.12)$$

From (3.11) and (3.12), one can infer that the maximum achievable coupling between two resonator in time domain is $\kappa_{max} = \Delta\omega_{FSR}/4$. This scenario occurs when the total amount of light entering the coupling region is transferred from one ring into the adjacent cavity, i.e. $\mathrm{K}l_{eff} = \pi/2$.

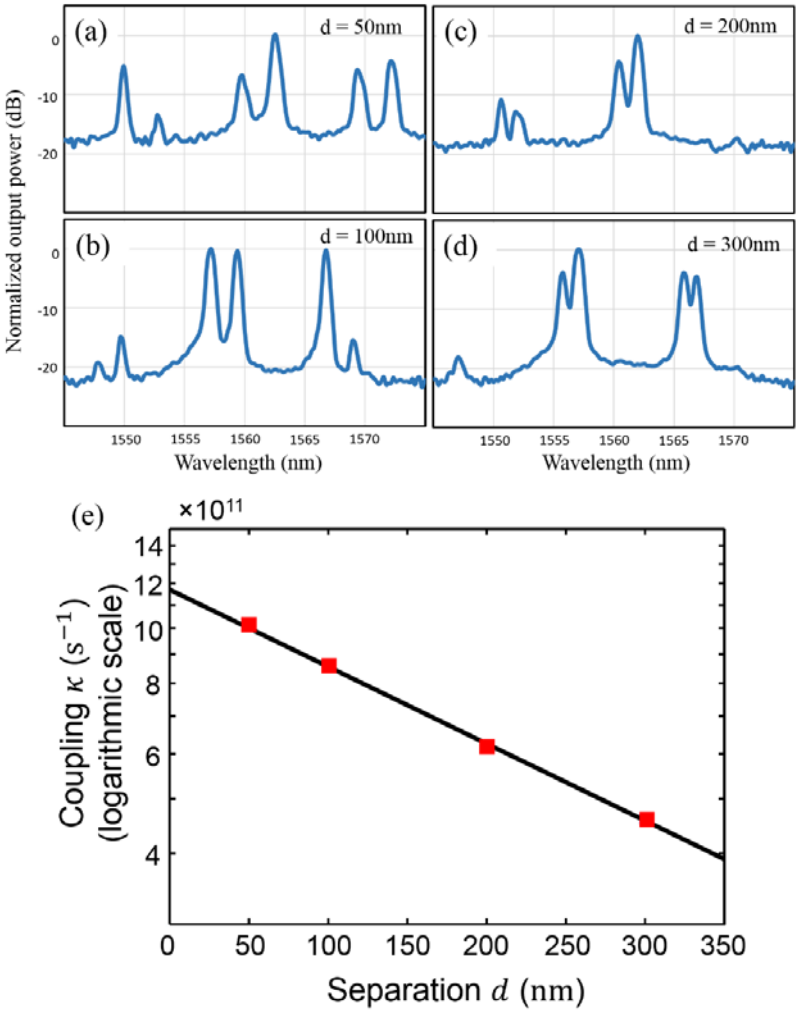

Figure 9. (a)–(d) Lasing spectra from evenly pumped microring pairs with separations of 50, 100, 200, and 300 nm, respectively. (e) The coupling coefficient depends exponentially on the separation distance between the two rings. The resolution of the spectrometer is set at 0.4 nm.

The coupling factor between dual cavities with different separation are experimentally characterized through the splitting of the corresponding lasing modes in the spectral domain, when both rings are evenly pumped. The results of this measurements are shown in Fig. 9. From Eq. (3.12), one can easily find $\delta\lambda = \kappa\lambda^2/\pi c$. Figures 9(a)–9(d) show the lasing spectra for a system of two coupled microrings separated by 50, 100, 200, and 300 nm, respectively. As expected, the wavelength splitting (coupling strength) monotonically decreases as the distance between the two rings is increased. Figure 9(e) confirms the exponential dependence of the coupling factor with respect to the spacing between the rings. For the rings separations at hand, coupling strengths on the order of $\sim 10^{12}\ s^{-1}$ are obtained, which is in agreement with simulation results.

CHAPTER 4: PT-SYMMETRIC COUPLED MICRORING LASERS

Coupled micro-resonators provide a viable platform to explore the physics and applications of parity-time symmetry in optics [9], [61]. In a coupled micro-cavity arrangement, PT-symmetry can be realized if one resonator is subject to gain while the other experiences an equal amount of loss. In this section, we employ the temporal coupled mode theory to present a linear analysis of this system. Through this method, we can show the modal behavior in parameter space and the dynamics of emergence of exceptional points. Using the same analysis, we study the lasing threshold in terms of different parameters of the PT-laser. We also present a qualitative nonlinear analysis of the system to study the effects of gain clamping and saturation above lasing threshold. The results in this chapter have been published in [74] and [75].

4.1. PT-symmetric coupled microring laser operating around an EP

A schematic representing such a dual cavity structure and an SEM image of the structure in an intermediate fabrication section are depicted in Fig. 10. Considering a pair of identical microring resonators, each of them supports a number of modes throughout the amplification bandwidth. The coupling between the two rings is dictated by the mutual overlap of their respective modal fields at the interaction region. In this study, the rings' dimensions and index contrast are selected so as to support a single transverse mode and to also favor the TE polarization as discussed in chapter 3. In the time domain, the interplay between the n^{th} longitudinal modes in the two rings obeys a set of two coupled differential

equations for their respective modal amplitudes a_n , b_n. By considering the n^{th} longitudinal mode in these two rings, one finds that

$$\begin{cases} \frac{da_n}{dt} = -i\omega_n a_n + i\kappa_n b_n + \gamma_{a_n} a_n \\ \frac{db_n}{dt} = -i\omega_n b_n + i\kappa_n a_n + \gamma_{b_n} b_n \end{cases} \quad (4.1)$$

where $\gamma_{a_n}$and γ_{b_n}represent the net gain (positive) or loss (negative) in each ring and ω_n is the n^{th} longitudinal resonance frequency of an isolated passive ring. Assuming an evolution of the form $(a_n, b_n) = (A_n, B_n)^{-i\omega_n t}$, the eigenfrequencies $\omega_n^{(1,2)}$ of the two supermodes of this system are given by

$$\omega_n^{(1,2)} = \omega_n + i\frac{\gamma_{a_n}+\gamma_{b_n}}{2} \pm \sqrt{\kappa_n^2 - \left(\frac{\gamma_{a_n}-\gamma_{b_n}}{2}\right)^2}. \quad (4.2)$$

When both rings are subject to the same level of gain or loss ($\gamma_{a_n} = \gamma_{b_n}$), Eq. 3 reveals that the real parts of the eigenfrequencies split by $2\kappa_n$, while their imaginary components remain degenerate. According to Eq. (4.2), an interesting situation arises when one of the rings is subject to gain, while the other one to the same amount of loss ($\gamma_{b_n} = -\gamma_{a_n}$). In this case, depending on the relationship between the strength of coupling ($2\kappa_n$) and the gain-loss contrast ($|\gamma_{a_n} - \gamma_{b_n}|$), the splitting either takes place in the real domain or along the imaginary axis. In particular, when the gain-loss contrast between the rings exceeds the coupling ($|\gamma_{a_n} - \gamma_{b_n}| \geq 2\kappa_n$), the real parts of the eigenfrequencies coalesce while the imaginary components lose their degeneracy. The point at which the two eigenfrequencies and their respective eigenvalues fuse ($|\gamma_{a_n} - \gamma_{b_n}| = 2\kappa_n$) is better known as an exceptional point and marks the threshold for parity-time symmetry breaking [5], [47].

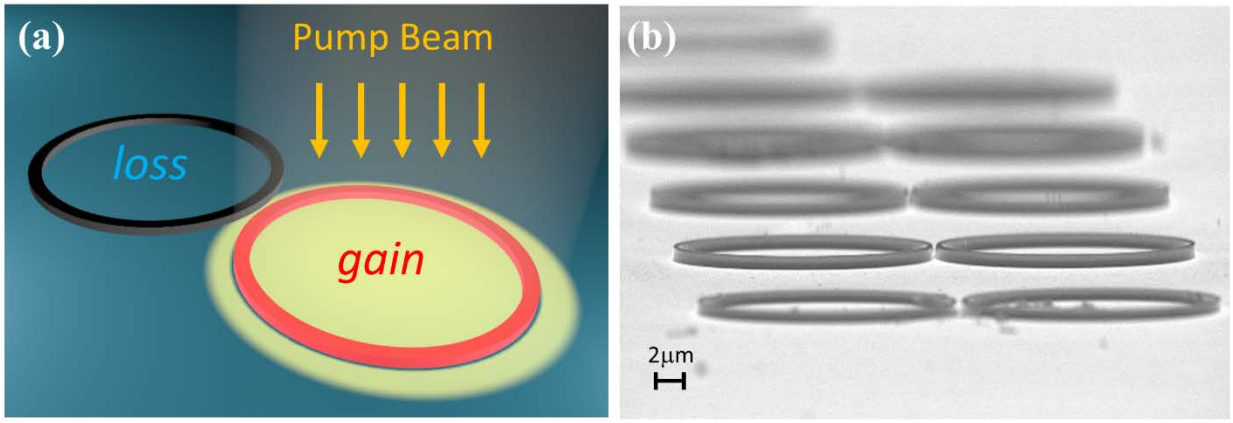

Figure 10. (a) Schematic of a PT symmetric microring laser. The pump beam is selectively withheld from one of the rings using a knife edge (b) Scanning electron microscope image of a typical set of microring resonator pairs with different separations at an intermediate fabrication step.

Figure 11 illustrates the trajectories of the eigenfrequencies associated with the aforementioned coupled micro-cavity system in the complex domain, as they transition through an exceptional point. In this example, we start with an equally pumped coupled micro-ring arrangement entailing two modes separated by $2\kappa_n$ along the real frequency axis. As one gradually reduces the gain in one of the resonators and replaces it with loss, while the other ring is kept fixed at the initial gain level, the splitting of the resonant frequencies in the real domain monotonically decreases. At the same time, the imaginary components of the eigenfrequencies are reduced due to the lower available net gain. Nevertheless, the imaginary parts of both eigenfrequencies remain equal, indicating that the supermodes are evenly distributed between the two rings. This trend continues until the system reaches the exceptional point. At this juncture, the eigenfrequencies become fully identical in both their real and imaginary parts. Beyond this point and as the gain in the second ring is further reduced, the resonant frequency of the two modes become degenerate, while the imaginary

parts bifurcate. These changes reflect the fact that in the broken-symmetry regime one of the supermodes primarily resides in the gain region (therefore experiencing more amplification), while the other one mainly occupies the lossy ring (hence attenuates).

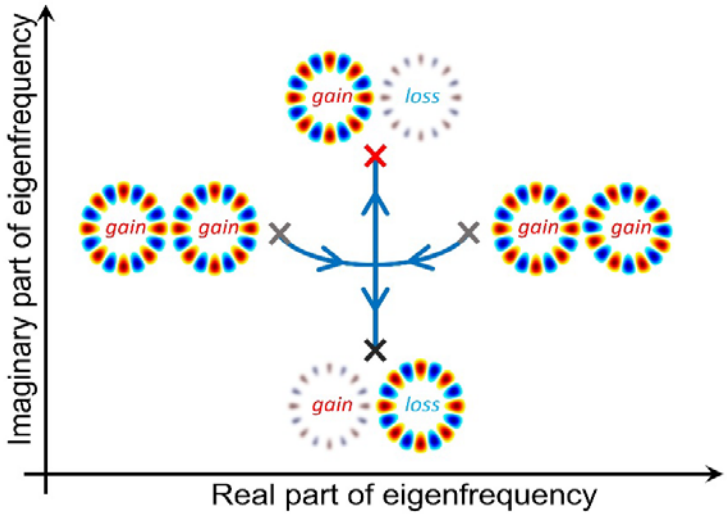

Figure 11. Evolution of eigenfrequencies as the gain in one of the double active cavities is being gradually replaced with loss. Below the exceptional point, the eigenfrequencies split along the real axis, while keeping the same imaginary components. Above the exceptional point, the real parts of the eigenvalues merge while the imaginary parts bifurcate. At the exceptional point, the eigenfrequencies become completely identical in the complex domain.

In order to experimentally study the response of a non-Hermitian coupled system around an exceptional point, a number of microring pairs are nano-fabricated. The microrings are comprised of six InGaAsP quantum wells, so that one can achieve different amounts of gain and loss in each cavity by selectively supplying an appropriate optical pump intensity to the quantum wells. The rings in these experiments have an outer radius of 10 μm, a width of 500 nm, and a height of 210 nm. The emissions from these structures were

visually and spectrally characterized by imaging the surface of the rings onto a CCD camera and by sending their radiation to a spectrometer, respectively. To realize the PT-symmetric arrangement, a knife-edge is utilized to selectively withhold the pump illumination from one of the rings. A detailed description of the fabrication process and measurement setup is provided in chapter 9.

We study the effect of applying a non-uniform pump distribution to observe the transition of the system in the parameter space. For our subsequent experiments, we choose rings with a separation of 150 nm which leads to the coupling strength of $\sim 7 \times 10^{11}\ s^{-1}$. First, an evenly distributed pump is illuminating both cavities (Fig.12 (a)). Gradually loss is introduced to one of the rings by partially blocking the pump with a knife edge. Figures 12 (a-d) show the corresponding evolution of the output spectra. The associated intensity profiles of the rings are also depicted in the insets of Figs. 12 (a-d). As the loss is increased, the two resonant peaks associated with the two supermodes move towards each other, while their respective intensities gradually decrease due to a reduced overall gain. A drastic change, however, happens when the system passes the exceptional point (Fig. 12(d)). At this point, the two supermodes become spectrally degenerate and only the broken-symmetry mode with the higher Q-factor experiences sufficient amplification to lase. There are two unique characteristics that distinguish this system: i) the PT-broken mode occurs at the center of the two resonant peaks of the evenly pumped system, ii) the PT-mode primarily resides in the pumped cavity (Fig. 12(d) inset). As a result, it is expected that the efficiency of such mode in the PT configuration not to be compromised by the presence of the lossy cavity as long as it operates in the broken symmetry regime. In the next chapter, we show

how this abrupt breaking of PT-symmetry in double microring systems can be fruitfully utilized to enforce single mode lasing with considerably enhanced mode discrimination in microring arrangements.

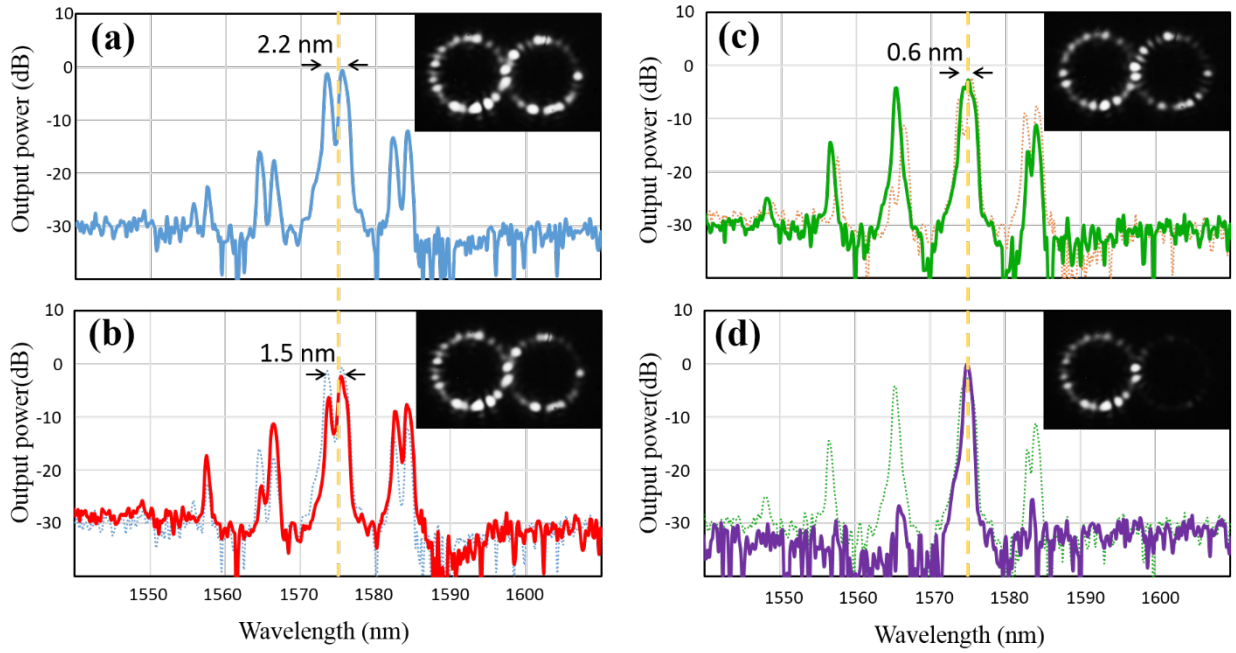

Figure 12. Evolution of the emission spectra of a double ring structure as a knife-edge gradually covers the right ring, thus introducing loss. The insets show the intensity profile in the two rings collected from the scattered emission. The resolution of the spectrometer is set at 0.4 nm. High-resolution linewidth measurements (see the appendix) show that the linewidth in (d) is ~10 GHz.

4.2. Lasing threshold

In this section, the lasing threshold condition for a PT-symmetric microring arrangement is derived. For this analysis, we use temporal coupled mode equations that describe the time evolution of the modal fields for the m^{th} longitudinal mode in the active cavity (E_{1m}) and in the lossy resonator (E_{2m}):

$$\begin{cases} \frac{dE_{1m}}{dt} = -\gamma E_{1m} + \frac{\sigma(p-1)}{1+\varepsilon|E_{1m}|^2} E_{1m} + i\kappa E_{2m} \\ \frac{dE_{2m}}{dt} = -\gamma E_{2m} - \frac{\sigma}{1+\varepsilon|E_{2m}|^2} E_{2m} + i\kappa E_{1m} \end{cases} \quad (4.3)$$

Here, κ denotes a temporal coupling coefficient between these two cavities, and it is related to the spatial coupling θ described above through $\kappa = \theta v_g/(2\pi R)$, where v_g is the group velocity, and R is the radius of the ring resonator. The linear loss γ (scattering, radiation losses, out-coupling, *etc.*) is taken to be the same in both resonators and it relates to quality factor Q via $\gamma = c/(\lambda_0 Q)$. In these equations $\sigma(p-1)$ and σ respectively represent the small signal gain (for $p > 1$) due to the pumping parameter p of the quantum wells and absorption loss in the absence of pumping, where $\sigma = \Gamma v_g A N_0$, with A being the gain constant, N_0 the transparency carrier population density, and Γ the confinement factor. Moreover, $p = \tau_e R_p/N_0$ is the pump parameter, where the carrier generation rate is given by $R_p = \eta I/(\hbar\omega p d)$ and I, η, d represent the pump intensity, external quantum efficiency, and the height of the multiple quantum wells in each micro-ring, respectively. In addition,τ_e is the carrier lifetime and $\hbar\omega_p$ is the energy of a pump photon. The parameter ε is inversely proportional to the saturation intensity $\varepsilon = nc\tau_e\epsilon_0 A\Gamma/(2\hbar\omega)$, where n is the refractive index of the structure [76].

To find the lasing threshold, the above equations are first linearized (small field amplitudes). Then, by adopting the parameters $G_m = \sigma(p-1)$ and $(a_m, b_m) = \sqrt{\varepsilon}\,(E_{1m}, E_{2m})$, we arrive at:

$$\begin{cases} \frac{da_m}{dt} = -\gamma a_m + G_m a_m + i\kappa b_m \\ \frac{db_m}{dt} = -\gamma b_m - \sigma b_m + i\kappa a_m \end{cases} \quad (4.4)$$

In the linearized region, the eigenvalues of this system, ζ, can be obtained through $(a_m, b_m) = (a_{0m}, b_{0m})exp(-i\zeta t)$, where a_{0m} and b_{0m} are in general complex constants. Hereby, two regimes can be identified, depending on the value of $(G_m + \sigma)$. In the first case, where $(Gm + \sigma) < 2\kappa$, the modal solutions of Eq. (4.4) are associated with the symmetry-preserved case and are given by,

$$\begin{pmatrix} a_m \\ b_m \end{pmatrix} = \begin{pmatrix} 1 \\ \pm e^{\pm i\delta} \end{pmatrix} e^{\left(\frac{G_m - \sigma}{2} - \gamma\right)t} e^{\pm i(\kappa \cos(\delta))t} \quad (4.5)$$

where $\sin(\delta) = (G_m + \sigma)/2\kappa$. If on the other hand, $(G_m + \sigma) > 2\kappa$, the solutions are,

$$\begin{pmatrix} a_m \\ b_m \end{pmatrix} = \begin{pmatrix} 1 \\ ie^{\pm\delta} \end{pmatrix} e^{\left(\frac{G_m - \sigma}{2} - \gamma\right)t} e^{\mp\kappa(\sinh(\delta))t} \quad (4.6)$$

where $cosh(\delta) = (G_m + \sigma)/2\kappa$. These latter solutions are characteristics of a broken PT-symmetry phase, since the fields in the two cavities are now unequal. If the system operates in the unbroken PT-symmetry regime, given by Eq. (4.5), then, according to the exponential term, linear amplification takes place if the gain is above the total loss in the system, *i.e.* $G_m > (2\gamma + \sigma)$. However, in the broken PT-symmetric phase, Eq. (4.6), growth occurs if $G_m > \kappa 2(\gamma + \sigma)^{-1} + \gamma$. To derive this latter condition, one has to consider the $\kappa(sinh(\delta))$ term in the exponent. From these two threshold conditions, it can be directly inferred that if $(\gamma + \sigma) > \kappa$, then the PT-broken phase has a lower threshold and hence is the one to lase. Conversely, if $(\gamma + \sigma) < \kappa$, the situation is reversed and the unbroken PT eigenstate will be the one to experience amplification. These two lasing thresholds can be summarized by the following relationship

$$G_{th} = \min\left[\frac{\kappa^2}{\gamma + \sigma} + \gamma, 2\gamma + \sigma\right] \quad (4.7)$$

To contrast these results to the lasing threshold of a single ring, one should consider the field dynamics described by Eq. (4.4) in the absence of coupling ($\kappa = 0$). In this case, the lasing threshold is simply given by $G_m^{th} = \gamma$. A typical set of parameter values in such semiconductor quantum well structures can provide a good comparison between a single ring and a PT-symmetric laser arrangement. Assuming $Q = 120{,}000$, hence the photon decay rate at $\lambda = 1.55\ \mu m$ is $\gamma = 1.5 \times 10^9\ s^{-1}$. The unsaturated absorption loss σ for $\Gamma = 0.5$, $v_g = c/3.8$, $A = 2 \times 10^{-20}\ m^2$ and $N_0 = 10^{24}\ m^{-3}$, is estimated to be $\sigma = 8 \times 10^{11}\ s^{-1}$. The coupling κ can be determined from the splitting of the longitudinal modes i.e. $\Delta\omega = 2\kappa$. From our experiments, we find that κ is in the order of $5 \times 10^{11}\ s^{-1}$. These values clearly indicate that $(\gamma + \sigma) > \kappa$ and therefore lasing in our structure is initiated in the broken symmetry mode, which is a necessary condition in our PT-symmetric mode management scheme. In this case, the threshold pump parameter for the PT-symmetric case is given by:

$$p^{PT} = 1 + \frac{\gamma}{\sigma} + \frac{\kappa^2}{\sigma(\gamma+\sigma)} \qquad (4.8)$$

In comparison, the lasing threshold for a single ring is $p^{single} = 1 + (\gamma/\sigma)$. Given that for the aforementioned values, $\gamma \ll \kappa < \sigma$, one can arrive at the interesting conclusion that these two thresholds are fairly close to each other. Figure 13 illustrates the ratio p^{PT}/p^{single} as function of the coupling strength when unsaturated absorption in the quantum well cavities is varying from 50 to 200 cm^{-1}.

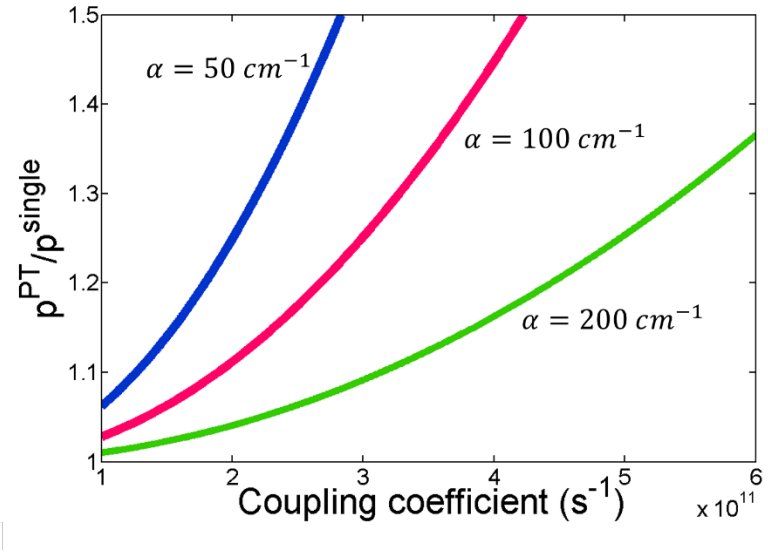

Figure 13. Ratio of lasing thresholds for PT-symmetric arrangement to single microring, at different coupling coefficients and for various absorptions in the quantum wells

4.3. Gain clamping and saturation

The linear analysis in section 4.1 can provide insights and predict the behavior of a PT-symmetric coupled cavity laser. However, every laser is an inherently nonlinear device due to the gain clamping and saturation. Therefore, to fully understand the dynamics of operation in a PT-symmetric laser, these nonlinear aspects should be taken into account. In this section, we qualitatively explain their nonlinear behavior. A detailed analysis including these nonlinearities has been performed in our group, the results of which is publish in [77].

In many amplifier settings, increasing the pump power leads to an increase in the resulting optical gain. However, during lasing action, the gain is firmly clamped to a precise value (total optical losses in the structure), which cannot be surpassed even with very high pump powers. Therefore, the extra pump energy results in boosting of the field amplitude

within the cavity and subsequently higher output intensity. This is also the case in a PT-symmetric coupled cavity laser. When both rings are pumped, the total gain in both resonator is equal to the total scattering and radiation losses (i.e. linear loss) in the structure,

$$\sigma_1 + \sigma_2 = 2\gamma, \qquad (4.9)$$

here, σ_1 and σ_2 represent the material gain/loss in the resonators and γ is the linear loss of each cavity which is related to the quality factor as indicated in the previous section. Now, if material loss gradually replaces the gain in one of cavities (selectively reducing the pump power), the gain in the active ring should compensate for this new source of loss in order to preserve lasing as well as PT-symmetry in the structure. Hence,

$$\sigma_1 = \sigma_2 + 2\gamma. \qquad (4.10)$$

In this case the gain-loss contrast in the structure is given by,

$$\Delta g = (\sigma_1 - \gamma) - (\sigma_2 + \gamma) = 2\sigma_2. \qquad (4.11)$$

Equation (4.11) indictaes that the gain-loss contast in a PT-laser is related to the material or nonlinear loss in the dark cavity. In this regard, if $\sigma_2 < \kappa$, the system continoues lasing in an un-broken PT-symmetric fashion. On the other hand, once this loss exceed the coupling strength ($\sigma_2 > \kappa$), the energy transfer between the two resonators can no longer supply the required light to maintain the lasing in the lossy resonator, and therefore, the PT-symmetry will break. Since κ is a fixed value defined by the geometry of the structure, in a PT-symmetric laser the regime of operation is dictated by the material loss in the lossy resonator, which can easily be controlled by changin the supplied pump power to this cavity. On the other hand, the gain's role is only to ensure the occurance of the lasing action in structure. Therefore, the amount of gain, in any regime of operation, should be higher than

the lasing threshold. This threshold is given in Eq. (4.7) for both un-broken and broken PT-symmery regims.

In order to observe the PT-symmetry breaking phase transition at relatively low pump powers, it is necessary to start with double pumped ring and then gradually replace the gain in one of the resonators with loss. Because, when one cavity is subject to amplification in an initially un-pumped arrangement, the system will start lasing whether in broken or un-broken PT-regime, depending on the loss and coupling values. In this case, the configuration remains in the same state of operation throughout a vast range of pump powers. Although the broken PT-symmetry can change to un-broken at very high power levels due to loss saturation in the dark cavity [77], the high amount of pumping makes this reverse transition very hard to reach and challenging to use.

CHAPTER 5:
MODE MANAGEMENT IN PT-SYMMETRIC MICRORING LASERS

In this section, we show that PT-symmetry breaking can be effectively exploited to enforce single longitudinal mode operation in inherently multi-moded micro-ring lasers. This is accomplished in a coupled arrangement of two structurally identical ring resonators, where one experiences gain, and the other one is subjected to an appropriate amount of loss. The key idea behind this mechanism is the fact that the threshold of symmetry breaking depends solely on the relation between gain/loss and coupling. Whereas any active resonator is in principle capable of displaying single-wavelength operation, selective breaking of PT-symmetry can be utilized to systematically enhance the maximum achievable gain of this mode, even in presence of a large number of longitudinal or transverse modes with similar quality factor. The differential amplification of the modes due to the gain bandwidth is used for longitudinal mode selection, while single transverse mode operation is enforced via the difference in the coupling factors. Finally, we investigate the system's stability and its robustness to perturbations. The results in this chapter have been published in [78] and [79].

5.1. Longitudinal mode management

Following the same discussion as in section 4.1, we consider two coupled microrings. The small structure size associated with such devices necessitates a high refractive index contrast. The interaction between two adjacent rings is mediated by the mutual overlap of their fields in the narrow region of greatest proximity, and the coupling coefficient κ determines the frequency splitting $\delta\omega$ between mode pairs. As shown in chapter 3, the free

spectral range, or mode spacing, of a ring with radius R and effective group index n_g is given by $\Delta\omega = c/Rn_g$. Assuming an active medium with an inhomogeneously broadened amplification profile $g(\omega)$, each and every mode whose gain exceeds the resonator losses can lase (see schematic in Fig.14 (a)).

In this coupled arrangement, PT-symmetry is established when the gain experienced in one ring is balanced by the loss in the other. If PT-symmetry is unbroken, the modes neither decay nor grow, but rather remain neutral. By contrast, once the gain-loss contrast is increased beyond the coupling constant, this symmetry is broken and the respective modes experience gain or loss in conjugate pairs [64]. This phase transition lies at the heart of our approach.

When two identical resonators are placed next to one another, the degeneracy between their respective modes is broken (see Fig. 14 (b)). The frequency splitting $\delta\omega$ of the resulting supermode doublets $\omega_n^{(1,2)}$ is directly proportional to the coupling coefficient, i.e., $\delta\omega = 2\kappa$. The resulting eigenfrequencies of such an active system can in general be complex, and their imaginary part describes amplification or attenuation. Meanwhile, in PT-symmetric arrangements, the relationship between eigenfrequencies and coupling is by nature different as described in Eq. (4.2). If the amount of gain and loss in the rings are considered to be equal ($\gamma_{a_n} = -\gamma_{a_n} = \gamma_n$), Eq. (4.2) simplifies to

$$\omega_n^{(1,2)} = \omega_n \pm \sqrt{\kappa_n^2 - \gamma_n^2}. \qquad (5.1)$$

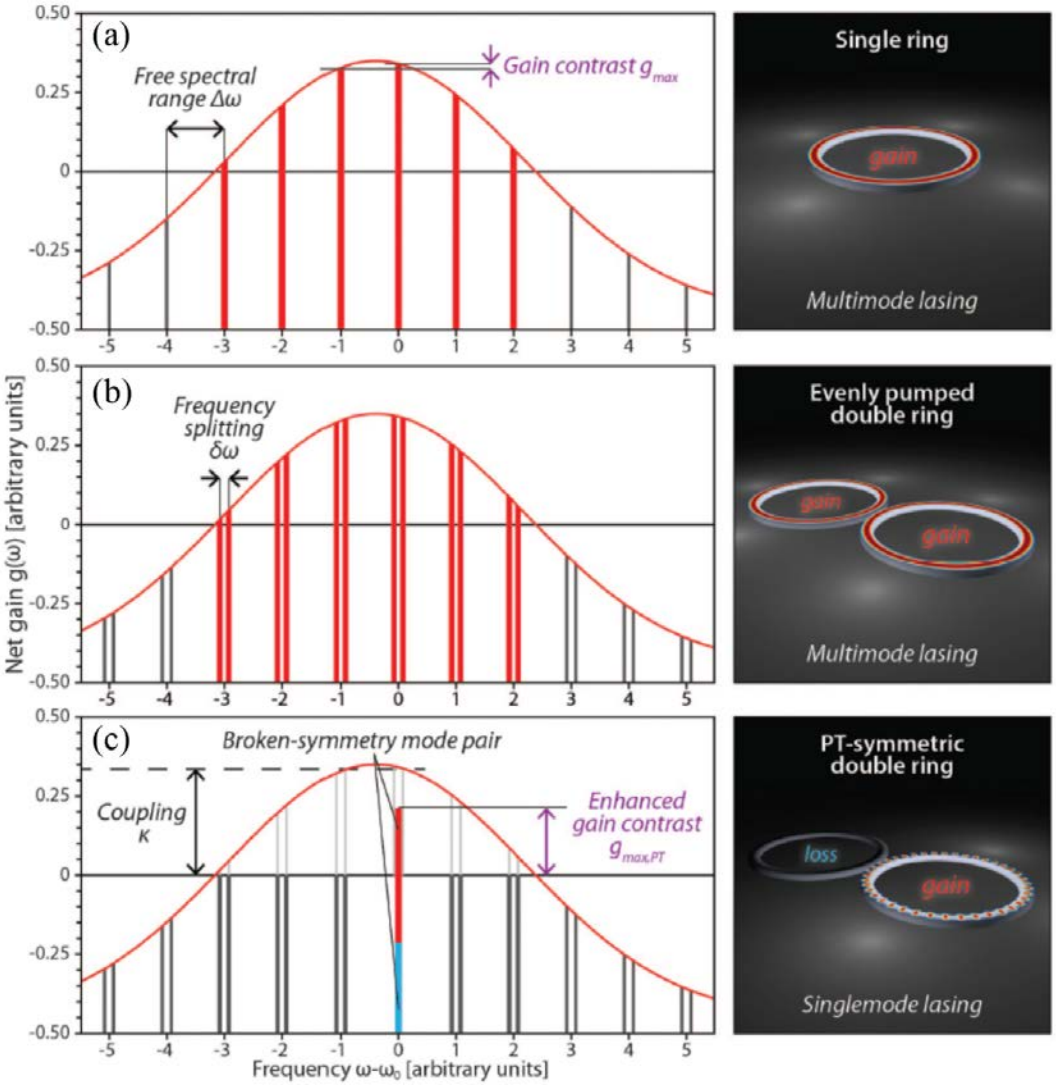

Figure 14. Schematic principle of mode suppression in PT-symmetric microring lasers. (a) An isolated ring resonator allows lasing of all longitudinal modes with positive net gain. To achieve single-mode operation, maximum permissible gain is limited by the gain contrast between the resonances. (b) In a coupled arrangement of two identical and evenly pumped rings, the degeneracy of resonator modes is broken and mode pairs emerge; their frequency splitting is a measure for the coupling strength. (c) PT-symmetric arrangement: As long as the coupling exceeds the amplification, loss and gain in the two respective rings balance each other, whereas above this threshold, PT symmetry breaking occurs. This mechanism can be exploited to enforce stable single-mode operation in otherwise highly multi-moded resonators. Note that the gain contrast is systematically enhanced with respect to the single-resonator scenario.

When Any pair of modes, whose gain-loss contrast γ_n remains below the coupling coefficient κ_n, undergoes bounded neutral oscillations. The absence of any overall gain or loss is easily understood considering that the modes reside equally in the amplifying and lossy regions, as shown in Fig.15. However, as soon as γ_n exceeds κ_n, a conjugate pair of amplifying and decaying modes emerges. Clearly, a judicious placement of this PT threshold will allow a complete suppression of all non-broken mode pairs in favor of a single amplified mode associated with the aforementioned conjugate pair (see Fig.14 (c)). As the imaginary parts of the eigenvalues diverge, degeneracy between their real parts is restored. We emphasize that even in the absence of a lossy counterpart (PT-symmetry), any laser cavity with a spectrally non-uniform gain distribution $g(\omega)$ can in principle exhibit single-mode operation, provided that the losses overcompensate the gain for all but one resonance. However, in this regime, the amplification cannot exceed the gain contrast $g_{max} = g_0 - g_1$ (see Fig.14 (a)). Here, g_0 refers to the gain of the principal mode, whereas g_1, to that of the next-strongest competing resonance. Obviously, this approach will impose severe constraints on the operating parameters— especially in the case of broad gain windows and/or closely spaced resonator modes, where g_{max} is very small. By contrast, in a PT-symmetric setting, the coupling κ now plays the role of a virtual loss, and all undesirable modes must fall below its corresponding threshold. According to Eq. (5.1), we find that in this case, the maximum achievable gain differential is given by

$$g_{max,PT} = \sqrt{g_0^2 - g_1^2} = g_{max} \times \sqrt{\frac{g_0 \backslash g_1 + 1}{g_0 \backslash g_1 - 1}} \qquad (5.2)$$

Given that $g_0 \geq g_1$, a selective breaking of PT-symmetry can therefore systematically increase the available amplification for single-mode operation. The square root behavior of this enhancement (a direct outcome of the PT symmetry breaking and the associated exceptional point), as characterized by the factor $G = g_{max,PT}/g_{max}$, can provide substantially higher selectivity, especially when the initial contrast between adjacent modes is small ($g_1 \rightarrow g_0$, see Fig.14 (c)). This type of mode discrimination is resilient and remains valid even when PT-symmetry does not exactly hold for all modes involved. On a fundamental level, the mechanism is related to the presence of an exceptional point in the system which is discussed and experimentally investigated in chapter 4. The influence of deviations from ideal PT-symmetry conditions is investigated in Section 5.3. It can be shown that the strong coupling between rings, makes this arrangement relatively immune to local perturbations introduced by fabrication errors, nonlinearities, and/or temperature gradients.

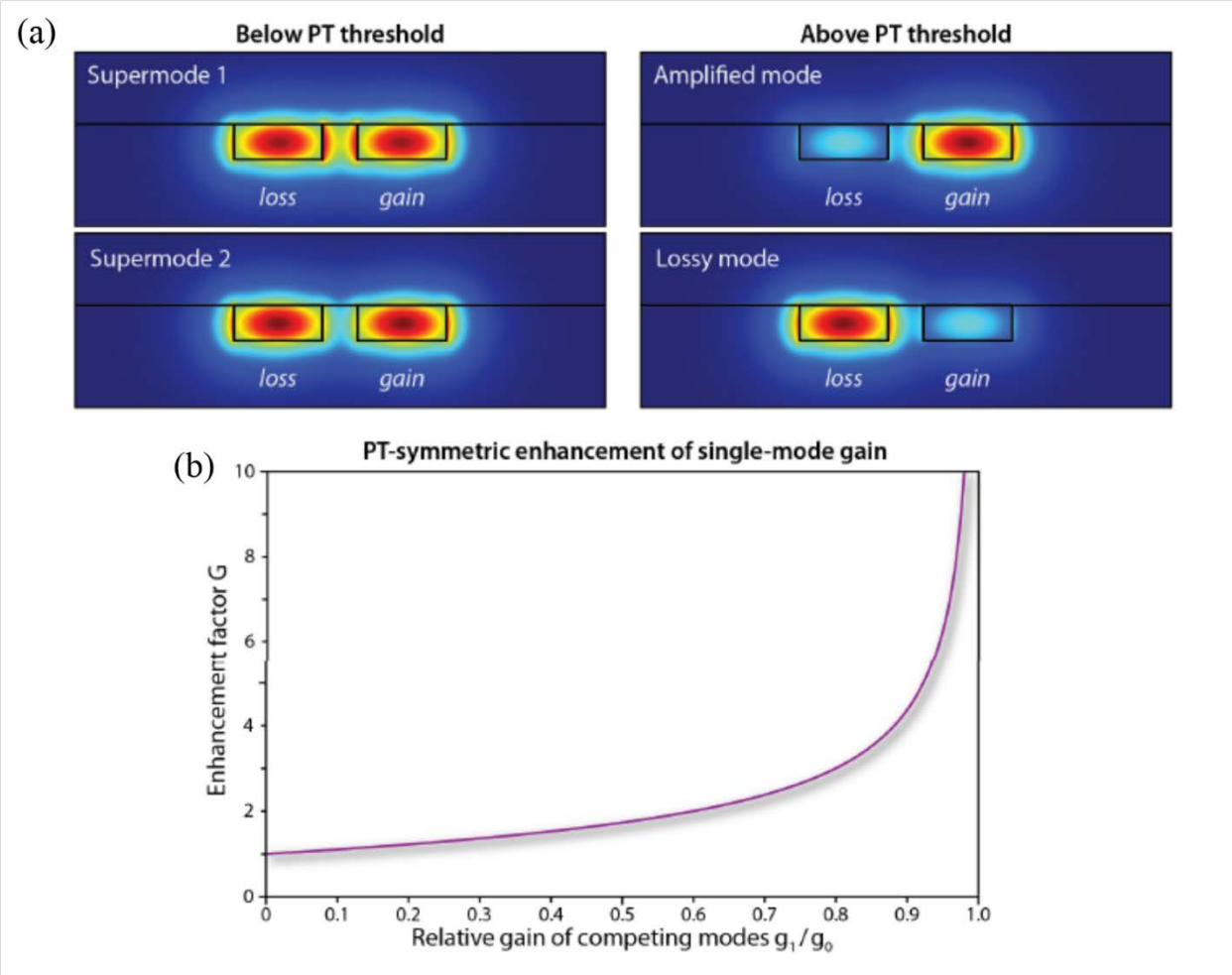

Figure 15. Transverse intensity distributions at the point of closest proximity between the rings. Below the threshold of PT symmetry breaking (left), the supermodes are evenly distributed between the gain and loss regions, respectively. In contrast, above the threshold (right), the modes predominantly reside in one of the rings, and consequently experience a net loss/gain. (b) Enhancement G of the maximum achievable differential gain for single-mode operation in a PT-symmetric setting compared to a single active resonator.

To experimentally verify this approach, three possible configurations (single ring, evenly pumped double ring and PT-symmetric ring arrangement) are realized and the mode selectivity in a PT symmetric scenario is demonstrated. Accordingly, the effective pump

powers are calculated from the geometric overlap between the active medium and the pump profile. Figures 16(a,b) illustrate the behavior of a single ring (radius 10 μm, ring width 500 nm, height 210 nm) when exposed to an effective peak pump power of 4.9 mW (15 ns pulses with a repetition rate of 290 kHz). Under these conditions, at least four modes contribute significantly to lasing in the isolated ring. When two such rings are placed at a distance of 200 nm from one another, and both exposed to the same pump power, one can clearly see the coupling-induced mode splitting (Figs. 16 (c,d)), which occurs symmetrically around the resonance wavelengths of each ring in isolation. In this coupled regime, both structures are contributing equally. Once PT-symmetry is established by withholding the pump from one of the resonators (Figs. 16(e,f)), lasing occurs exclusively in the active ring, where single-mode operation is now achieved. The presence of the lossy ring only serves to suppress the unwanted longitudinal modes with a contrast exceeding 20 dB.

Figure 17(a) shows the characteristic light-light curves for all three arrangements involving the 10 μm rings. In all cases the transition to the lasing regime, defined by the sudden onset of emission, is clearly visible. The PT-symmetric arrangement appears almost indistinguishable from the single ring, indicating that the presence of the lossy element does not decrease the overall slope efficiency. Of course, a spectrally resolved comparison of these two scenarios (Fig. 17(b)) reveals that the PT system actually offers superior performance, since the emission from the single ring includes contributions from several modes. The collected data represents the scattering off the ring resonators.

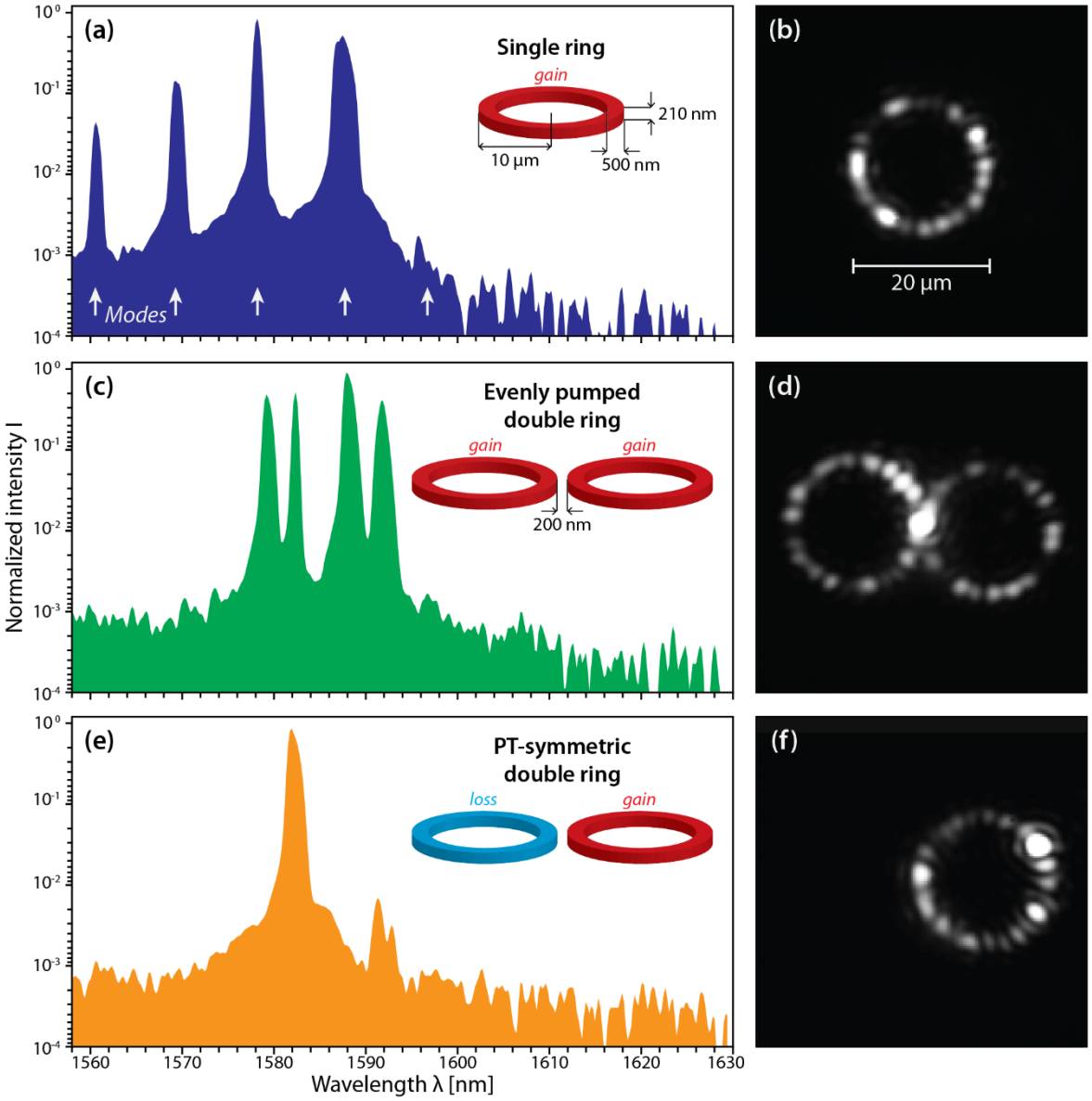

Figure 16. Experimental observation of mode suppression by PT-symmetry breaking. (a) Emission spectrum of a single resonator (radius 10µm, ring width 500 nm, height 210 nm) when exposed to a peak pump power of 4.9 mW. (b) Corresponding intensity pattern within the ring as observed from scattered light. (c) Spectrum obtained from an evenly pumped pair of such rings (4.9 mW + 4.9 mW). (d) The intensity pattern shows that both resonators equally contribute. (e) Single-moded spectrum under PT-symmetric conditions (0 mW + 4.9 mW pump). The mode suppression ratio exceeds 20dB. (f) Lasing exclusively occurs in the active resonator.

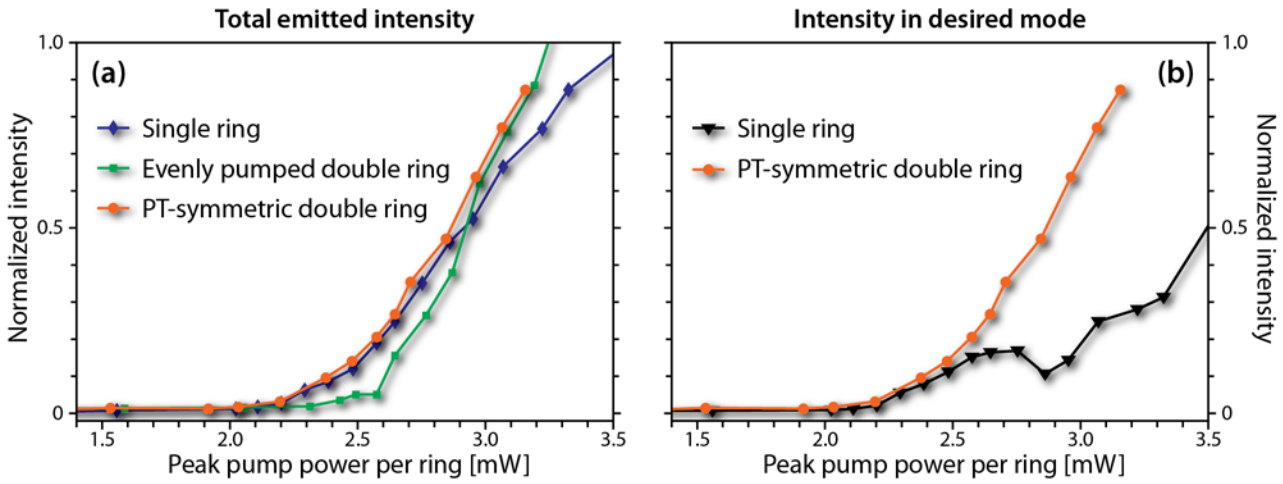

Figure 17. (a) Characteristic light-light graphs of the single, double, and PT-symmetric microring resonator arrangements. (b) Spectrally resolved plots comparing the intensity emitted in the desired mode. The PT-symmetric configuration clearly offers superior performance. The onset of parasitic modes is indicated by the kinks in the single-ring graph.

5.2. Transverse mode management

Integrated photonic laser systems with larger cross sections are desirable for many applications since they allow for higher energies within the cavities while managing the thermal load and keeping the impact of optical nonlinearities under control. Unfortunately, however, merely enlarging the transverse dimensions of the waveguides inevitably gives rise to competing higher-order spatial modes. This, in turn, compromises the spectral and spatial fidelity of the laser and limits the power allocated within a specific mode [19]. These limitations exist on all scales, and may even be exacerbated in chip-scale semiconductor lasers, where the large gain bandwidths of the active media already pose a challenge in promoting single-mode operation [20].

So far, tapering along the direction of propagation, engineering the refractive index in the cross section, as well as evanescent filtering are some of the extensively explored techniques to enforce single spatial mode operation in such arrangements [80]–[83]. Yet, in spite of their success, they are not always compatible with on-chip microcavity structures and in most cases are quite sensitive to small fabrication tolerances. In this respect, it would be desirable to explore alternative avenues to address these issues.

In this section, we show that selective breaking of parity-time (PT) symmetry can also be utilized in promoting the fundamental transverse mode in spatially multi-moded micro-ring lasers. In fact, as shown in [64], the virtual threshold at the exceptional point $g/\kappa = 1$ introduces an additional degree of freedom, e.g., the coupling constant κ between the active and the lossy cavity, mediated by the evanescent overlap of their respective modes. As it is well-known, higher order spatial modes systematically exhibit stronger coupling coefficients due to their lower degree of confinement. Consequently, in a PT symmetric arrangement, the fundamental mode is the first in line to break its symmetry as the gain increases (when $g > \kappa$), thus experiencing a net amplification. On the other hand, for this same gain level, the rest of the modes retain an unbroken symmetry and therefore remain entirely neutral. The coupled mode analysis describing the behavior of transversely multi-mode coupled resonators are the same as in sections 4.1, except for coupling coefficient which is different for various transverse modes.

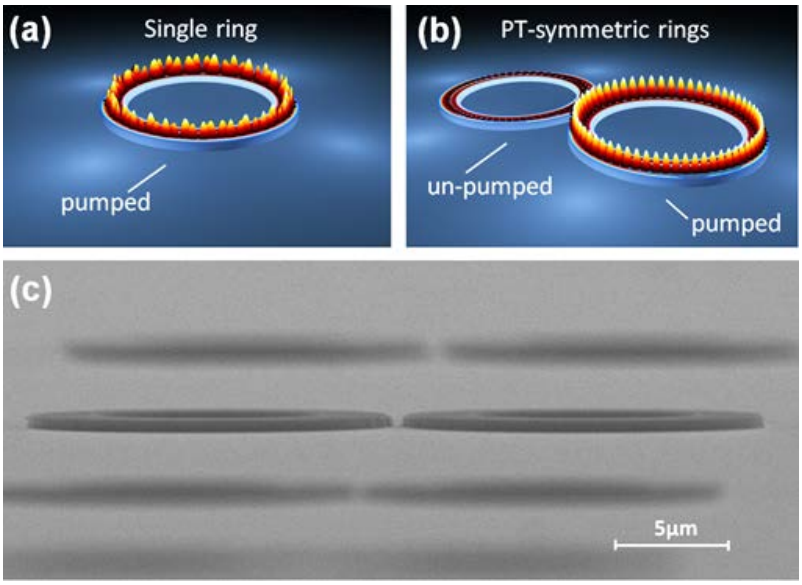

Figure 18. Schematic representation of a multimode isolated ring versus Single mode PT symmetric arrangement. (a) In a single microring resonator, multiple transverse and longitudinal modes can lase simultaneously (b) on the other hand, in a PT-symmetric arrangement, only one longitudinal mode with the lowest order transverse profile can lase, and (c) an SEM image of a PT-symmetric double ring structure.

Figures 18 (a) and (b) schematically illustrate the transition from multimode behavior in a microring laser to single mode operation in a twin-ring configuration as enabled by preferential PT symmetry breaking. Our experiments were conducted in high-contrast active ring resonators based on quaternary InGaAsP (Indium-Gallium-Arsenide-Phosphide) multiple quantum wells embedded in SiO2 (silicon dioxide) and air as shown in Fig.18 (c). Based on our measurements, we estimate the quality factor of the fabricated microrings to be on the order of 120,000. The gain bandwidth of the active medium spans the spectral region between 1290 and 1600 nm [34]. In our proof-of-principle design, a ring of an outer radius of $6\,\mu m$ and waveguide dimensions of $0.21\,\mu m \times 1.5\,\mu m$ are chosen to realize

comparably large free spectral range ($\Delta\lambda_{FSR}\sim 16\,nm$) and readily discernible three sets of transverse modes.

Figures 19 (a-c) depict the transverse intensity profiles of different spatial modes supported by such a single microring resonator. The curvature of the ring imposes a radial potential gradient, which deforms the mode fields into whispering-gallery-like distributions. Whereas the peak of all modes shifts towards the ring center, the exponential decay outside the ring still grows strongly with the mode order. As shown in Fig.19 (d-f), for a certain coupling coefficient, set by the distance between the two rings, the transverse TE_0 field is the only mode to break its PT symmetry while all the higher order modes (TE_1, TE_2) are still in the unbroken PT phase and hence occupy both rings equally. This behavior is also evident in Fig.19 (g) where the coupling strength between different transverse modes is depicted as a function of the separation between the two rings. For a fixed distance, the coupling coefficient increases with the order of the transverse mode since the effective indices of higher order modes lie closer to that of the surrounding medium, allowing for stronger evanescent interactions across the cladding region. This trend persists for all wavelengths, and in conjunction with the difference in confinement enables PT symmetry breaking to be employed as a mode-selective virtual loss. It should be noted however that coupling coefficient also a function of wavelength. As a result, different longitudinal modes experience slightly different coupling coefficients (see Fig. 20(a)). In addition, the confinement factor (related to the overlap of the field with active regions) also plays a role in determining the modal gain, and it is described by

$$\Gamma = \frac{\int_{V_a} dr|<S(r)>|^2}{\int_{-\infty}^{+\infty} dr|<S(r)>|^2}, \qquad (5.3)$$

where $|< S(r) >|$ is the time averaged Poynting vector and the integration in the nominator is taken over the cross section of the microring resonator. The coupling strength and confinement factor is shown in Fig.20 (b) with respect to the wavelength. Clearly, higher order transverse modes exhibit lower confinement and therefore experience less modal gain. This behavior is again in favor of selective PT symmetry breaking for the fundamental transverse mode.

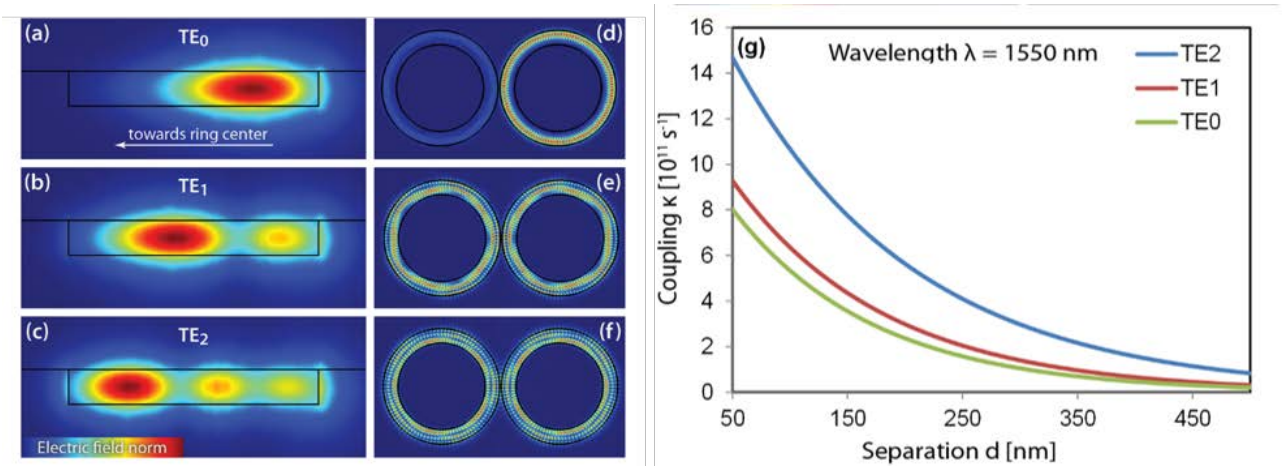

Figure 19. Spatial mode profiles and coupling strengths for different transverse modes in the structure (a-c) Intensity distributions in a microring resonator with a cross section 0.21 μm × 1.5 μm and a radius of $R = 6\ \mu m$ as obtained by finite element simulations for the first three transverse modes, (d-f) intensity distribution of these same modes within the PT-symmetric ring resonators. While the TE_0 mode operates in the broken PT symmetry regime and lases, all other modes remain in their exact PT phase and therefore they stay neutral (below lasing threshold), and (g) Exponential decay of the temporal coupling coefficients κ with cavity separation d. Higher order modes exhibit larger coupling coefficients than their lower-order counterparts.

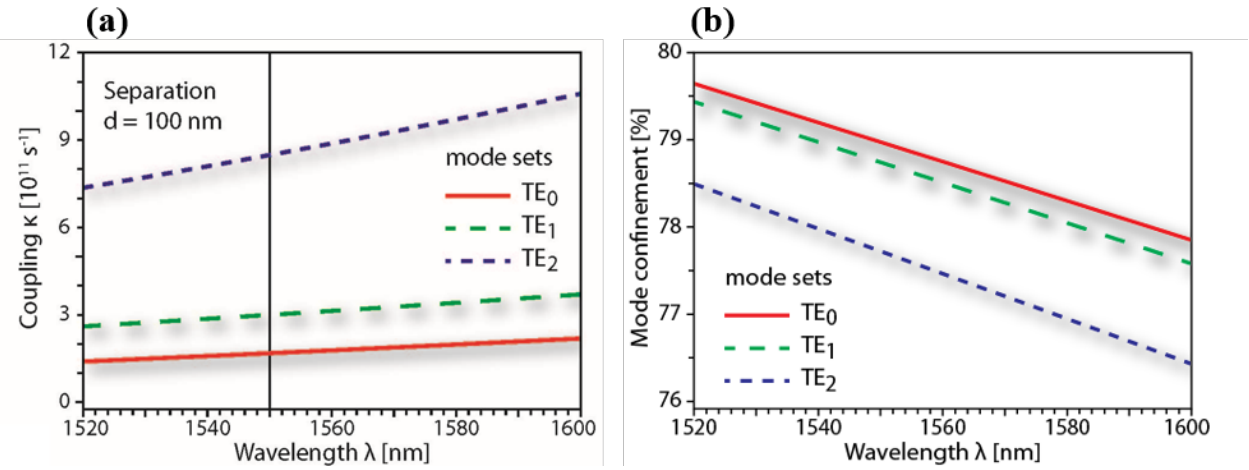

Figure 20. (a) The coupling coefficient and (b) the confinement factor corresponding to different transverse modes of a microring resonator with respect to wavelength when the separation between the rings is 100 nm.

In order to experimentally illustrate the selective breaking of PT symmetry, we consider a scenario where a coupled arrangement of identical microring resonators is evenly illuminated by the pump beam. In this case, as shown in Figure 21(a), every resonance in each ring splits into a doublet. In our system, the modes can be distinguished both theoretically and experimentally by considering their wavelength splitting (coupling strength) as well as their corresponding free spectral ranges. For example, the TE_1 supermodes exhibit greater frequency splitting compared to the TE_0 ones due to their higher coupling coefficient. In the PT-symmetric system where only one of the two rings is pumped, the TE_0 modes preferentially undergo PT-symmetry breaking due to their higher modal confinement and fuse into a singlet. In addition, given that different longitudinal modes experience different amounts of gain, one can restore the PT-symmetry of one of the TE_0 modes by adjusting the pump level. As a result, global single mode operation (spectrally and

spatially) can be achieved in this twin-microring system, as only one single longitudinal resonance of the fundamental TE_0 mode experiences sufficient gain to induce PT-symmetry breaking. Figure 21(b) shows the fusion of a doublet in the frequency domain and the formation of a single lasing mode.

Figure 22 compares the modal behavior of a single ring and a PT-symmetric double ring system. Figure 22(a) shows the spectrum obtained from a single microring resonator supporting up to three transverse modes. Due to their relatively close lasing thresholds, TE_0, TE_1 and TE_2 simultaneously lase. Note that, in an isolated ring, a decrease of the overall pump power does in practice yield very small selectivity between these modes. On the other hand, when the active ring of the PT-symmetric double-ring arrangement is supplied with the same pump power as in Fig. 22(a), the higher order modes are readily suppressed with a fidelity of over 25 dB (Fig. 22(b)).

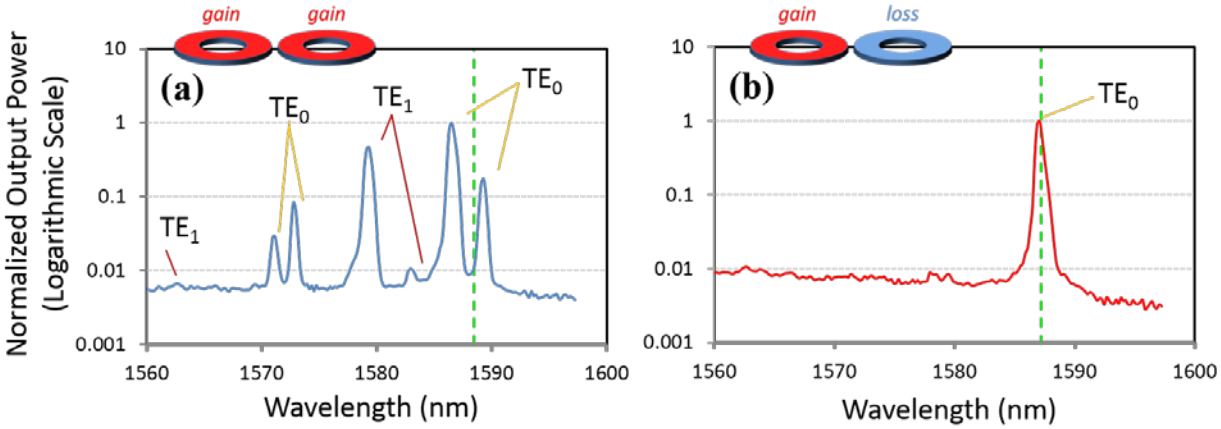

Figure 21. PT-enforced single mode operation in the presence of higher order transverse modes. (a) Measured emission spectrum from a coupled arrangement of evenly pumped microrings, comprised of various TE_0 and TE_1 modes. (b) Global single-mode operation in the PT arrangement. Selective breaking of PT symmetry is used to suppress the entire set of TE_1 modes as well as competing longitudinal TE_0 resonances. The minimum separation between the coupled rings is 50 nm.

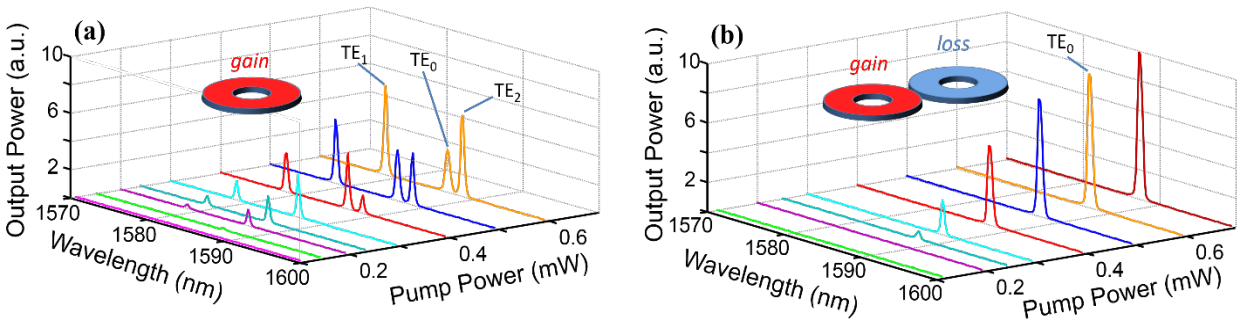

Figure 22. Comparison between the spectral evolution of a single microring laser and the corresponding PT-symmetric arrangement as a function of the pump power. (a) Higher order transverse modes TE_1 and TE_2 appear in the lasing spectrum of the single microring laser. (b) The PT laser remains single-mode.

It is also instructive to compare the output efficiency of the PT-symmetric laser with that of a standalone microring resonator. The characteristic light-light curves shown in Figure 23(a) demonstrate that despite a slightly higher lasing threshold, the PT arrangement exhibits approximately the same slope efficiency as the single ring. What is important, however, is that in the PT case, the entire power is now emitted into the broken-PT resonance, whereas in the single ring system it is shared among a mixture of competing modes (Fig. 23 (b)). It should be noted that the threshold in the PT system is set by the coupling between the rings and the loss of the un-pumped cavity and can be further modified through design (see Section 4.2).

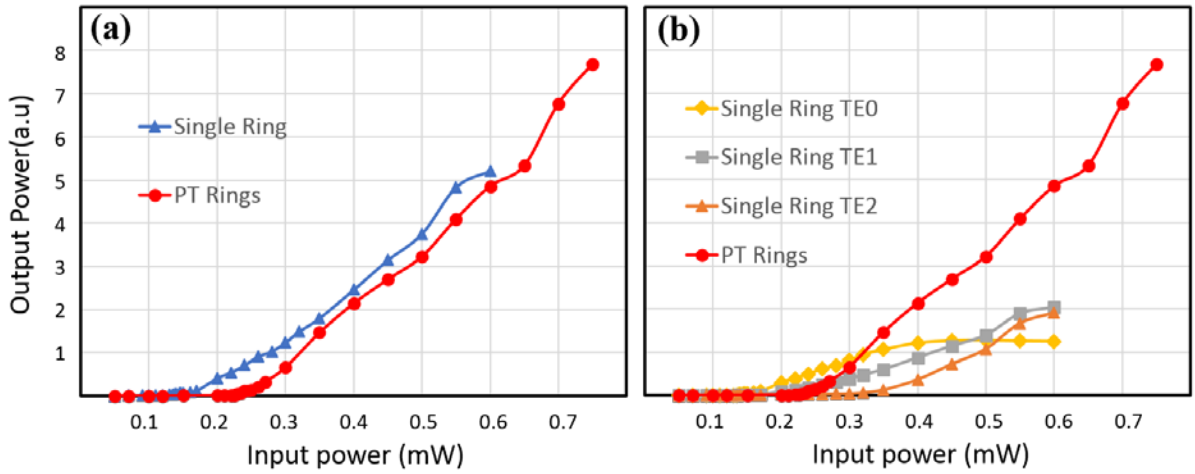

Figure 23. Light-light characteristics. (a) Despite a slightly higher lasing threshold, the PT-symmetric arrangement exhibits the same slope efficiency as an isolated microring. (b) The desired TE_0 mode of the PT system carries much higher power than any mode in the single microring. In the single ring, different transverse modes can be distinguished from their onset of lasing.

5.3. Robustness to perturbations and stability

The analysis in Section 5.1 assumes perfect PT-symmetric conditions, *i.e.*, two entirely identical rings exhibiting equal amounts of gain and loss. In practice, however, it may not always be possible to fulfill these conditions. To begin with, even if PT-symmetry is exactly held for one pair of modes, the wavelength dependence of the gain medium as well as the bending and scattering losses may cause deviations from this condition for the rest of the modes. In addition, due to the inter-dependence of refractive index and gain/loss (Kramers-Kronig relations), even structurally identical ring resonators can be detuned when being subjected to different pump energies. Yet, as we will show in this section, the strong coupling between the ring resonators makes the PT-symmetric mode selection technique resilient to some level of perturbation. To study this problem in a systematic way, we formulate a

situation where the gain/loss and the resonant frequencies in the two coupled resonators are not exactly equal. Following an approach similar to that outlined in section 4.1, we find the following self-consistent relationship between the fields in the two resonators (a_n and b_n):

$$\begin{cases} \frac{da_n}{dt} = -i\omega_{an}a_n + i\kappa_n b_n + \gamma_{a_n}a_n \\ \frac{db_n}{dt} = -i\omega_{bn}b_n + i\kappa_n a_n + \gamma_{b_n}b_n \end{cases} \quad (5.4)$$

where $\gamma_{a_n}$and γ_{b_n}represent the net gain (positive) or loss (negative) in each ring and $\omega_{a,bn}$ are the nth longitudinal resonance frequency of each ring (when isolated and passive), and κ represent the coupling between the rings. Note that if caused by perturbations, it is generally expected that the mismatch between the resonant frequencies of the rings to be small, therefore one can assume $\omega_{bn} = \omega_{an} + \Delta\omega$ where $\Delta\omega \ll \omega_{an,bn}$. On the other hand, the gain and loss can, in practice, significantly deviate from their exact PT balance. This is due to fact that the loss of the un-pumped ring is dictated by the absorption and scattering, while the gain in the pumped cavity can attain a wide range of values depending on the intensity of the pump. Again, by assuming an evolution of the form $(a_n, b_n) = (A_n, B_n)e^{-i\omega_n t}$, one can find the eigenfrequencies $\omega_n^{(1,2)}$ of the supermodes to be

$$\omega_n^{(1,2)} = \omega_{an} + \frac{\Delta\omega}{2} + i\frac{\gamma_{a_n}+\gamma_{b_n}}{2} \pm \sqrt{\kappa_n^2 - \left(\frac{\gamma_{a_n}-\gamma_{b_n}}{2} + i\frac{\Delta\omega}{2}\right)^2} \quad (5.5)$$

In order to visually illustrate how the system responds to deviations, the evolution of eigenfrequencies, when the gain in the active ring changes from 0 to 2κ are plotted in the complex plane for a double ring structure under perfect PT-symmetric conditions (Fig. 24(a)), and the same system subject to the above perturbations (Fig. 24(b)). As shown in Fig.

24(b), for the perturbed system, the eigenfrequencies are of a complex nature and the transition from the unbroken to the broken regime occurs in a more adiabatic fashion. However, regardless of these differences, as long as the deviations are well below the level required to fully decouple the two rings (around 10% of the coupling), the overall behavior of the modes remains the same. Therefore, by using strongly coupled resonators as demonstrated in this work, it is possible to achieve robust single mode operation despite small perturbations due to fabrication imperfections or pump-induced nonlinearities.

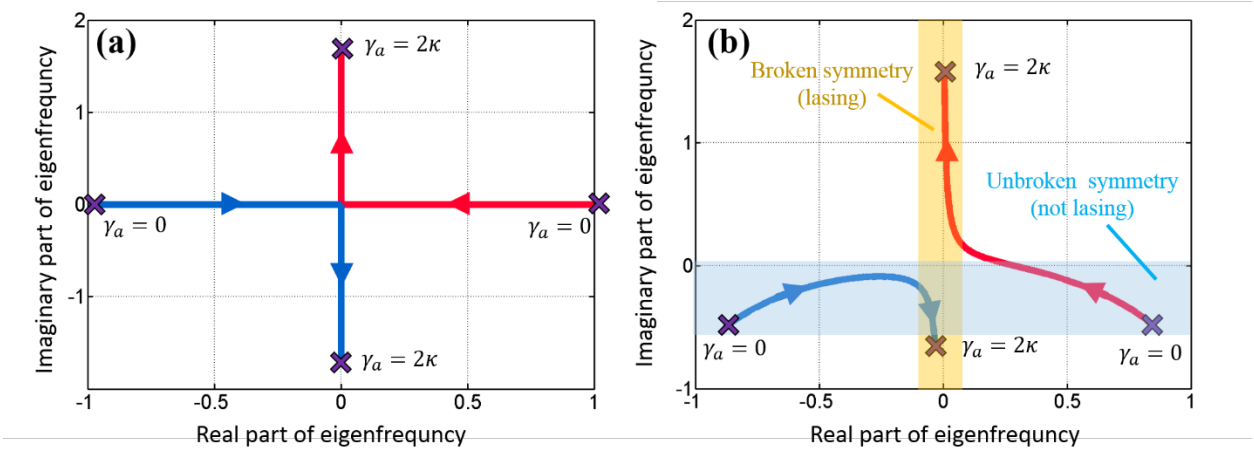

Figure 24. The real and imaginary parts of the normalized eigenfrequencies associated with (a) a perfectly PT-symmetric, and (b) a perturbed PT-symmetric coupled microring arrangements, where the gain in the active ring is varied from 0 to 2κ. The loss in the un-pumped resonator γ_{b_n}, and the phase mismatch $\Delta\omega$ are set to be κ and 0.03κ respectively. In the perturbed PT system, the general trends remain the same as long as the two rings are strongly coupled.

Along the same lines, the performance of the stability of PT-symmetric laser is also tested in the presence of temperature variations. In a single ring configuration, due to the presence of multiple competing modes, a slight shift of the amplification envelope may

severely impact the ensemble of the lasing modes. Figure 25(a) shows the temperature-induced shift of the photoluminescence spectrum of the quantum well active medium. Figure 25(b) compares the evolution of the emission spectra obtained from a conventional ring resonator and the PT-symmetric system as the sample temperature is externally varied. Interestingly, the self-adjusting properties of PT-symmetric mode stabilization seem to prevent mode-hopping effects. As a result, the lasing mode of the PT system remains stable and continuously shifts over a range of 3.3 nm by varying the temperature between 270 K and 300 K, while single-mode behavior is preserved with high fidelity. Thus, this scheme is shown to be substantially robust to ambient temperature changes in enforcing single mode operation.

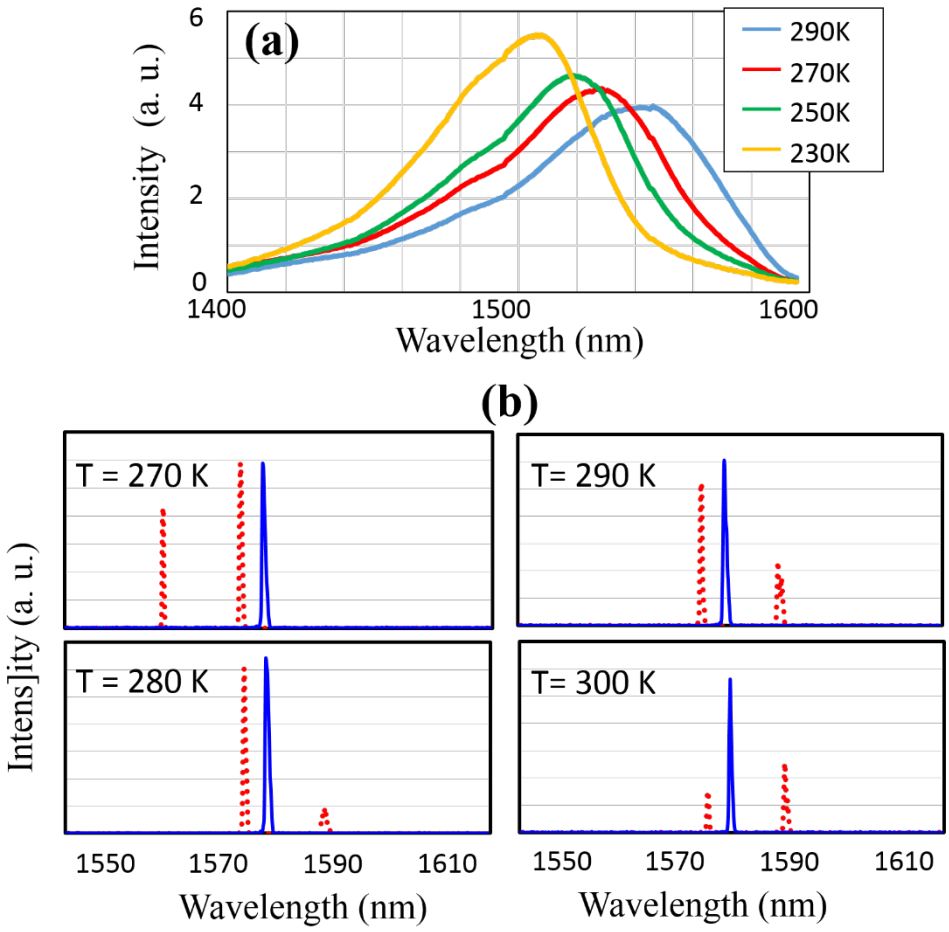

Figure 25. Continuous wavelength tuning of a PT-symmetric single-mode microring laser. (a) Measured photoluminescence of the InGaAsP wafer at different temperatures. (b) Emitted spectrum of the same PT-symmetric scenario shown in (a) (red line) compared to single ring scenario with the same ring dimensions (blue line). Continuous single mode tuning is achieved in the PT case while the multi-moded spectrum of a single ring laser undergoes severe mode-hoping by changing the temperature. (c) Emitted spectrum from a PT-symmetric microring structure at a temperature of 270 K, 280 K, 290 K and 300 K, and a pump power of 0.8, 1, 1.4, and 1.4 mW, respectively. The observed wavelength tuning is approximately 0.1 nmK^{-1}. The rings have a radius of 6 μm and a width of 500 nm and are placed 200 nm apart from each other.

CHAPTER 6:
DIRECT MODULATION OF PT-SYMMETRIC LASERS

Telecommunication is one of the fundamental areas of application for semiconductor lasers. In order to utilized the lasers for high speed data transmission, one should be able to modulate their output with microwave frequencies. The upper frequency limit of such a modulation defines the information carrying capacity of an optical communication system. One of the common approaches for these high frequency operations is to directly modulate the output amplitude of semiconductor lasers by varying the current flow through the device. However, the modulation speed in most of current semiconductor settings is limited due to large photon life times in the cavities. In this chapter, we theoretically show that the frequency response of a semiconductor laser can be broadened, if the system is paired with a lossy partner in a PT-symmetric fashion, and biased close to the exceptional point.

6.1. Gain derivatives enhancement

To study the small signal modulation response of PT-symmetric coupled microrings, we assume that the laser always operates in the broken PT-symmetric regime. As we know material gain approximately is a linear function of number of carriers:

$$g_m = \frac{\sigma_g}{V}(N - N_0) \quad (m^{-1}) \qquad (6.1)$$

where g_m is the material gain at the wavelength of operation, σ_g is the gain cross section, N is the number of carriers, and N_0 is the number of carriers at transparency. Thus, the modal gain of the active ring can be written as,

$$G_r = \Gamma v_g g_m = G_{rN}(N - N_0) \quad (s^{-1}), \qquad (6.2)$$

where $G_{rN} = \Gamma v_g \sigma_g / V$ and v_g is the mode group velocity in the ring. If the system is lasing beyond PT symmetry breaking point, the gain associated with the mode residing in the active resonator represents the stimulated emission rate (G). For a typical microring laser, the stimulated emission rate is linearly related to the gain of the cavity. However, in the case of the PT laser, it is a more elaborate function of total loss of the un-pumped cavity and the coupling strength between the rings, as well as the gain in the pumped resonator (G_r). Equation (6.3) shows the dependence G to the different parameters of the system as derived in chapter four.

$$G = \frac{G_r - \alpha}{2} + \sqrt{\left(\frac{G_r + \alpha}{2}\right)^2 - \kappa^2} \qquad (6.3)$$

Using the equation (6.3), the parameters of the system can be designed such that the threshold of lasing and PT breaking be equal. Once the system is designed, we consider the attenuation in the lossy ring and the coupling strength to be constant for the calculations regarding small signal modulation. Therefor one can find that the dependence of the stimulated emission to any parameter in the PT-laser is a linear funcation derivative of the gain in the active ring with respect to the same parameter. This relation is showed as

$$\frac{dG}{dx} = A \times \frac{dG_r}{dx} \qquad (6.4)$$

where x is number of photons or carriers. We call A the derivative enhancement factor which express the difference between an isolated mirroring laser and the corresponding PT-symmetric microring laser arrangement. Equation (6.5) is the expression for A derived simply from applying the chain rule to (6.3),

$$A = \frac{1}{2} + \left(\frac{G_r + \alpha}{2}\right) / \sqrt{(G_r + \alpha)^2 - 2\kappa^2}. \qquad (6.5)$$

Therefore, A is always equal to one for a single mirroring laser. The amount of A with respect to gain/loss to coupling ratio is also plotted in Fig. 26 for the PT scenario when the gain and loss in the cavities are equal. According to Fig. 26, the enhancement factor increases considerably as the system approaches the PT-symmetry breaking or exceptional point. In the next section, we show how this enhancement coefficient can improve the modulation response of the system by increasing the relaxation oscillation frequency and the damping factor.

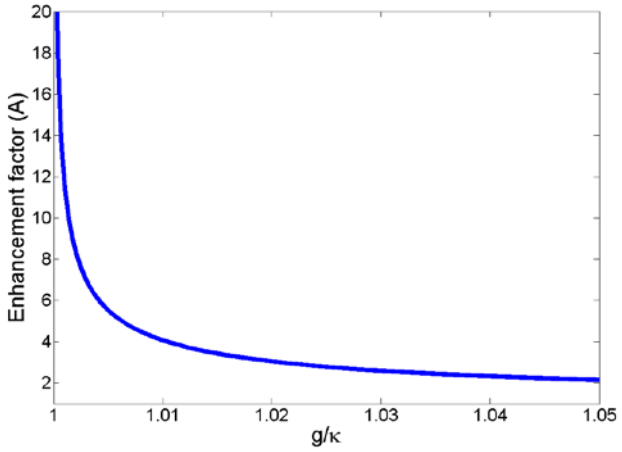

Figure 26. Enhancement of the derivative of the modal gain in the PT-symmetric case over isolated microring laser with respect to gain/loss over coupling ratio.

6.2. Small signal modulation response of a PT-laser

In order to find the modulation response in the PT-symmetric case, one can start with the rate equations. If P is the number of photons and N is the number of carriers in the laser cavity, following the method in [20] we have

$$\begin{cases} \frac{dP}{dt} = GP + R_{sp} - \frac{P}{\tau_p} \\ \frac{dN}{dt} = \frac{I}{e} - \frac{N}{\tau_c} - GP \end{cases}, \quad (6.6)$$

where G and R_{sp} are the net rate of stimulated and spontaneous emissions, respectively, I is the injected current, τ_p and τ_c represent the photon and carrier lifetimes, and e is the electric charge of an electron. The equation for G is already derived in the previous section. R_{sp} also can be ignored, since we are only interested at the behavior of the laser above the lasing threshold. Also, for simplicity, one can ignore the injection efficiency and output efficiency in the rest of the calculations.

Let's consider the laser to be biased at the current I_0 (number of carriers and photons to be N_{th} and P_0 respectively) at steady state. From the rate equations, one can derive,

$$G_0 = \frac{1}{\tau_p} \quad (6.7)$$

$$P_0 = \frac{\tau_p}{e}\left(I - \frac{eN_{th}}{\tau_c}\right) = \frac{\tau_p}{e}(I - I_{th}) \quad (6.8)$$

By adding a small modulation current *i(t)* to the bias current we have:

$$\begin{cases} I(t) = I_0 + i(t) \\ P(t) = P_0 + p(t) \\ N(t) = N_{th} + n(t) \end{cases} \quad (6.9)$$

The stimulated emission rate also can be approximated by the first order Taylor expansion to be,

$$G = G_0 + \frac{\partial G}{\partial N}n(t) + \frac{\partial G}{\partial P}p(t), \quad (6.10)$$

where the gain saturation effect is represented in the last term of the equation. Inserting (6.9) and (6.10) in (6.6), and ignoring the second order terms of $i(t)$, $p(t)$, and $n(t)$, we have

$$\begin{cases} \frac{dp}{dt} = \Gamma_{PP}p(t) + \Gamma_{PN}n(t) \\ \frac{dn}{dt} = \Gamma_{NP}p(t) + \Gamma_{NN}n(t) + i(t)/e \end{cases} \quad (6.11)$$

where

$$\Gamma_{pp} = \frac{\partial G}{\partial P}P_0 \quad (6.12)$$

$$\Gamma_{PN} = \frac{\partial G}{\partial N}P_0 \quad (6.13)$$

$$\Gamma_{NP} = -G_0 - \frac{\partial G}{\partial P}P_0 \quad (6.14)$$

$$\Gamma_{NN} = -\frac{\partial G}{\partial N}P_0 - \frac{1}{\tau_c} \quad (6.15)$$

In equation (6.15), it is assumed that carrier lifetime dependence to the number of carriers is negligible. In the next step, one can assume that the modulation current to be a sinusoidal function with the angular frequency of ω_0. Under small signal approximation, the photon and carriers are expected to oscillate sinusoidally with the same frequency around the bias values. Thus,

$$\begin{cases} i(t) = I_m Re\{e^{-j\omega_0 t}\} \\ p(t) = P_m Re\{e^{-j\omega_0 t}\} \\ n(t) = N_m Re\{e^{-j\omega_0 t}\} \end{cases} \quad (6.16)$$

Using equation (7.16), one can rewrite equation (7.11) as

$$\begin{cases} (\Gamma_{PP} + j\omega_0)P_m + \Gamma_{PN}N_m = 0 \\ \Gamma_{NP}P_m + (\Gamma_{NN} + j\omega_0)N_m = -I_m/e \end{cases} \quad (6.17)$$

This can be easily solved by Cramer's rule to find the amount of P_m with respect to I_m,

$$P_m = \frac{\Gamma_{PN}I_m/e}{(\Gamma_{PP}+j\omega_0)(\Gamma_{NN}+j\omega_0)-\Gamma_{PN}\Gamma_{NP}} \quad (6.18)$$

which can be written as

$$P_m = \frac{\Gamma_{PN} I_m/e}{\omega_R^2 - \omega_0^2 + j\gamma\omega_0} \quad (6.19)$$

where

$$\omega_R = (\Gamma_{PP}\Gamma_{NN} - \Gamma_{PN}\Gamma_{NP})^{1/2} \quad (6.20)$$

and

$$\gamma = \Gamma_{PP} + \Gamma_{NN} \quad (6.21)$$

ω_R and γ are defined as the relaxation oscillation frequency and the damping factor respectively. Hence, the frequency response of the photon number in the system for a small signal excitation can be written as

$$H(\omega_0) = \frac{P_m(\omega_0)}{P_m(0)} = \frac{\omega_R^2}{\omega_R^2 - \omega_0^2 + j\gamma\omega_0} \quad (6.22)$$

Now, let's consider the PT-symmetric laser again. In this system, the gain associated with the active resonator can be described by

$$G_r = G_{rN}(N - N_0)(1 - \epsilon_{sat}P). \quad (6.23)$$

ϵ_{sat} expresses the gain suppression in the pumped cavity for large values of P. Consequently, we can find the derivative of G_r with respect to P and N at for a particular bias values,

$$\frac{dG_r}{dN} = G_{rn}(1 - \epsilon_{sat}P) \approx G_{rN} \quad (6.24)$$

$$\frac{dG_r}{dP} = -\epsilon_{sat}G_{rn}(N_{th} - N_0) \approx -\epsilon_{sat}G_0 \quad (6.25)$$

However, using equation (6.4), for the gain of the lasing mode beyond PT symmetry breaking we have,

$$\frac{dG}{dN} = A\frac{dG_r}{dN} \approx AG_{rN} \quad (6.26)$$

$$\frac{dG}{dP} = A\frac{dG_r}{dP} \approx -A\epsilon_{sat}G_0 \quad (6.27)$$

where A is the enhancement factor (depends on various parameters of the PT-system), that is fully described in the first section. And as mentioned before, it indicates the difference between a single microring laser and a PT symmetric microring laser configuration. Also $G_{rN} = \Gamma v_g \sigma_g / V$ and $G_0 = \frac{1}{\tau_p}$. Thus, one can rewrite equations (6.12)-(6.15) as,

$$\Gamma_{PP} = -A\epsilon_{sat} G_0 P_0 \quad (6.28)$$

$$\Gamma_{PN} = A G_{rN} P_0 \quad (6.29)$$

$$\Gamma_{NP} = -G_0 \quad (6.30)$$

$$\Gamma_{NN} = -A G_{rN} - \frac{1}{\tau_c} \approx -\frac{1}{\tau_c} \quad (6.31)$$

Therefore, one can write,

$$\Gamma_{PP}^{\mathrm{PT}} = A\Gamma_{PP}^{single} \quad (6.32)$$

$$\Gamma_{PN}^{\mathrm{PT}} = A\Gamma_{PN}^{single} \quad (6.33)$$

$$\Gamma_{NP}^{\mathrm{PT}} = \Gamma_{NP}^{single} \quad (6.34)$$

$$\Gamma_{NN}^{\mathrm{PT}} = \Gamma_{NN}^{single} \quad (6.35)$$

Hence, from (7.20), one can derive:

$$\omega_R^{PT} = \sqrt{A}\,\omega_R^{single} \quad (6.36)$$

Figure 27(a) shows the frequency response of a single microring laser versus the PT symmetric arrangement when operating at $I = 1.005 I_{th}$ and $I_{th} = 1mA$. The photon life time considered to be the same for both cases. As it is clear in Fig. 27(a), considerable improvement in the small signal frequency response can be achieved just by introducing an identical but lossy cavity to a semiconductor microring laser. The transient respond of the two systems is also compared in Fig. 27(b).

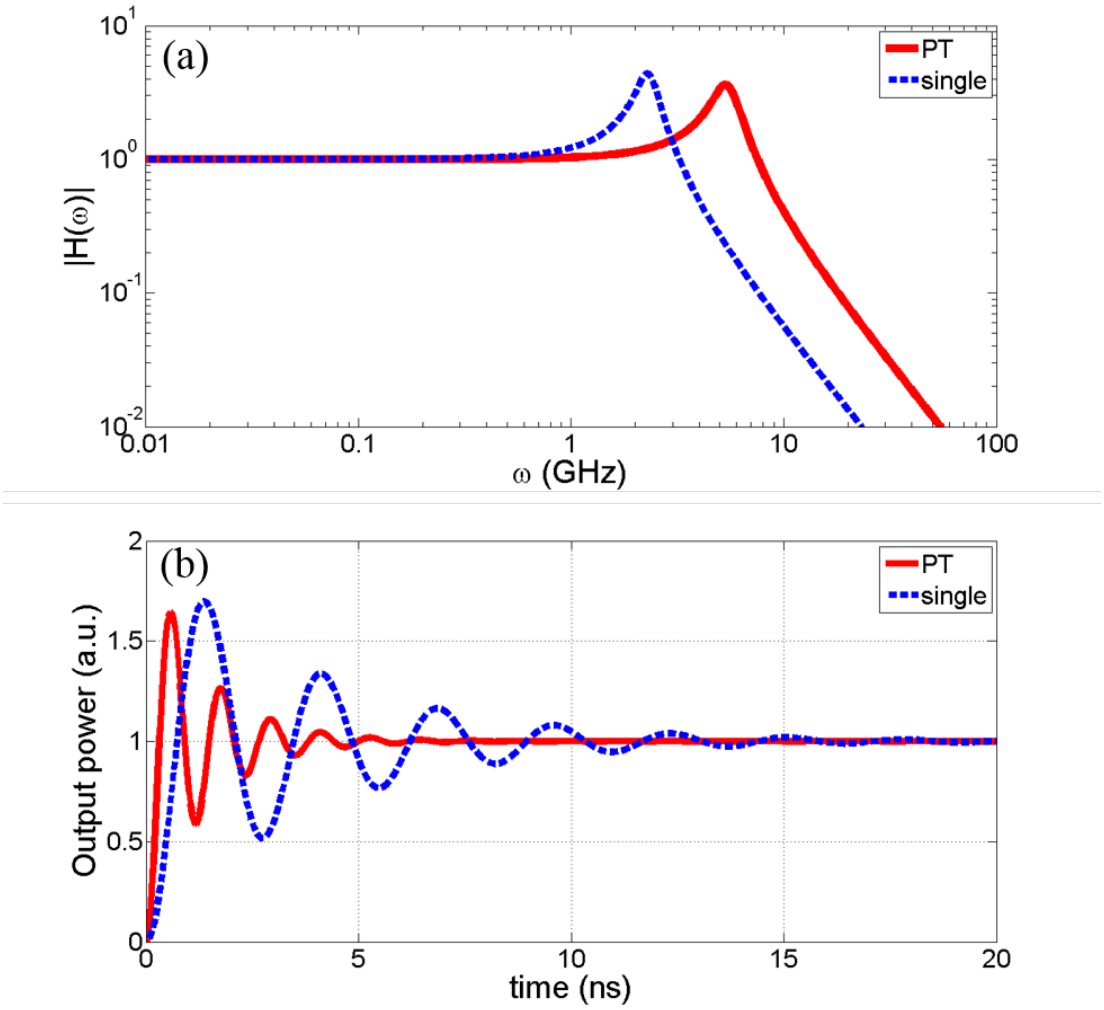

Figure 27. (a) Frequency response of an isolated microring laser (dashed blue line) versus the PT-symmetric configuration of the same resonator (solid red line). (b) transient response of an isolated microring laser (dashed blue line) versus the PT symmetric configuration of the same resonator (solid red line) when a step current with amplitude of $(I_0 - I_{th})/2$ is applied to the pumped cavity.

CHAPTER 7: DARK STATE LASERS

In this section, we present the theoretical analysis and the experimental demonstration of single mode operation in dark state lasers through the physics of non-Hermitian EPs. The structure is based on a coupled microring layout [84]. This dual cavity configuration is implemented on the same InP based multi-quantum-well semiconductor gain material as in previous chapters. In this system, single frequency emission was enforced with more than a 30 dB side-lobe mode suppression. In addition, over one free spectral range of continuous wavelength tunability is demonstrated by simply adjusting the ambient temperature. Figure 28(a) provides a schematic of the configuration used in our experiments. This arrangement is comprised of two dissimilar microring resonators (same widths and heights, different radii), indirectly coupled to each other via a central waveguide. The cross-section of the three identical guides is designed so as to favor a single transverse TE mode. Fig. 28(b) depicts an SEM image of the fabricated structure. The results in this chapter have been published in [85].

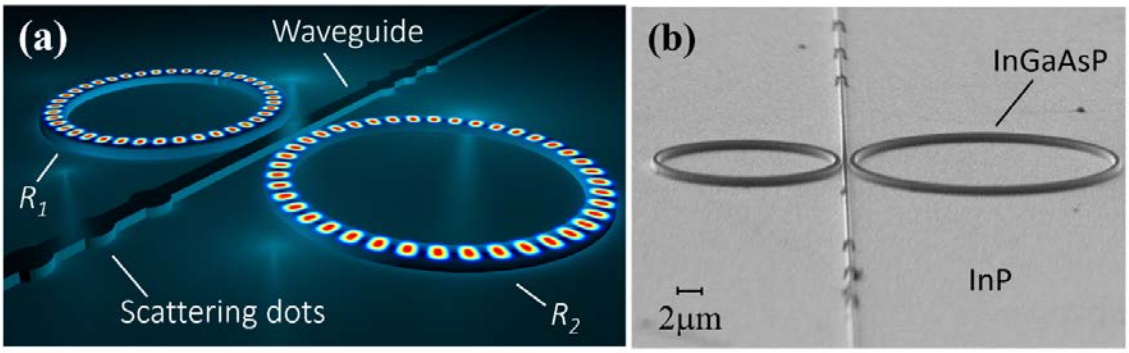

Figure 28. (a) Schematic of a dark state laser. The dots on the middle waveguide are used to scatter the light in this channel for detection. (b) An SEM image of the dark state laser system at an intermediate fabrication step.

7.1. Theoretical model

The presence of exceptional points and the ensuing mode discrimination in the above dark state arrangement can be understood by investigating the corresponding eigenvalue spectrum (Fig. 29). The passive dark state arrangement without any intrinsic gain or loss is considered in this analysis. Here, the eigenfrequencies and eigenmodes of the system can be determined using temporal coupled mode formulations. By considering a longitudinal resonance frequency of the system, the equations representing the evolution of the fields in the two resonators and the bus waveguide can be written as follows:

$$\begin{cases} \frac{da}{dt} = -i\omega_1 a - \gamma a - \gamma c + i\mu b_i \\ b_o = b_i + i\mu a + i\mu c \\ \frac{dc}{dt} = -i\omega_2 c - \gamma c - \gamma a + i\mu b_i \end{cases} \quad (7.1)$$

In this model, the ring resonators are viewed as two oscillators with field amplitudes $a(t)$ and $c(t)$, normalized in such a way that $|a(t)|^2$ and $|c(t)|^2$ represent stored energies, b_i and b_o represent the amplitudes of the input and output waves in the bus channel normalized to the power, $\omega_{1,2}$ are the resonance frequencies of the rings, and finally μ is the coupling coefficient between each resonator and the bus waveguide. In this analysis, γ represents the out-coupling loss of the two cavities. Note that μ and γ are not independent parameters and conservation of energy demands that $\mu = \sqrt{2\gamma}$ [86]. Assuming eigenmode solutions of the form $(a, c) = (a_0, c_0)e^{-i\omega t}$, one can find the longitudinal eigenfrequencies to be:

$$\omega_n^{(1,2)} = \left(\frac{\omega_1+\omega_2}{2}\right) - i\gamma \pm \sqrt{\left(\frac{\omega_1-\omega_2}{2}\right)^2 - \gamma^2}. \quad (7.2)$$

Moreover, the associated eigenmodes can be written as:

$$\binom{a_0}{c_0}_{1,2} = \begin{pmatrix} 1 \\ i\delta \pm \sqrt{1-\delta^2} \end{pmatrix} \qquad (7.3)$$

where $\delta = (\omega_2 - \omega_1)/(2\gamma)$.

When the resonance frequency of the two dissimilar rings are relatively far away from each other ($(\omega_1 - \omega_2)^2 \gg 4\gamma^2$), Eq. (7.2) reveals that the eigenfrequencies bifurcate in the real domain. In this scenario, such *uncoupled modes* endure a significant amount of loss as a result of the power out-coupling to the central channel and remain below lasing threshold as indicated in Fig. 29(c). The system is exactly at the exceptional point when the detuning between the two rings satisfies $(\omega_1 - \omega_2) = \pm 2\gamma$. At this singular point, the two eigenfrequencies and their respective eigenvectors coalesce as indicated by Eqs. (7.2) and (7.3). Finally, if $(\omega_1 - \omega_2)^2 \ll 4\gamma^2$, the system is operating beyond the phase transition point. In this case, the two coinciding resonances tend to fuse in the real domain while they split along the imaginary axis. In other words, the two emerging supermodes will resonate at the same frequency, having two very different quality-factors ($Q = |\omega_R \,/\, (2\omega_I)|$).

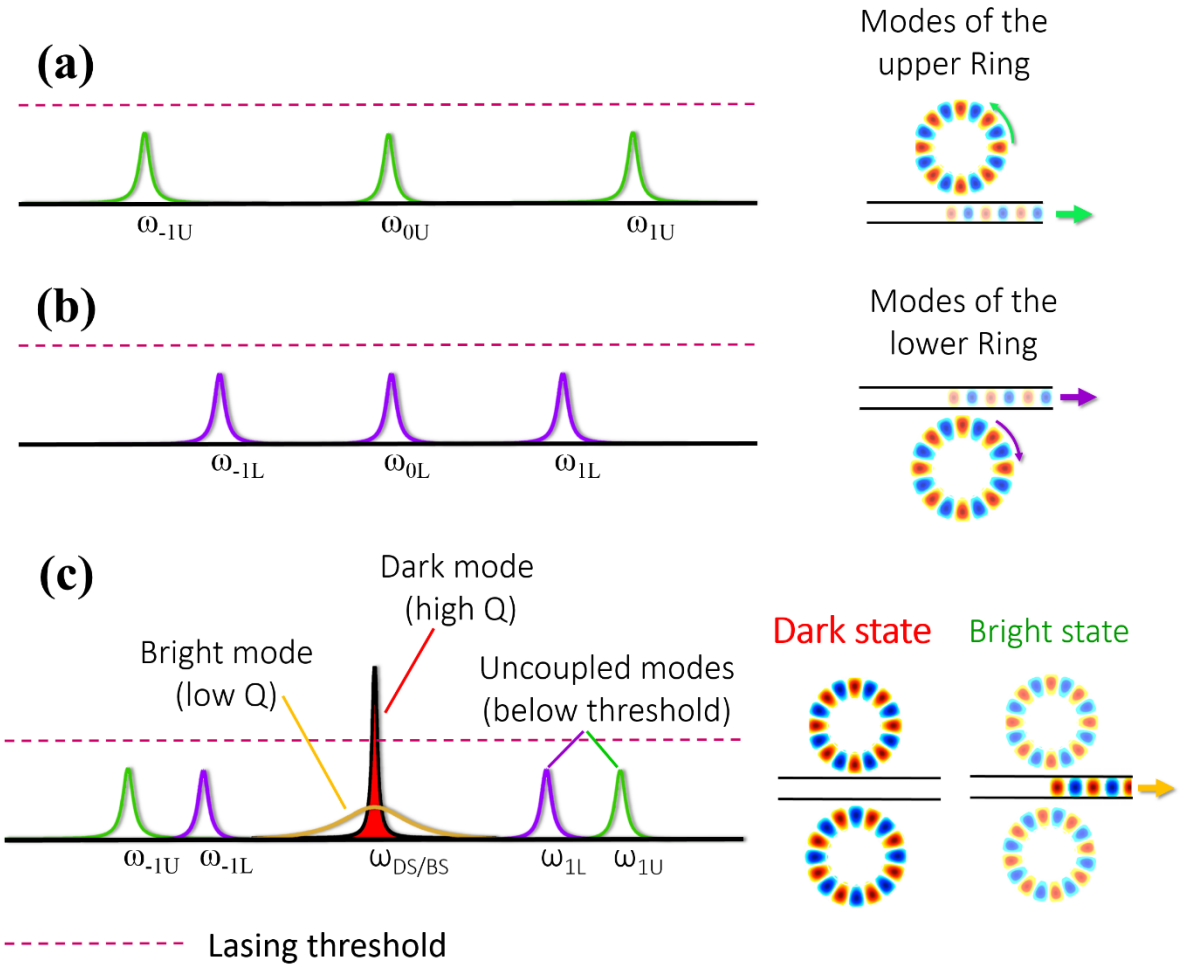

Figure 29. Principle of operation of a microring-based dark state laser. (a) Due to out-coupling losses, all the longitudinal modes of the upper microring have a low Q-factor and therefore a high lasing threshold (dashed line). (b) Similarly, modes of the lower microring cannot reach lasing threshold. (c) In a dark state arrangement, the spectrally coinciding modes form a pair of bright and dark modes. While the bright state loses a significant fraction of its energy to the central waveguide, the dark state has zero overlap with this channel and therefore has a high Q-factor and a low lasing threshold. The difference between Q-factors are conveyed in the depicted linewidths of the resulting dark and bright states.

Intuitively, one can understand this process as follows. In a dark state laser, the central waveguide plays the role of a mode dependent loss element. Equation (7.3) indicates that in such a configuration, the fields of the two coalesced supermodes are approximately in-phase and π-out-of-phase within these two rings. Given that the symmetric in-phase mode strongly excites the central waveguide through constructive interference, a considerable amount of energy is expected to be irreversibly lost through this channel. On the other hand, the anti-symmetric π-out-of-phase mode (dark state) does not inject light into the middle channel and hence experiences minimum attenuation. In this latter scenario, the mode remains well-confined within the two rings as shown in the inset of Fig. 29(c). Note that, this is consistent with the results of the Eqs. (7.2) and (7.3). Since any non-coinciding resonance associated with the two dissimilar rings endures a significant amount of loss through coupling to the central waveguide, in the presence of gain, the anti-symmetric dark state mode is the first in line to lase with a large margin for mode discrimination. Therefore, the emergence of an exceptional point in such a non-Hermitian open configuration enables single mode lasing.

7.2. Experimental results

In this section, we present the experimental results regarding the formation of dark state modes in a microring system. The central waveguide as well as the microrings involve InGaAsP multiple quantum wells and are surrounded by low index dielectrics (SiO2 and air). The microrings were optically pumped with a 1064 nm laser beam (SPI fiber laser) focused onto a circular area with the diameter of ~100 μm on the sample surface. The intensity

profile is captured via an IR CCD camera, and the emission spectrum is collected using a monochromator with the resolution of 0.4 nm. The reported pump power is calculated by taking the ratio of the ring top surface area aperture to the pump laser spot size and multiplying it by the total pump laser power. Only the output power collected by the objective lens is considered for the reported results. Finally, controlling the temperature is performed by placing the structures in a continuous-flow cryostat (Janis ST-500). Using a closed loop controller, the temperature was varied from room temperature down to 110K.

Figure 30 shows the emission characteristics of a dark state structure comprising of two microrings with radii of 9 μm and 11 μm (width: 500 nm, height: 210 nm) separated by a waveguide of an identical cross section, centered at a distance of 200 nm from each of the two rings. Single mode lasing is achieved at room temperature under pulsed pumping conditions (pulse width: 15 ns, repetition rate: 290 KHz). In order to ensure that the observed mode is of the dark state type, the spectrum of this two-ring configuration (Fig. 30(e)) is compared to that obtained from the lower and upper rings when they are pumped individually (Figs. 30(a,c)). As expected, independently, each ring exhibits lasing in a multiple number of modes. However, when a resonance from the upper microring happens to be in close proximity to another one of the lower ring, a dark state mode emerges as the fundamental oscillation in this coupled system (Fig. 30(e)). Given that the dark state mode has a larger Q-factor and a lower threshold with respect to the rest of the modes, it can deliver much higher output power by depleting the pool of charge carriers. This prevents the lasing of uncoupled modes in Fig. 30(e), although the supplied pump power is the same as in Fig. 30 (a) and (c). In order to observe the light intensity in the middle waveguide, a set of

scatterers has been intentionally implanted in the central channel, away from the coupling region as shown in Figs. 28 (a) and (b). As Fig. 30 (b) and (d) show, the scatterers in the middle channel light up when the resonances of the individual rings are excited. On the other hand, these same centers appear dim when only a dark state mode is present, i.e. when both rings are pumped simultaneously (Fig. 30(f)). This also confirms the emergence of a single mode spectrum under dark state conditions. The characteristic light-light curve associated with the configuration when operating in the dark mode is compared to that when only one of the rings is pumped (see Fig. 31). The lower threshold and higher efficiency of the dark state mode indicate a significantly larger quality factor, in agreement with theoretically anticipated results. Our further measurements show that the dark sate laser remains single-moded with SMSR of 30 dB (see Fig. 32) throughout a wide range of pump powers (more than five times the threshold pump power).

As Eq. (7.1) indicates, any detuning between the resonances of the two rings compromises the quality factor of the dark state but allows some power outflow through the central channel [84]. However, using this scheme for out-coupling reduces the mode discrimination between the dark state and the adjacent uncoupled modes. Therefore, an effective method of extracting light from the device, while preserving the inherent mode discrimination, is to incorporate bus waveguides on either ends of the two rings.

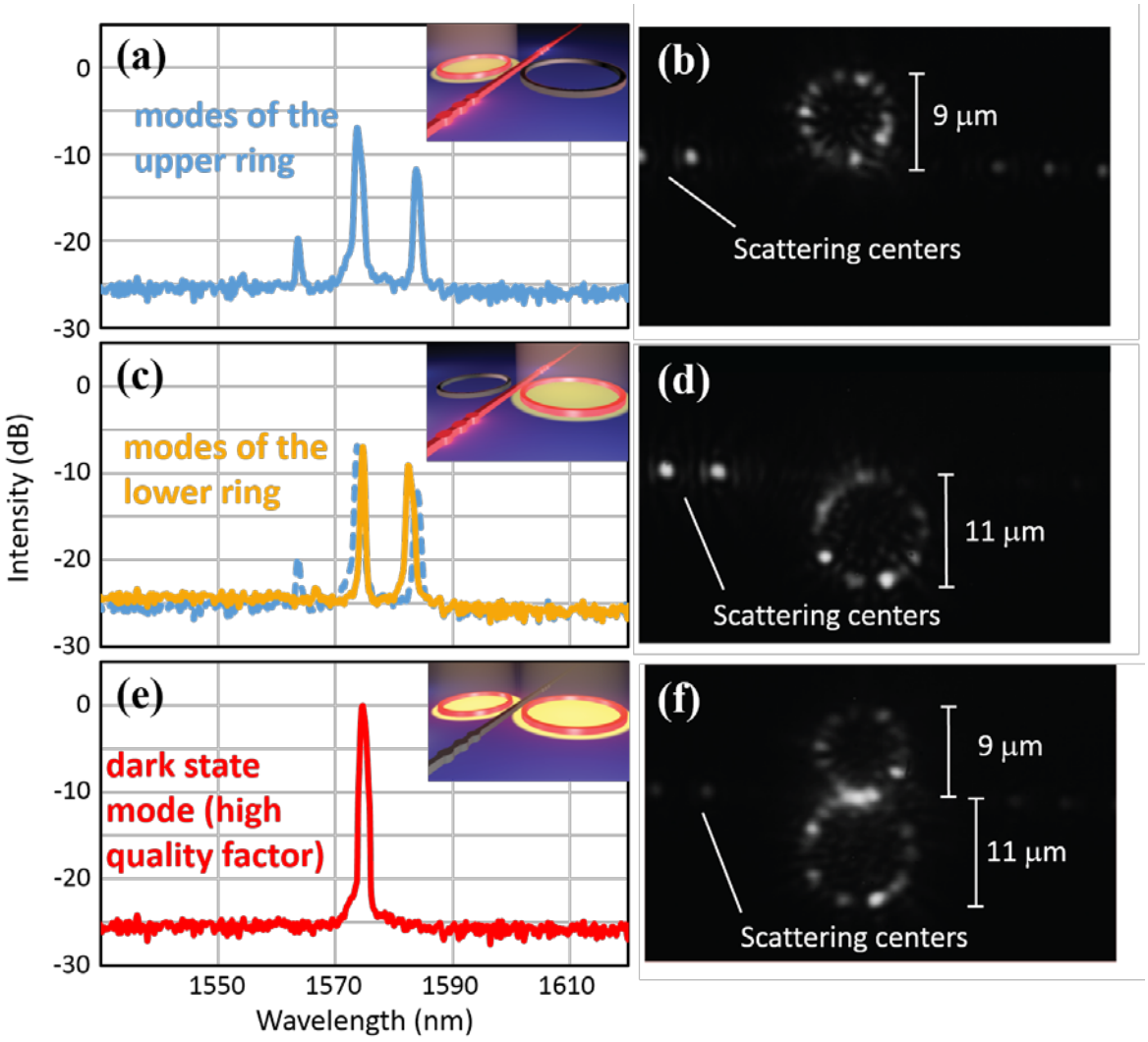

Figure 30. Experimental demonstration of dark state laser at room temperature. (a) Emission spectrum of the upper microring when illuminated by the pump beam (peak pump power: 1.2mW). In this regime, several longitudinal modes are lasing within the gain bandwidth. (b) Corresponding intensity pattern as obtained from scattering imperfections. The presence of light in the central waveguide is observed from the bright scattering centers. (c) and (d), same as in (a) and (b) when the lower ring is pumped at the same power level, the dotted line in (c) is depicting the spectrum of the upper ring for comparison. (e) When both rings are pumped at the same power densities as in (a) and (c), the double ring system lases in a single dark mode emerged from two coalescing longitudinal frequencies. (f) In this case, small emission is seen from the scattering dots, indicating insignificant excitation of the central waveguide compare to the first two cases.

Note that both a dark state laser and a parity-time symmetric laser utilize exceptional points of open (non-conservative) systems to enforce single-mode operation in microring systems. In a parity-time symmetric arrangement, the exceptional point arises through the interplay between gain and loss. (In practice, this was enabled by non-uniform pumping of the two rings or by a unidirectional grating.) In a dark state laser, the pump is uniform across the two rings, and the exceptional points emerge due to the presence of the central waveguide that operates as a mode-dependent loss channel.

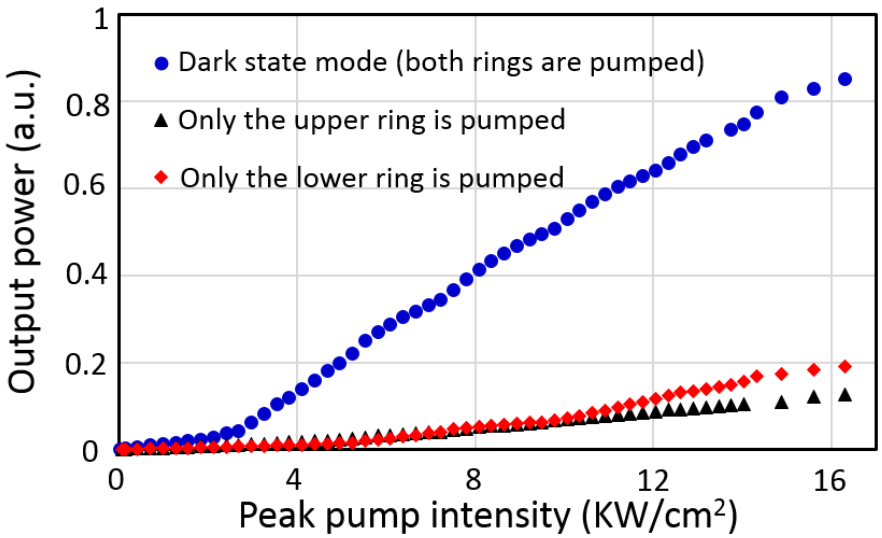

Figure 31. Light-light curves associated with dark state mode (when both rings are pumped), and when either the upper or lower rings is pumped. In addition to the remaining single mode for the entire pump power range, the dark state configuration shows lower lasing threshold, higher slope efficiency, and enhanced total output power.

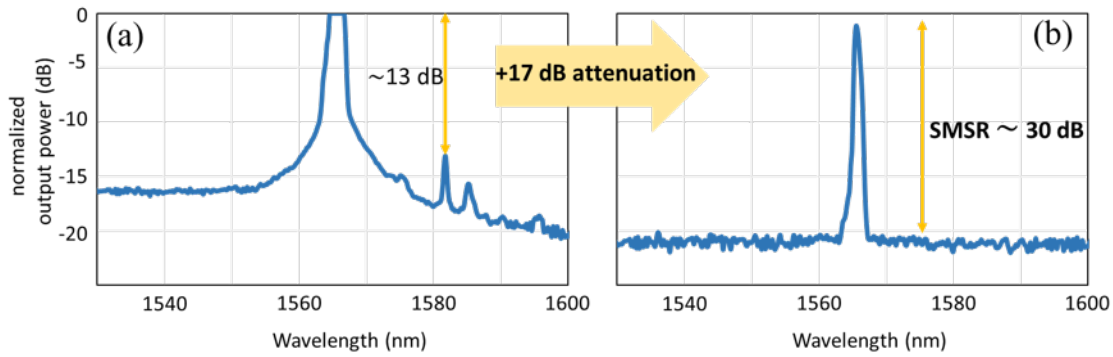

Figure 32. (a) Emitted spectrum of the dark state laser at the pump power of $5P_{th}$. The main lobe is allowed to be saturated in order to see the side lobes (b) the lasing spectrum under the same pumping condition after 17 dB attenuation. Overall, the SMSR of the dark state laser is on the order of 30 dB.

Finally, due to the Vernier effect, dark state modes occur at a discrete set of wavelengths where the resonances of the upper and lower rings are sufficiently close to coalesce. As a result, the free spectral range in such a resonator system can be increased substantially since it is determined by the relative radii of the two rings. This ability to extend the free spectral range without reducing the radii of the microrings (thus avoiding bending losses) could have important ramifications in designing laser cavities and spectral filters. Evidently, a wider free spectral range is desired in applications where laser wavelength tuning is intended. Fig. 33 shows the spectral tuning of a dark state laser. As large as one free-spectral-range of hop-free tuning is achieved by means of adjusting the ambient temperature. This continuous tunability range can be further extended by applying an offset differential temperature to the rings [84].

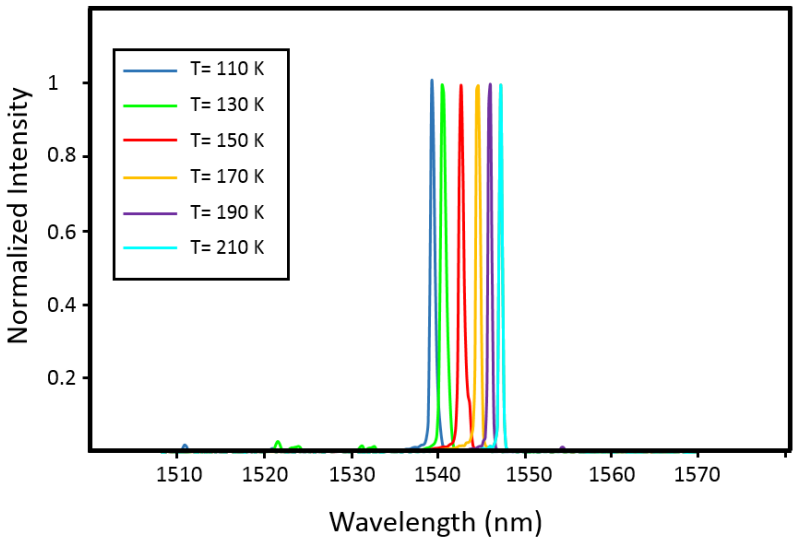

Figure 33. Wavelength tunability of a double-ring dark state laser. Over 8 nm wavelength tuning is demonstrated for a single mode under dark state lasing conditions by just varying the ambient temperature. This range is limited only by the temperature-induced photoluminescence shift. The radii of the two rings are 10 and 9 μm, associated with a free spectral range of 8 and 9 nm, respectively. This leads to a free spectral range of 72 nm for dark state modes.

CHAPTER 8:
ENHANCED SENSITIVITY IN PT-SYMMETRIC COUPLED CAVITIES

Optical micro-cavities are nowadays the subject of numerous studies, both in the scientific and technological domain. Their high quality factors can lead to strong light-matter interactions- a highly desirable attribute in many applications, especially those pertaining to sensing. Optical sensors can transduce small physical or chemical changes in the cavity's environment into a shift of the resonant frequency, which can be then detected [35]. However, improving the detection limit of these devices is often hindered by the resonator's Q-factor and the available spectroscopic resolution. Clearly of importance will be to devise new methodologies capable of improving the sensitivity of such devices. Recently, the bifurcation properties associated with exceptional points have been proposed as a potential means to increase the sensitivity of an optical resonator system to external perturbations [39], [87], [88].

In this chapter, we propose and demonstrate a novel class of ultra-sensitive photonic molecules based on the physics of exceptional points in PT-symmetric coupled microring arrangements involving two and three resonators. We show that this effect can be amplified by exploiting higher-order exceptional points in PT-arrangements with higher number of resonators. These active structure involves InP-based semiconductor quantum wells and the gain-loss profile is imposed by actively shaping the optical pump beam. In all cases, the resonance frequencies are fine-tuned using micro-heaters. By doing so, one can independently control the real and the imaginary components of the refractive index distribution, which is essential for establishing higher-order exceptional points in these

photonic molecules. The resulting bifurcations in the frequency domain are then monitored and characterized by allowing the system to experience net gain. The fabricated micro-heaters are also utilized to apply thermal perturbations on individual micro-cavities.

8.1. Binary systems

In this section, we provide the analysis and experimental demonstration regarding the enhanced sensitivity of a binary PT-symmetric photonic molecule to thermally induced perturbations. This system can be constructed by coupling an active optical cavity to an identical however lossy partner. Figure 34 schematically depicts such an arrangement.

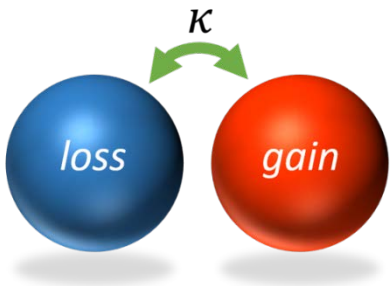

Figure 34. Schematics of a binary PT-symmetric photonic molecule arrangement.

Here, one cavity (a) experiencing gain g while its counterpart (b) is subjected to an equal amount of loss ($-g$). In the time domain, considering the base $e^{i\omega t}$, the field evolution obeys the following coupled differential equations:

$$i\frac{d}{dt}\begin{pmatrix} a \\ b \end{pmatrix} = \begin{pmatrix} ig & \kappa \\ \kappa & -ig \end{pmatrix}\begin{pmatrix} a \\ b \end{pmatrix} \qquad (8.1)$$

Using the representation $(a, b)^{\mathrm{T}} = V_n e^{-i\omega_n t}$, Eq. (7.1) corresponds to the eigenvalue equation $HV_n = \omega_n V_n$. The matrix H is

$$H = \begin{pmatrix} ig & \kappa \\ \kappa & -ig \end{pmatrix}. \qquad (8.2)$$

Setting $\mathrm{Det}(H - \omega_n I) = 0$, the corresponding characteristic equation is

$$\omega_n{}^2 = \kappa^2 - g^2 \qquad (8.3)$$

which leads to

$$\omega_{-1,1} = \pm\kappa\sqrt{1 - \left(\frac{g}{\kappa}\right)^2} \qquad (8.4)$$

In this configuration, PT-symmetry is unbroken under the condition that $g < \kappa$. this implies that the two eigenvalues in Eq. (8.4) are real. However, for $g > \kappa$, the two eigenvalues become imaginary and the system is said to have entered a broken symmetry phase. Interestingly, when $g = \kappa$, the system is at its second-order exceptional point, where the eigenvalues coalesce ($\omega_{-1} = \omega_1 = 0$). Similarly, to the case of third-order exceptional points the eigenvectors of the arrangement fuse at the singular point

$$V_{-1} = V_1 = \begin{pmatrix} 1 \\ -i \end{pmatrix} \qquad (8.5)$$

The generalized perturbed Hamiltonian for this binary configuration can be written as,

$$H = \kappa \begin{pmatrix} i\tilde{g} & 1 \\ 1 & -i\tilde{g} \end{pmatrix} + \kappa \begin{pmatrix} \epsilon_1 & 0 \\ 0 & \epsilon_2 \end{pmatrix}, \qquad (8.6)$$

where the normalization $\tilde{g} = g/\kappa$ is applied. Eigenvalues for H can therefore be found from the following determinant,

$$\begin{vmatrix} -\tilde{\omega}_n + i\tilde{g} + \epsilon_1 & 1 \\ 1 & -\tilde{\omega}_n - i\tilde{g} + \epsilon_2 \end{vmatrix} = 0, \qquad (8.7)$$

where $\tilde{\omega}_n = \omega_n/\kappa$. The resulting characteristic equation is given by,

$$\tilde{\omega}_n{}^2 - [\epsilon_1 + \epsilon_2]\tilde{\omega}_n + [\epsilon_1\epsilon_2 - i\tilde{g}(\epsilon_1 - \epsilon_2) + \tilde{g}^2 - 1] = 0. \qquad (8.8)$$

A bias of the system around the EP, i.e. $\tilde{g} = 1$, transforms the characteristic equation to,

$$\widetilde{\omega_n}^2 - [\epsilon_1 + \epsilon_2]\widetilde{\omega_n} + [\epsilon_1\epsilon_2 - i(\epsilon_1 - \epsilon_2)] = 0. \quad (8.9)$$

Without loss of generality, one can assume that the perturbation only affects the gain cavity ($\epsilon_1 = \epsilon,\ \epsilon_2 = 0$). In this respect, the characteristic Eq. (8.9) reduces to,

$$\widetilde{\omega_n}^2 - (\epsilon)\widetilde{\omega_n} - i\epsilon = 0. \quad (8.10)$$

Equation (8.10) can be perturbatively expanded using a Newton-Puiseux series, which begins with a square root element since the EP is of order two. Hence, the first two terms of this series can be written as,

$$\widetilde{\omega_n} \sim c_1\epsilon^{\frac{1}{2}} + c_2\epsilon. \quad (8.11)$$

Inserting the above expansion in Eq. (8.10), one can find the coefficients to satisfy,

$$(c_1^3 - i)\epsilon + (2c_1c_2 - c_1)\epsilon^{3/2} + (c_2^2 - c_2)\epsilon^2 = 0. \quad (8.12)$$

Setting the first two terms in Eq. (8.12) to be zero leads to the following two sets of values for c_1 and c_2,

$$(c_1, c_2) = \left(e^{\frac{i\pi}{4}}, \frac{1}{2}\right), \left(e^{-\frac{i3\pi}{4}}, \frac{1}{2}\right) \quad (8.13)$$

The resulting eigenvalue bifurcations are given by:

$$\widetilde{\omega}_{-1} \sim e^{\frac{i\pi}{4}}\epsilon^{1/2} + \frac{1}{2}\epsilon \quad (8.14)$$

$$\widetilde{\omega}_{1} \sim e^{-\frac{i3\pi}{4}}\epsilon^{1/2} + \frac{1}{2}\epsilon \quad (8.15)$$

Equations (8.14) and (8.15) indicates that for a binary arrangement the real part of the eigenfrequencies bifurcates with a square root dependence on the applied perturbation

($Re\{\Delta\tilde{\omega}^{EP2}\} = \sqrt{2\epsilon}$). By considering the effect of coupling strength, this relation can be written as:

$$Re\{\Delta\omega^{EP2}\} = \sqrt{2\kappa\epsilon}. \qquad (8.16)$$

Figure 35 illustrates the trajectory of change of the eigenfrequencies of a binary PT-symmetric photonic molecule in complex domain when the gain/loss contrast is varied from 0 to 3κ in presence of different amounts of detuning between the rings. Furthermore, the splitting calculated above is plotted in the inset with respect to the induced perturbation, when the system is initially biased at the EP.

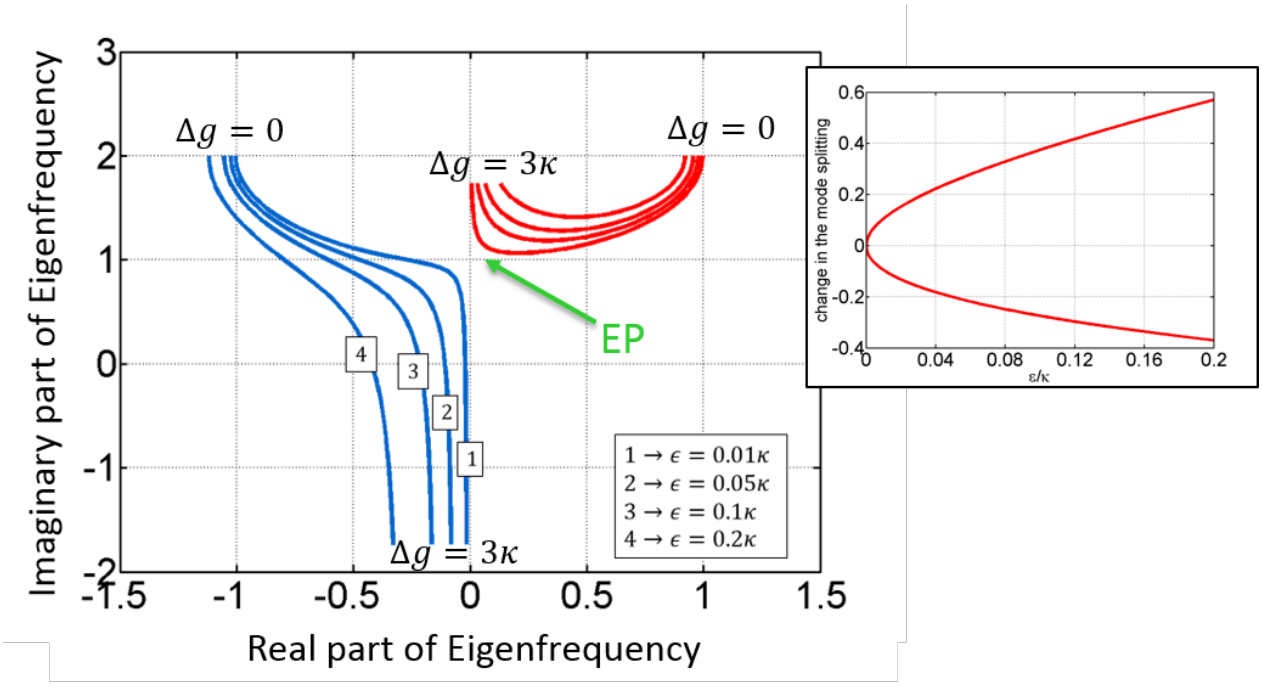

Figure 35. The trajectory of change of the eigenfrequencies in complex domain when the gain/loss contrast is varied from 0 to 3κ in presence of different amounts of detuning between the rings. The splitting between the real parts of the two eigenfrequencies due to the perturbation is considerable around the EP. The inset depicts this splitting with respect to the induced perturbation, when the system is initially biased at the EP.

Figure 36(a) depicts a schematic of the PT-symmetric system comprised of two coupled resonators with gain and loss. Two metallic micro-heaters underneath the structure are used to phase match the cavities as well as introducing thermal perturbations. An SEM image of the rings after etching and microscope images of the fabricated heaters are shown in Fig. 36 (b) and (c), respectively. A detailed description of the fabrication process can be found in chapter 9.

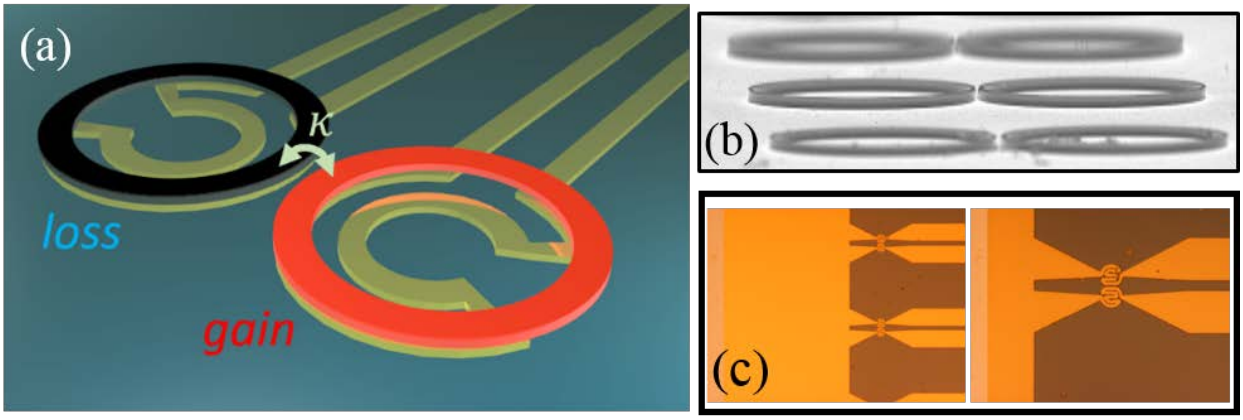

Figure 36. (a) A schematic of the binary PT-symmetric photonic molecule under study. (b) An SEM image of the microrings after etching. (c) Microscope images of the gold micro-heaters with different magnifications.

When the resonators are tuned, the appropriate gain/loss distribution is provided in the structure to bring the system to its EP. At this particular point, all the lasing frequencies coalesce into one line. Once the configuration is set to operate at such state, the gain cavity is then perturbed by supplying current into the corresponding heater. By doing so, the change in the refractive index varies linearly with the electrical power dissipated in the resistor ($\epsilon \propto I^2$). As a result, the lasing frequencies begin to diverge and the ensuing splitting is then monitored with respect to ϵ. The induced differential detuning is experimentally

characterized with respect to the power of the heaters by intentionally decoupling the microrings. This is technique is discussed in detail in section 8.3.

In order to characterize the bifurcation behavior of a EP2 singularity associated with a PT-symmetric coupled-microring structure, we use microring resonators with a radius of $10\,\mu m$, a width of $500\,nm$, and a height of $210\,nm$. The cross-section of the rings is appropriately designed so as to ensure single-mode TE conditions at the wavelength of operation $\lambda_0 \sim 1600\ nm$. The splitting of the lasing frequency is then monitored with respect to heater's current. Figure 37(a) illustrate this relation. Clearly, the wavelength splitting has a square function dependence on the power dissipated in the heater, in accord with theoretical expectations. A log-log plot with a linear slope of $1/2$ reaffirms this behavior (inset in Fig.3 a). The coupling factor in this binary arrangement is $10^{12}\ s^{-1}$. Figure 37(b) depicts the measured enhancement in sensitivity as a function of the induced perturbation (in terms of shift in resonance frequency). In our study, the enhancement is defined in terms of experimentally accessible quantities, as the ratio $\Delta\omega^{EP2}/\epsilon$. Figure 37(b) indicates that as a result of the presence of an exceptional point, the enhancement factor increases for small values of ϵ. In this case, we observed up to 13 times enhancement in the detuning range below 10 GHz.

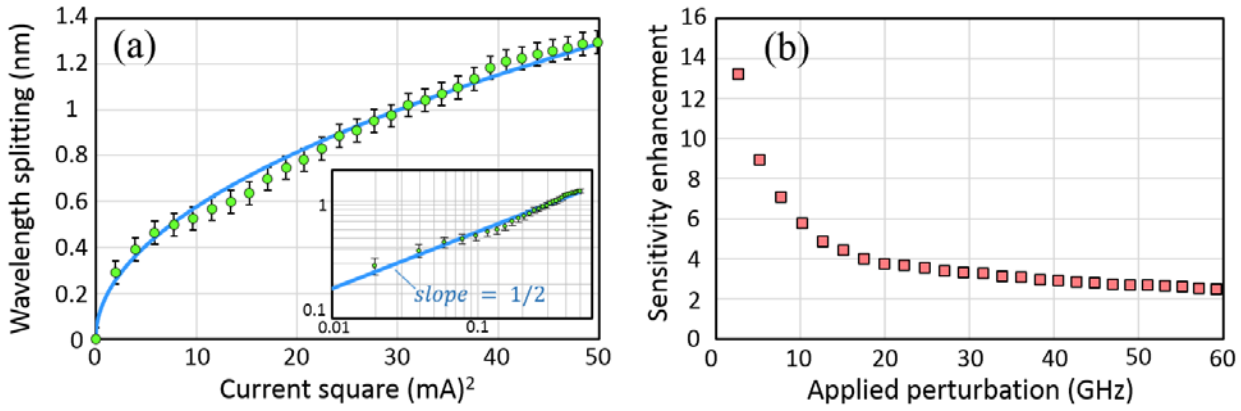

Figure 37. Observed square root wavelength splitting of the lasing modes as a function of power dissipated in the heaters ($\propto I^2$) in a binary PT-symmetric system operating around an exceptional point (EP2). In this case, the perturbation is imposed on the active cavity. The corresponding inset demonstrates a slope of 1/2 in a log-log scale, characteristic of an EP2 singularity. (b) Measured enhancement factor as a function of induced perturbation. An order of magnitude enhancement is obtained for a detuning of ~10 GHz between the two resonators. The enhancement is defined in terms of experimentally accessible quantities, as the ratio $\Delta\omega_n^{EP}/\epsilon$, where in this experiment $\boldsymbol{\epsilon}$ represents the detuning observed in a single isolated cavity for the same heater power.

In order to highlight the role of coupling factor in this approach, we measure the response of systems with different coupling factors to an external perturbation. The results of this measurements are shown in Fig. 38(a). Clearly, increasing the coupling strength between the two resonators leads to improvement in the sensitivity of the structure. Moreover, log-log plots of the data in Fig. 38 (b) show the square root behavior of the system's response to the imposed detuning and the superiority of the sensitivity in the PT-symmetric arrangements over a single cavity.

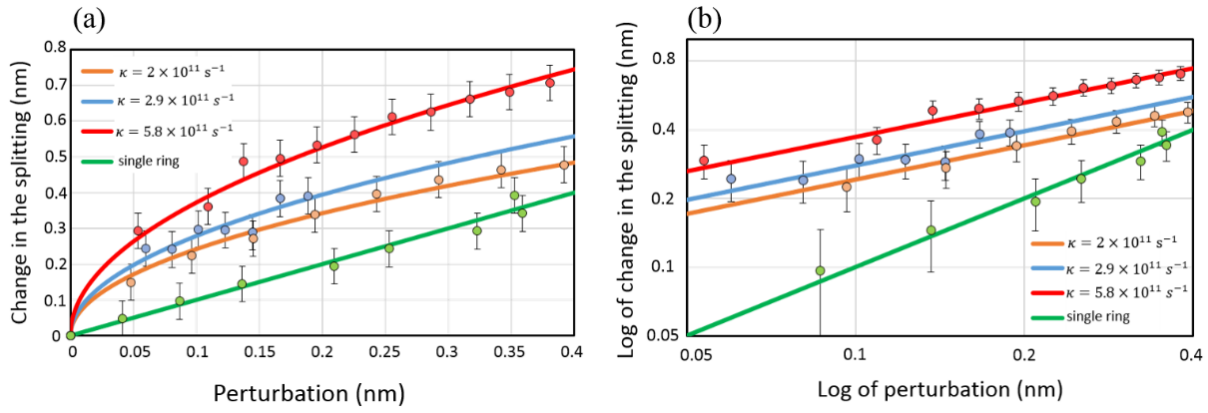

Figure 38. (a) Wavelength splitting with respect to the applied perturbation in PT-symmetric binary arrangement with different coupling factors compared to that of a single resonator. The PT-configurations show superior sensing capability with respect to the single ring. This effect is enhanced by increasing the coupling coefficient (b) The log-log plot of the data in (a) illustrating the square root behavior of the double microring PT-arrangements.

8.2. Ternary systems

In previous section, the bifurcation properties associated with second-order EPs is utilized to enhance the sensitivity of an on-chip micro-resonator arrangement to external perturbations. Interestingly, one can further amplify the effect of perturbations through the use of even higher-order exceptional points (N>2). While a growing number of theoretical studies have been devoted to such higher-order singularities [89]–[91], their experimental demonstration in the optical domain has so far remained elusive. In this section, we report the observation of third-order exceptional points in a ternary parity-time symmetric photonic laser molecule with a judiciously tailored gain-loss distribution. The enhanced response associated with this system follows a cubic root dependence on induced

perturbations. This behavior can be in turn observed by monitoring the lasing emission in the spectral domain.

To realize the third-order EP, we use a PT-symmetric structure that is comprised of three resonators (see Fig. 39(a)). The two resonators on the sides are subject to balanced amounts of gain and loss, while the one in the center happens to be neutral. As a result, the eigenvalues are expected to diverge according to $\epsilon^{1/3}$. In principle, higher order exceptional points can be synthesized in this manner by following a recursive bosonic quantization procedure [92].

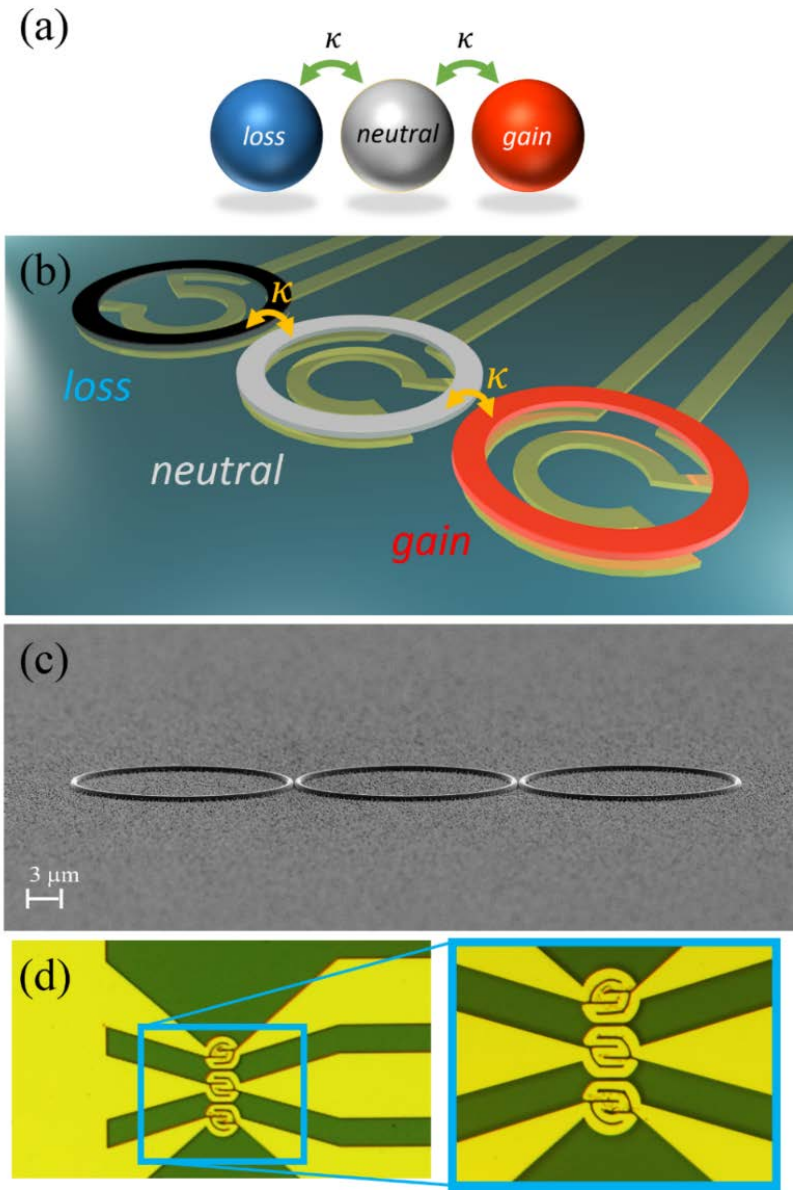

Figure 39. (a) Schematics of a ternary PT-symmetric photonic molecule arrangement (b) A PT-symmetric ternary microring system, with all cavities equidistantly spaced from each other. The two side ring resonators are experiencing a balanced level of gain and loss while the one in the middle is kept neutral. Three micro-heaters are positioned underneath each cavity for fine-tuning the resonance wavelengths and for subsequently introducing thermal perturbations. (c) An SEM image of the structure at an intermediate fabrication step. (d) Microscope images of the heating elements.

Figure 39(b) provides a schematic of the ternary PT-symmetric coupled microring system used in our experiments. The rings are evenly exchanging energy with each other with a coupling strength κ. Three metallic (Au) heaters are positioned underneath each cavity. An SEM image of the structure, at an intermediate stage of fabrication and microscope images of the heaters are shown in Fig. 39(c) and (d), respectively. Using the same approach as in section 7.1, the modal field evolution in this structure obeys $id\vec{V}/dt = H\vec{V}$ in the absence of any disturbance, where $\vec{V} = [a, b, c]^T = V_n e^{-i\omega_n t}$ represents the modal column vector and H is the associated 3×3 non-Hermitian Hamiltonian, i. e.,

$$H = \begin{pmatrix} ig & \kappa & 0 \\ \kappa & 0 & \kappa \\ 0 & \kappa & -ig \end{pmatrix} \qquad (8.17)$$

Here g accounts for the gain/loss levels and κ is the coupling strength between successive resonators. In equation (8.17), a, b, and c represent field amplitudes in the amplifying, neutral, and lossy cavity, respectively. Meanwhile, ϵ denotes an external perturbation, that generally could be introduced anywhere along the diagonal elements of the matrix. Here, without loss of generality, the perturbation has been imposed on the cavity with gain. In this scenario, one can directly determine the complex eigenfrequencies ($\omega_n, n = -1,0,1$) of this trimer by solving the following cubic algebraic equation:

$$\omega_n(\omega_n^2 - 2\kappa^2 + g^2) = 0 \qquad (8.18)$$

which results in the following three eigenvalues,

$$\omega_0 = 0; \omega_{-1,1} = \pm\sqrt{2}\kappa\sqrt{1 - \left(\frac{g}{\sqrt{2}\kappa}\right)^2}. \qquad (8.19)$$

Equation (8.19) indicates that when the gain/loss contrast attains a critical value, in this case $g = \sqrt{2}\kappa$, all three eigenfrequencies coalesce at $\omega_n = 0$, where the system is operating at a third-order exceptional point. Moreover, at this specific point, the three eigenmodes of this ternary photonic molecule fuse at $[a, b, c]^{EP} = A_0[1, -i\sqrt{2}, -1]$, indicating that the energy in the central (neutral) cavity is twice as much of that circulating in the other two resonators which are subjected to gain and loss.

In order to study the eigenvalue bifurcation properties, it is convenient to work with a normalized description according to $\tilde{g} = g/\kappa$, in which case the perturbed Hamiltonian H can be written as,

$$H = \kappa \begin{pmatrix} i\tilde{g} & 1 & 0 \\ 1 & 0 & 1 \\ 0 & 1 & -i\tilde{g} \end{pmatrix} + \kappa \begin{pmatrix} \epsilon_1 & 0 & 0 \\ 0 & \epsilon_2 & 0 \\ 0 & 0 & \epsilon_3 \end{pmatrix} \qquad (8.20)$$

For this particular form of the Hamiltonian the perturbation is assumed to not affect the coupling. Hence the perturbation manifests itself as three separate terms along the diagonal, i.e. ϵ_1, ϵ_2 and ϵ_3 corresponding to the gain, neutral and lossy cavities respectively. The determinant of H is given by,

$$\begin{vmatrix} -\tilde{\omega}_n + i\tilde{g} + \epsilon_1 & 1 & 0 \\ 1 & -\tilde{\omega}_n + \epsilon_2 & 1 \\ 0 & 1 & -\tilde{\omega}_n - i\tilde{g} + \epsilon_3 \end{vmatrix} = 0, \qquad (8.21)$$

where $\tilde{\omega}_n = \omega_n/\kappa$. For a system biased around the exceptional point, i.e. $\tilde{g} = \sqrt{2}$, the characteristic equation of Eq. (8.21), becomes,

$$\tilde{\omega}_n{}^3 - (\epsilon_1 + \epsilon_2 + \epsilon_3)\tilde{\omega}_n{}^2 + \left(\epsilon_1\epsilon_2 + \epsilon_2\epsilon_3 + \epsilon_3\epsilon_1 - i\sqrt{2}(\epsilon_1 - \epsilon_3)\right)\tilde{\omega}_n +$$

$$\left(\epsilon_1 + \epsilon_3 - \epsilon_1\epsilon_2\epsilon_3 - 2\epsilon_2 + i\sqrt{2}\epsilon_2(\epsilon_1 - \epsilon_3)\right) = 0. \qquad (8.22)$$

Since $\epsilon_{1,2,3} \ll 1$, higher order terms can be ignored and Eq. (8.22) simplifies to:

$$\widetilde{\omega_n}^3 - (\epsilon_1 + \epsilon_2 + \epsilon_3)\widetilde{\omega_n}^2 + \left(-i\sqrt{2}(\epsilon_1 - \epsilon_3)\right)\widetilde{\omega}_n + (\epsilon_1 + \epsilon_3 - 2\epsilon_2) = 0. \qquad (8.23)$$

Three different cases are investigated; (i) The perturbation is on the gain-element; (ii) On the neutral element; (iii) Both on the gain and neutral elements with a proportionality between them. The latter scenario is closest to the actual experiment. Although the perturbation is introduced by a heater located underneath the gain cavity, the generated heat perturbs the neutral cavity as well due to thermal diffusion.

(i) Perturbing the gain cavity

In this case $\epsilon_1 = \epsilon,\ \epsilon_2 = \epsilon_3 = 0$. Hence Eq. (8.23) reduces to:

$$\widetilde{\omega_n}^3 - (\epsilon)\widetilde{\omega_n}^2 + \left(-i\sqrt{2}\epsilon\right)\widetilde{\omega}_n + \epsilon = 0. \qquad (8.24)$$

Equation (8.24) can be perturbatively expanded using a Newton-Puiseux series. Considering the first two terms only, A $\widetilde{\omega}_n \sim c_1\epsilon^{\frac{1}{3}} + c_2\epsilon^{\frac{2}{3}}$, with the coefficients c_1 and c_2 being complex constants, results in

$$(c_1^3 + 1)\epsilon + \left(3c_1^2c_2 - i\sqrt{2}c_1\right)\epsilon^{4/3} + \left(3c_1c_2^2 - c_1^2 - i\sqrt{2}c_2\right)\epsilon^{5/3} + (c_2^3 - 2c_1c_2)\epsilon^{6/3} + (-c_2^2)\epsilon^{7/3} = 0. \qquad (8.25)$$

Forcing the coefficients of the first two terms to be zero, we obtain three sets of values for the coefficients c_1 and c_2, corresponding to the three eigenvalues

$$(c_1, c_2) = \left(e^{-\frac{i\pi}{3}}, \frac{i\sqrt{2}}{3}e^{\frac{i\pi}{3}}\right), \left(e^{\frac{i\pi}{3}}, \frac{i\sqrt{2}}{3}e^{-\frac{i\pi}{3}}\right), \left(-1, -\frac{i\sqrt{2}}{3}\right). \qquad (8.26)$$

The bifurcations in the eigenvalues now acquire the form:

$$\begin{cases} \widetilde{\omega}_{-1} \sim e^{\frac{i\pi}{3}}\epsilon^{1/3} + \frac{i\sqrt{2}}{3}e^{-\frac{i\pi}{3}}\epsilon^{\frac{2}{3}} \\ \widetilde{\omega}_{0} \sim e^{-\frac{i\pi}{3}}\epsilon^{1/3} + \frac{i\sqrt{2}}{3}e^{\frac{i\pi}{3}}\epsilon^{\frac{2}{3}} \\ \widetilde{\omega}_{1} \sim -\epsilon^{\frac{1}{3}} - \frac{i\sqrt{2}}{3}\epsilon^{\frac{2}{3}} \end{cases} \quad (8.27)$$

As Eq. (8.27) indicates, the frequency splitting between $\widetilde{\omega}_0, \widetilde{\omega}_1$, as well as $\widetilde{\omega}_{-1}, \widetilde{\omega}_1$ follow the cubic root of ϵ, while the difference between real parts of $\widetilde{\omega}_0, \widetilde{\omega}_1$is on the order of $\epsilon^{2/3}$. This behavior can experimentally be characterized in the spectral domain by monitoring the resonant wavelength splitting of for example $\widetilde{\omega}_0, \widetilde{\omega}_1$. This splitting can be written as

$$Re\{\Delta\widetilde{\omega}^{EP3}\} \sim \frac{3}{2}\epsilon^{\frac{1}{3}} \quad (8.28)$$

(ii) Perturbing the neutral cavity

For a perturbation of the neutral cavity $\epsilon_2 = \epsilon,\ \epsilon_1 = \epsilon_3 = 0$. As a result, the characteristic equation, Eq. (8.23) can be written as

$$\widetilde{\omega}_n{}^3 - (\epsilon)\widetilde{\omega}_n{}^2 - 2\epsilon = 0. \quad (8.29)$$

Again assuming a Newton-Puiseux perturbative expansion as applied in the last section for $\widetilde{\omega}_n$, one obtains from Eq. (8.29),

$$(c_1^3 - 2)\epsilon + (3c_1^2c_2)\epsilon^{4/3} + (3c_1c_2^2 - c_1^2)\epsilon^{5/3} + (c_2^3 - 2c_1c_2)\epsilon^{6/3} + (-c_2^2)\epsilon^{7/3} = 0 \quad (8.30)$$

The three sets of values for the coefficients c_1 and c_2 are as follows:

$$(c_1, c_2) = \left(2^{\frac{1}{3}}e^{-\frac{i2\pi}{3}}, 0\right), \left(2^{\frac{1}{3}}, 0\right), \left(2^{\frac{1}{3}}e^{\frac{i2\pi}{3}}, 0\right). \quad (8.31)$$

The resulting bifurcations in the eigenvalues acquire the form:

$$\begin{cases} \widetilde{\omega}_{-1} \sim 2^{\frac{1}{3}} e^{-\frac{i2\pi}{3}} \epsilon^{1/3} \\ \widetilde{\omega}_{0} \sim 2^{\frac{1}{3}} \epsilon^{\frac{1}{3}} \\ \widetilde{\omega}_{1} \sim 2^{\frac{1}{3}} e^{\frac{i2\pi}{3}} \epsilon^{\frac{1}{3}} \end{cases} \quad (8.32)$$

(iii) Perturbing both the gain and neutral cavities

In this case, the applied perturbations acquire the values $\epsilon_1 = \epsilon,\ \epsilon_2 = \alpha\epsilon, (\alpha < 1),\ \epsilon_3 = 0.$ Therefore, the characteristic equation, according to Eq. (8.23), is given by,

$$\widetilde{\omega}_n{}^3 - \epsilon(1+2\alpha)\widetilde{\omega}_n{}^2 + \left(-i\sqrt{2}\epsilon\right)\widetilde{\omega}_n + \epsilon(1-2\alpha) = 0. \quad (8.33)$$

After expanding the eigenvalues by $\widetilde{\omega}_n \sim c_1\epsilon^{\frac{1}{3}} + c_2\epsilon^{\frac{2}{3}}$, one can obtain,

$$[c_1^3 + 1 - 2\alpha]\epsilon + \left[3c_1^2c_2 - i\sqrt{2}c_1\right]\epsilon^{4/3} + \left[3c_1c_2^2 - c_1^2(1+2\alpha) - i\sqrt{2}c_2\right]\epsilon^{5/3} +$$

$$[c_2^3 - 2c_1c_2(1+2\alpha)]\epsilon^{6/3} + [-c_2^2(1+2\alpha)]\epsilon^{7/3} = 0. \quad (8.34)$$

By forcing the coefficients of the first two terms to be zero, one can find c_1 and c_2 to be:

$$(c_1, c_2) = \left((1-2\alpha)^{\frac{1}{3}} e^{-\frac{i\pi}{3}}, \frac{i\sqrt{2}}{3}(1-2\alpha)^{-\frac{1}{3}} e^{\frac{i\pi}{3}}\right), \left((1-2\alpha)^{\frac{1}{3}} e^{\frac{i\pi}{3}}, \frac{i\sqrt{2}}{3}(1-2\alpha)^{-\frac{1}{3}} e^{-\frac{i\pi}{3}}\right), \left(-(1-2\alpha)^{\frac{1}{3}}, -\frac{i\sqrt{2}}{3}(1-2\alpha)^{-\frac{1}{3}}\right). \quad (8.35)$$

The bifurcations in the eigenvalues now acquire the form:

$$\begin{cases} \widetilde{\omega}_{-1} \sim (1-2\alpha)^{\frac{1}{3}} e^{\frac{i\pi}{3}} \epsilon^{1/3} + \frac{i\sqrt{2}}{3}(1-2\alpha)^{-\frac{1}{3}} e^{-\frac{i\pi}{3}} \epsilon^{\frac{2}{3}} \\ \widetilde{\omega}_{0} \sim (1-2\alpha)^{\frac{1}{3}} e^{-\frac{i\pi}{3}} \epsilon^{1/3} + \frac{i\sqrt{2}}{3}(1-2\alpha)^{-\frac{1}{3}} e^{\frac{i\pi}{3}} \epsilon^{\frac{2}{3}} \\ \widetilde{\omega}_{0} \sim (1-2\alpha)^{\frac{1}{3}} e^{-\frac{i\pi}{3}} \epsilon^{1/3} + \frac{i\sqrt{2}}{3}(1-2\alpha)^{-\frac{1}{3}} e^{\frac{i\pi}{3}} \epsilon^{\frac{2}{3}} \end{cases} \quad (8.36)$$

The similarity of Eq. (8.36) to Eq. (8.27) demonstrates that this scenario is identical to case (i), where the perturbation exclusively affects the gain cavity, except for the $(1-2\alpha)^{1/3}$ coefficients. Therefore, the bifurcation characteristics of the system analyzed in case (i) are

extended to this case. For example, the frequency splitting between $\widetilde{\omega}_0, \widetilde{\omega}_1$, follows the cubic root of the imposed perturbation and can be written as:

$$Re\{\Delta\widetilde{\omega}^{EP3}\} \sim \frac{3}{2}(1-2\alpha)^{\frac{1}{3}}\epsilon^{\frac{1}{3}}. \qquad (8.37)$$

Equation (8.37) indicates that the presence of ϵ_2 reduces the sensitivity of the system is by a factor of $\sqrt[3]{|2\alpha-1|}$. Therefore, the sensitivity can be improved when the outer cavities are isolated from the introduced perturbation. Although, in our experiment, the heater associated with the gain resonator is used to impose the perturbations, as a result of thermal diffusion, both gain and neutral resonators were differentially detuned (case (iii)). However, due to the analogy of Eqs. (8.36) and (8.27), our experiment can be accurately modeled using the analysis of case (i).

To better illustrate how a small detuning or gain variation may affect this arrangement, we assume $\epsilon_1 \neq 0, \epsilon_2 = \epsilon_3 = 0$. In this aspect, the three complex eigenfrequencies of this PT-symmetric configuration can be numerically obtained by solving the characteristic equation (8.24), as depicted in Figures 40(a) and (b). Of particular interest is how this system reacts around the EP3 singularity, when $g = \sqrt{2}\kappa$. This response is highlighted in the two cross sections (in both the real and imaginary domain) in Figs. 40(a) and (b) as well as in Figs. 40(c) and (d) (solid curves). The differential between two eigenfrequencies (in this case ω_0 and ω_1) is also plotted in Fig. 40(e) (solid curve) as a function of ϵ. By considering the logarithmic behavior of this latter curve (solid line in Fig. 40(f)), one finds that the slope of the response is 1/3, thus numerically confirming that indeed perturbations around EP3 experience an enhancement of the type $\epsilon^{1/3}$.

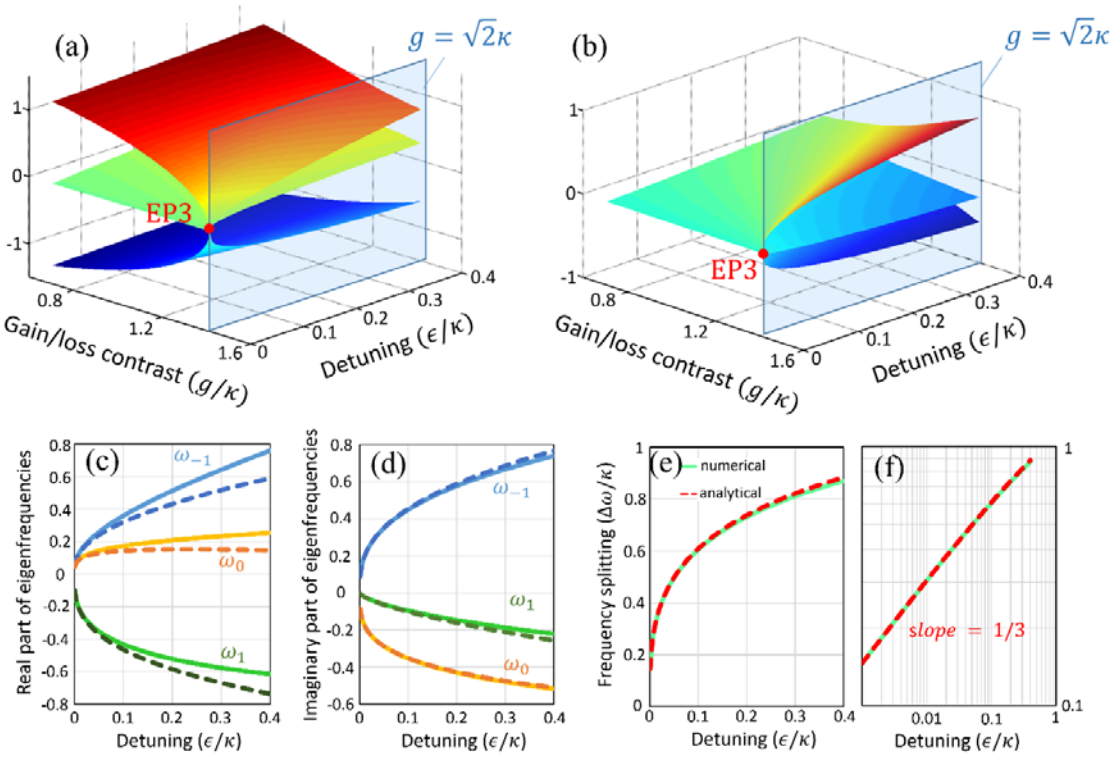

Figure 40. (a) The real parts of the three eigen-frequencies of the ternary PT-symmetric system as a function of the gain/loss contrast and detuning. The exceptional point is located at $g = \sqrt{2}\kappa$ and $\epsilon_1 = 0$. (b) Same as in (a) for the imaginary parts of the eigen-frequencies. (c) Analytical results (dashed lines) and numeral solutions (solid lines) for the real parts of the eigen-frequencies as the applied detuning varies when $g = \sqrt{2}\kappa$. (d) Same as in (c) for the imaginary part of the eigen-frequencies. (e) Analytical (dashed red line) and numerical (solid green line) results depicting the difference between ω_0 and ω_1 in the real domain, illustrating a cubic-root behavior. (f) Same result as in (e) only now shown in a log-log scale. A slope of 1/3 confirms the cubic-root response with respect to detuning.

Now one can compare the analytical results to the exact numerical solution. From Eq. (8.27), one finds that $\omega_n = e^{-i(2n+1)\pi/3}\kappa^{2/3}\epsilon^{1/3} + i\sqrt{2}e^{i(2n+1)\pi/3}\kappa^{1/3}\epsilon^{2/3}/3$. Based on this latter expression, the system response is plotted in Figs. 40(c)-(f) (dashed curves), in close agreement to that obtained numerically. Our analysis indicates that the real parts of the pair ω_{-1}, ω_1 as well as those of ω_0, ω_1 diverge from each other in an $\epsilon^{1/3}$ fashion, while the

differential between ω_0, ω_{-1} (that happened to be originally degenerate) varies instead according to $\epsilon^{2/3}$. Hence, in characterizing the sensitivity response of this ternary laser arrangement we will monitor the separation of the ω_0, ω_1 spectral lines. In this case, by involving the coupling coefficient, the anticipated frequency splitting in Eq. (8.28) can be rewritten as:

$$\Delta\omega^{EP3} = \frac{3}{2}\,\kappa^{2/3}\,\sqrt[3]{\epsilon}. \qquad (8.38)$$

Here, the microring resonators and the experimental setting are the same as those used in the previous section. The ternary structure in this experiment is comprised of three equidistantly spaced microrings, having a coupling strength of $\sim 7 \times 10^{11}\ s^{-1}$. To establish PT-symmetry in the system, the pump beam is completely withheld from one of the side rings. In addition, the central ring (neutral region) is partially illuminated while the third ring is fully pumped. By adjusting the transverse position of the knife edge and the pump level, the three lasing modes of this structure gradually coalesce into one line (1602 nm), associated with the emergence of the third order exceptional point. The intensity profile (Fig. 41(a)) of the lasing mode at this point is captured via a CCD camera and is in qualitative agreement with that expected from theory. Once the system is set on an EP3, the heater underneath the pumped cavity is activated. As a consequence of this perturbation, the single lasing mode splits into three distinct branches as anticipated from Fig. 40(c). The spectral evolution of this transition is collected using a spectrometer with an array detector (Fig. 41(b)). As previously indicated, in this experiment we monitor the difference between the resonance frequencies ω_0, ω_1. Figure 41(c) indicates that indeed the frequency separation

$\Delta\omega^{EP3}$ follows a cubic root function with respect to ϵ_1. This is also confirmed after plotting these data in a log-log scale from where one can directly infer a slope of 1/3 (see the inset of Fig. 41(c)). The enhancement factor corresponding to this trimer is plotted in Fig. 41(d). In this case, the sensitivity is magnified ~23 times when the detuning between the active and neutral resonators is below 5 GHz. In the next section we show that this response can be further boosted by a factor of 2 if the perturbation is exclusively acting on one of the cavities.

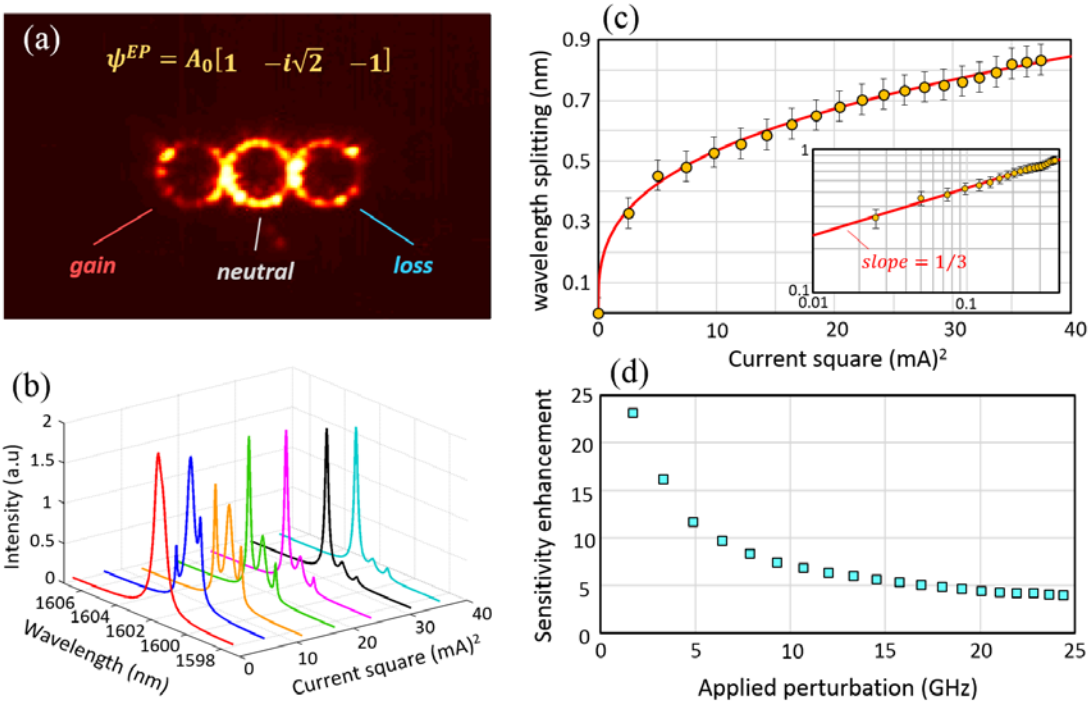

Figure 41. (a) Image of the intensity profile of the lasing mode in a PT-symmetric ternary laser arrangement operating around the exceptional point (EP3). The energy in the central (neutral) cavity is approximately twice that in the side resonators. (b) Spectra of the three lasing modes as the system departs from the exceptional point due to an imposed perturbation on the gain cavity. (c) Resulting cubic-root splitting between two neighboring lasing wavelengths as a function of I^2. Inset: a log-log curve indicates a slope of 1/3. (d) Observed sensitivity enhancement in this arrangement when biased at an EP3 point. An enhancement as large as ~23 is now measured when the detuning is below 10 GHz.

8.3. Characterization of the thermally applied perturbations

This section provides the experimental characterization of the induced perturbations by one activated micro-heater in the coupled resonator system. Due to the thermal diffusion, power dissipated in the heater ($P = RI^2$) linearly affects the refractive index of all cavities with different proportionality constants. Therefore, by intentionally decoupling the involved microrings, the applied detuning in the resonance wavelength ($\Delta\lambda$) of the cavities can be measured as a function I^2 (Fig. 42).

In the binary configuration (Fig 42(a)), the effective imposed perturbation is the difference between the shifts in the resonance wavelengths of the two cavities $\epsilon = \Delta\lambda_1 - \Delta\lambda_2$, which is measured to be $\epsilon \cong 0.01I^2$. In this case, the sensitivity enhancement that is shown in Fig. 37(b) is defined as $\Delta\lambda^{EP2}/\epsilon$. Note that the relationship between the imposed detuning and the power of the heater is a function of various parameters in the system such as ohmic resistance and vertical distance of the heaters from the rings, hence it can acquire distinct values for different structures.

On the other hand, in the ternary system (Fig. 41), effectively two different perturbations are present. The first one is detuning the closest resonator to the active heater by $\epsilon_1 = \Delta\lambda_1 - \Delta\lambda_3$, and the second is perturbing the central microring with respect to $\epsilon_2 = \Delta\lambda_2 - \Delta\lambda_3$. These two values were measured to be $\epsilon_1 = 0.012I^2$, and $\epsilon_2 = 0.007I^2$. Following the calculations in the previous section, one can write $\epsilon_2 = \alpha\epsilon_1$, where α is measured to be 0.6. As discussed above, the presence of ϵ_2 in the system decreases the sensitivity by $\sqrt[3]{|2\alpha - 1|}$, which translates to a two-times reduction in the ensuing wavelength splitting and

consequently the enhancement factor. For this ternary system, the sensitivity enhancement shown in Fig. 41(d) is defined as $\Delta\lambda^{EP3}/(\epsilon_1 - \epsilon_2)$.

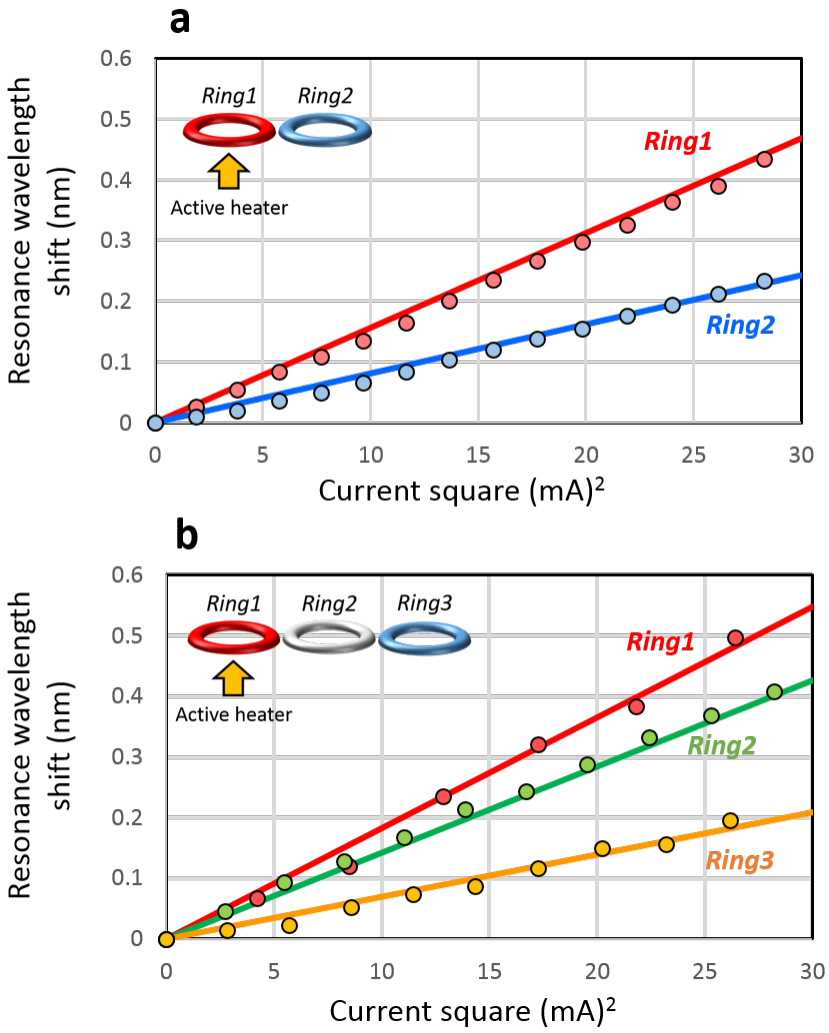

Figure 42. The change in resonance wavelengths ($\Delta\lambda$) of the intentionally decoupled cavities as a function of I^2 (heater power) in (a) a binary structure and (b) a ternary structure. The applied perturbation varies linearly with the power of the heater, and is imposed differentially on the microrings with respect to their distance from the active heater. The different colors of the rings are used for distinction and not for representation of gain/loss.

CHAPTER 9: EXPERIMNTAL SETTING

In this chapter, details of techniques regarding the sample fabrication process and measurement setup are provided.

9.1. Sample fabrication

Figure 43(a) shows the general fabrication steps to realize the coupled microring structures used in this study. The quantum well gain material forming the microrings is comprised of six $In_{x=0.734}Ga_{1-x}As_{y=0.57}P_{1-y}$ wells (thickness: 10 nm) which are sandwiched by cladding layers of $In_{x=0.56}Ga_{1-x}As_{y=0.938}P_{1-y}$ (thickness: 20 nm) grown on p-type InP substrate. A 10 nm thick InP protective layer covers the quantum wells. The MOCVD epitaxially-grown wafer was supplied by OEpic Inc.

To fabricate the micoring resonators, hydrogen silsesquioxane (HSQ) solution in methyl isobutyl ketone (MIBK) was first spin-coated on the wafer as a negative tone electron beam resist. Consequentially Ebeam lithography was used to write the ring resonator patterns. These patterns were developed by tetramethylammonium hydroxide (TMAH) and subsequently transferred to the wafer through reactive ion etching process. The dry etching involves H2:CH_4:Ar gases with flow rate of 40:4:20 SCCM, RIE power of 150 W, and chamber pressure of 30 mT. A scanning electron beam (SEM) image of the sample at the end of this step is shown in Figs. 10(b), 18(c), 28(b), and 39(c). Next, a 500 nm silicon dioxide (SiO_2) layer was deposited on the structure using plasma enhanced chemical vapor deposition (PECVD) to promote the adhesion of bisbenzocyclobutene (BCB). Next, a 3 μm thick layer of

BCB was spin-coated and cured on the sample for planarization. The heaters' pattern was then aligned on the top of the rings and projected onto NR71000PY negative resist via photolithography. The pattern was developed in RD6 for 7 sec. Next, we deposited 10 nm of Titanium (for adhesion) and 150 nm of gold using thermal evaporation. The sample was then immersed in RR41 resist remover heated up to 100° C to lift off the remaining photoresist. A microscope image of the sample at this step provided in Fig. 36(c) and 39(d) showing the gold heaters fabricated at ~3 μm on top of the rings. This distance is chosen in order to eliminate the optical interaction between the cavity and the metallic section. Next, the sample was wire bonded to a 16-pin carrier (TO8 header) in order to provide access to the heaters during the experiment (Fig. 43(b)). The sample was then covered with SU8 photoresist for protection and mechanical support. Finally, the InP substrate was removed by a wet etching process employing hydrochloric acid (HCl). The wet etching is highly selective and hence only removed InP and not the InGaAsP layers. This leaves the microrings partially embedded in the SiO2 and exposed to air. After this process, the structure is accessible for the measurement from the backside through a gap in the header (Fig. 43(c)). Note that, there is no micro-heater structure in the experiments of chapters 3 to 7. Therefore, for these samples, removing the InP substrate (steps 9 and 10) is performed right after SiO_2 deposition (step 4), while the rest of the process is similar to that of depicted in Fig. 43(a).

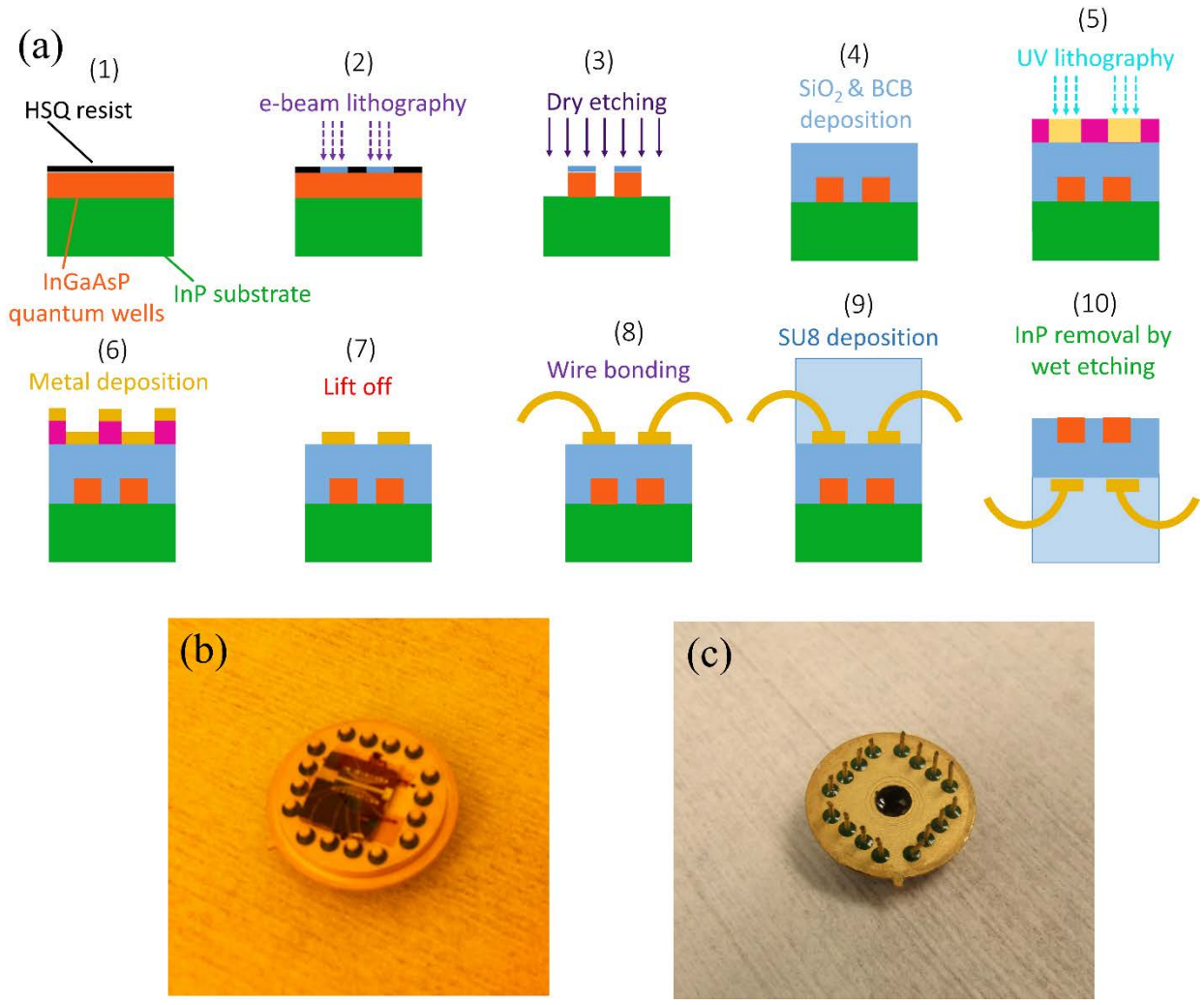

Figure 43. (a) Schematic of the sample fabrication process. (b) The heaters are electrically connected to the header's pins via wire bonding. (c) The microring arrangements are accessible for the measurement after removing the InP substrate from the backside through a gap in the header.

9.2. Characterization setup

The microring arrangements were optically pumped with a pulsed 1064 nm laser beam (SPI fiber laser). A schematic of the measurement setup is depicted in Fig. 44. The diameter of the beam was arranged such that at the surface of the sample it had a diameter of ~100 μm. A microscope objective with a numerical aperture of 0.42 was used to project the pump beam

on the rings, as well as to collect the output light from the samples. Alignment of the pump beam to the desired cavity was performed by imaging the sample surface through two cascaded 4-f imaging systems onto an IR CCD camera (Xenics Inc.), using a broadband IR light source. Output spectra were obtained using a spectrometer. For the characterization of single mode lasing in chapters 3 to 7, we utilized a Princeton Instruments Acton SP2300 spectrometer with a 600 g/mm grating and an LN2 cooled InGaAs detector (Roper Scientific OMA-V). The entrance slit size is set to 500 μm, and the spectra were recorded with a resolution of 0.4 nm. Since higher resolution was required to characterize the sensitivity of the arrangements, for the experiments in chapter 8, a Hiroba Scientific iHR320 equipped with a 900 g/mm grating was used in conjunction with an electrically cooled InGaAs detector (Synapse EM). Here, the spectrometer entrance slit was set to 100 μm in order to obtain the resolution of ~0.13 nm.

In order to establish the PT-symmetry in the structures, the microrings were pumped selectively by using a transversely movable knife edge imaged on the surface of the sample. By adjusting the intensity of the pump beam and position of the knife edge, the required gain/loss distribution was realized. Figure 45 shows the intensity profile of the pump beam at the place of the sample with and without the knife edge's image. The current to the heaters were supplied by precision current sources (ILX Lightwave) to ensure stability of the induced thermal perturbations. Figures 46 (a) and (b) respectively depict three heaters imaged on the measurement station using a broadband NIR source and the associated ring resonators when they are all evenly pumped.

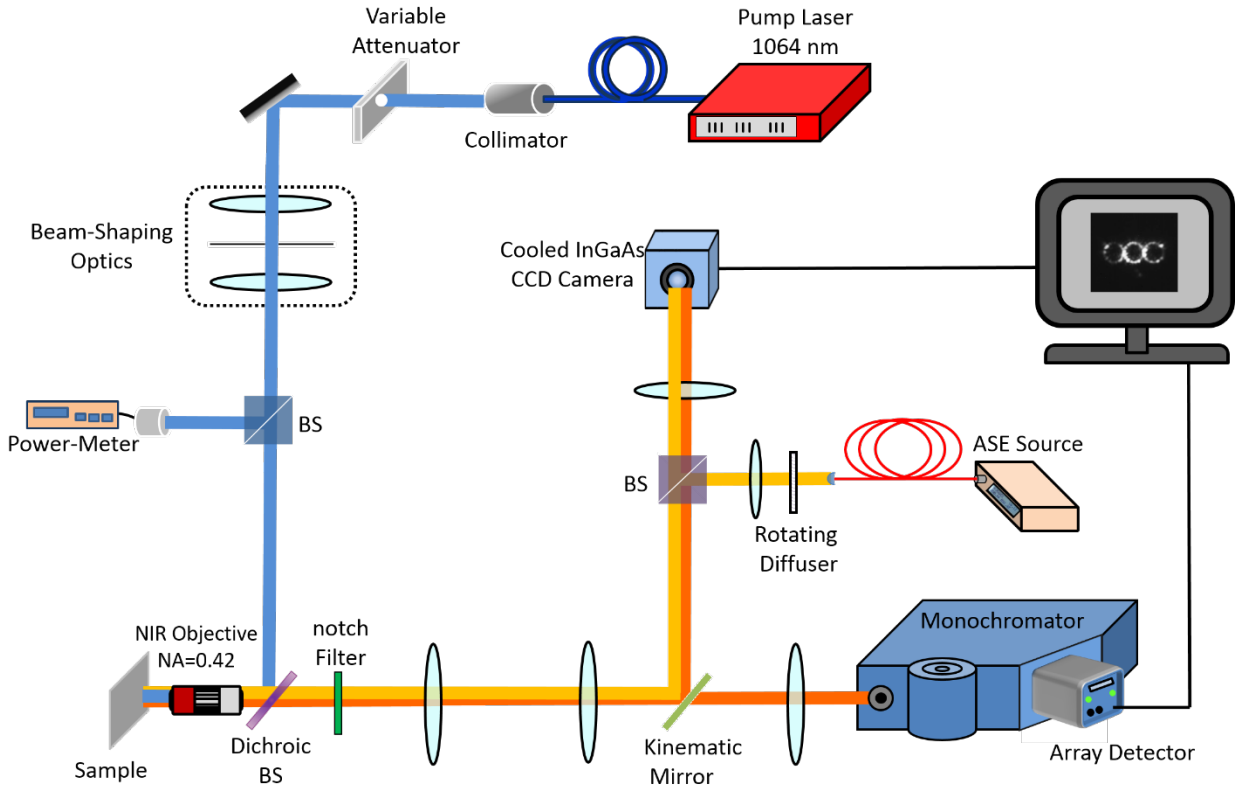

Figure 44. A schematic of the experimental setup

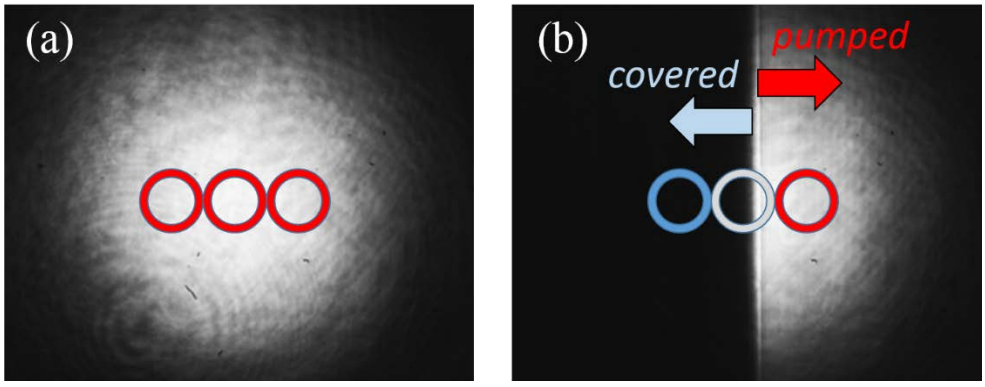

Figure 45. (a) The intensity profile of the pump beam at the place of the sample (a) without and (b) with the knife edge's image. By adjusting the intensity of the pump beam and position of the knife edge, the designed gain/loss distribution is realized.

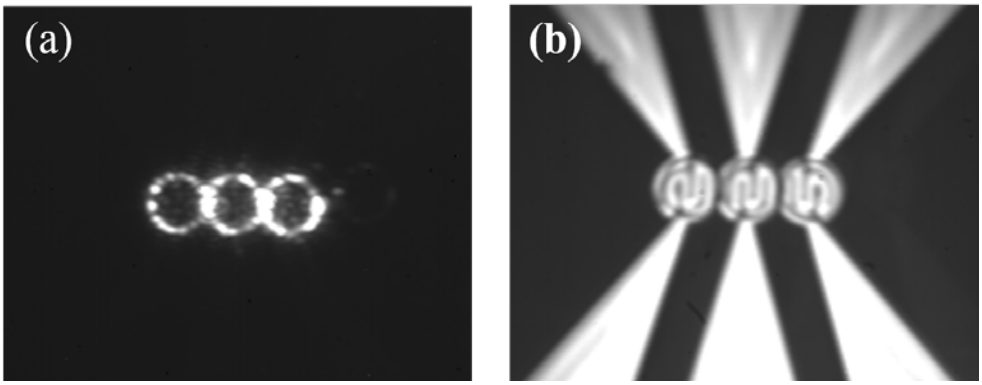

Figure 46. (a) Three coupled microring resonators when they are all evenly pumped and (b) the associated heaters imaged on the measurement station using a broadband NIR source.

CHAPTER 10: CONCLUSION

In this work, we successfully utilized the peculiar properties of exceptional points to address some of the longstanding challenges in integrated photonics. These non-Hermitian degeneracies were realized in active semiconductor coupled micro-cavity systems with judiciously tailored gain and loss.

On-chip PT-symmetric microring lasers were implemented on an InP-based gain medium by pairing an amplifying microring to an identical but lossy counterpart. In addition, the behavior of the system was characterized when operating around their associated exceptional point. Single mode lasing was then enforced in this arrangement via selective breaking of PT-symmetry. This mode management scheme was utilized to suppress unwanted lasing modes in both temporal and spatial domains. In this regard, it was shown that the maximum available gain for single mode operation can be systematically boosted in PT-symmetric lasers. The proposed method is robust, broadband, and self-adaptive, and can in general be implemented using any type of laser cavity. These results can have widespread ramifications in both fields of semiconductor lasers and non-Hermitian optics.

Dark state laser is another resonant configuration that can support EPs due to its unique geometrical design. This open system is comprised of two dissimilar microrings coupled via a central channel. By appropriately using the dynamics of the system near EP, we demonstrated single mode lasing at pump powers way above threshold and also one FSR of frequency tuning.

Furthermore, we showed that binary and ternary PT-symmetric coupled resonator systems are ultra-sensitive to perturbations when biased at the exceptional point. In particular, we reported the first observation of higher-order exceptional points in a ternary parity-time symmetric photonic laser molecule. The enhanced response associated with this system follows a cubic root dependence on externally introduced perturbations, and can be detected in the spectral domain. This approach is easy to implement and can in principle be adopted in various other photonic configurations. This work can pave the way for utilizing exceptional points for enhancing sensitivity of optical micro-cavity arrangements to small perturbations.

APPENDIX: LASER LINEWIDTH MEASUREMENT

The spectral linewidth of a semiconductor laser has a complex dependence on many different parameters of the system, such as Q-factor of the cavity, output power, mode overlap with the gain region, and nonlinearities in a lasing cavity. Since the linewidth of the lasers in this study was too narrow for the spectrometer to resolve, a new method was employed to measure this important laser characteristic. Here, we utilized a rotating high finesse parallel-plane Fabry-Perot (FP) in the path of the laser emission to perform a high resolution spectral measurement. The FSR and linewidth of the Fabry-Perot is 60 and 2 GHz, respectively. Therefore, the incoming laser beam should be temporally single mode and narrower than 60 GHz.

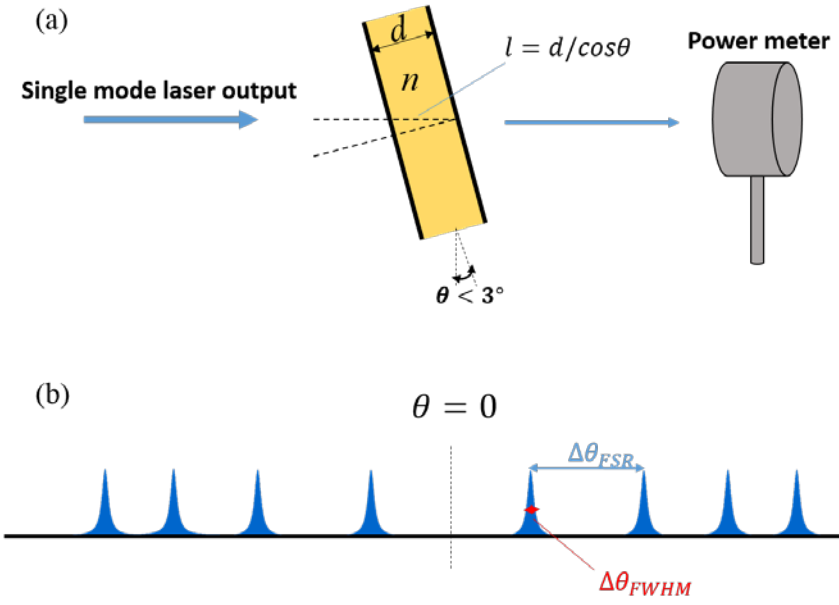

Figure 47. (a) A schematic of experimental setting for high resolution linewidth measurement involving a rotating Fabry-Perot and a power meter. (b) A schematic of the measured power with respect to tilt angle of the FP for single longitudinal mode input

Figure 47(a) shows a schematic of this measurement. By tilting the FP around 3° from the normal incident condition, we can monitor the amount of the optical power throughout the frequency domain. Figure 47(b) schematically depicts the result of such a measurement, when the input is a single lasing mode. As this figure indicates, it is desirable to carry out the experiment when the incoming beam is very close to normal incident conditions, since for larger tilt angles, finer rotation steps are required to achieve the same spectral resolution. To map the measured powers from the tilt angle axis to the frequency axis, one can use the known value for the FSR of the FP.

For incoming light that satisfies the resonance condition of the FP, one can write,

$$2 \times \frac{2\pi f}{c} \times \frac{nd}{\cos(\theta)} = 2m\pi \qquad (A.1)$$

where, f is the frequency of the laser light, θ is the associated tilt angle of the FP, d and n are the width and refractive index of the FP, respectively, c is the speed of light in the vacuum, and m is the number of the resonance mode. From (A.1), one can simply calculate the frequency with respect to the θ to be,

$$f = \frac{mc}{2nd} \times \cos(\theta). \qquad (A.2)$$

Subsequently,

$$f_1 - f_2 = \frac{mc}{2nd} \times (\cos(\theta_1) - \cos(\theta_2)). \qquad (A.3)$$

So for any two arbitrary angles, Eq. (A.3) can be written as,

$$\delta f = C \times (\cos(\theta_1) - \cos(\theta_2)) \qquad (A.4)$$

where, δf is the frequency and $C = 2m\pi/2nd$ is a property of the FP, which should be found experimentally.

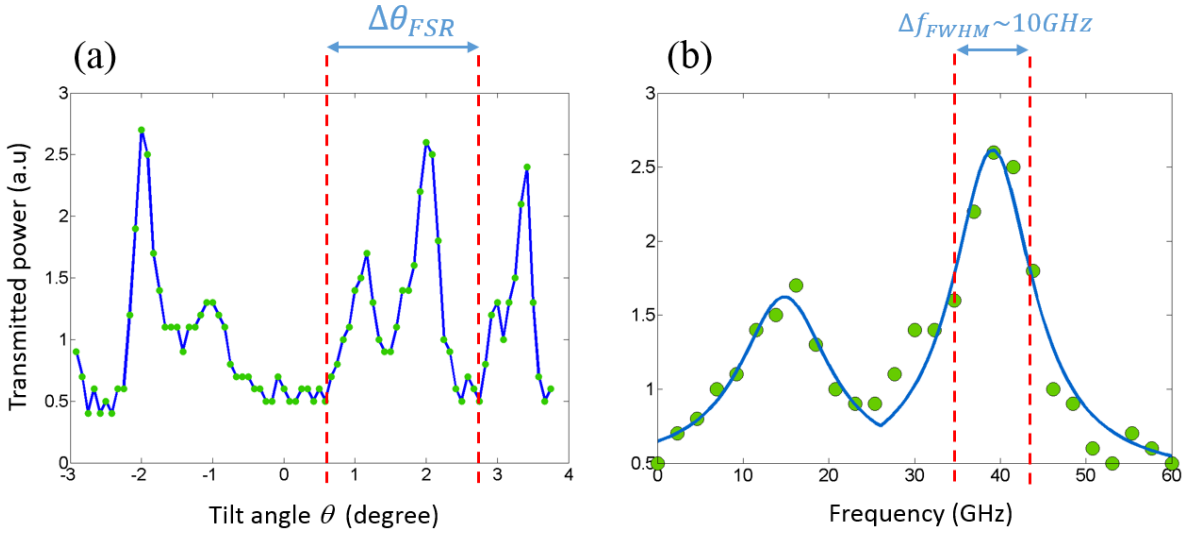

Figure 48. (a) The measured transmitted power through the Fabry-Perot with respect to the tilt angle. The incoming emission is from a single longitudinal mode of a microring laser, and the FP is rotated with the steps of 0.1°. (b) The calculated power in frequency domain showing the laser linewidth of ~10 GHz.

This experiment was performed for a single longitudinal emission from a microring laser. Figure 48(a) shows the measured transmitted power with respect to the Fabry-Perot's angle. The tilt angles marking $\Delta\theta_{FSR}$ shown in the figure can used in conjugation with Eq. (A.4) to find C. This value is then used to calculate the spectrum in Fig. 48(b). The two peaks are representing the two counter propagating modes associated with the involved longitudinal mode. The linewidth of the modes are measured to be ~10 GHz from this resolved spectrum. Figure 49 is depicting the high-resolution spectrum measurement for a single microring and a dark state microring laser arrangements. These measurements also confirm that the laser linewidth is ~10 GHz. Furthermore, Figure 49(b) reveals that the dark state arrangement

operates in a single directional mode fashion at the same pump level that make both CW and CCW modes lase in the single microring.

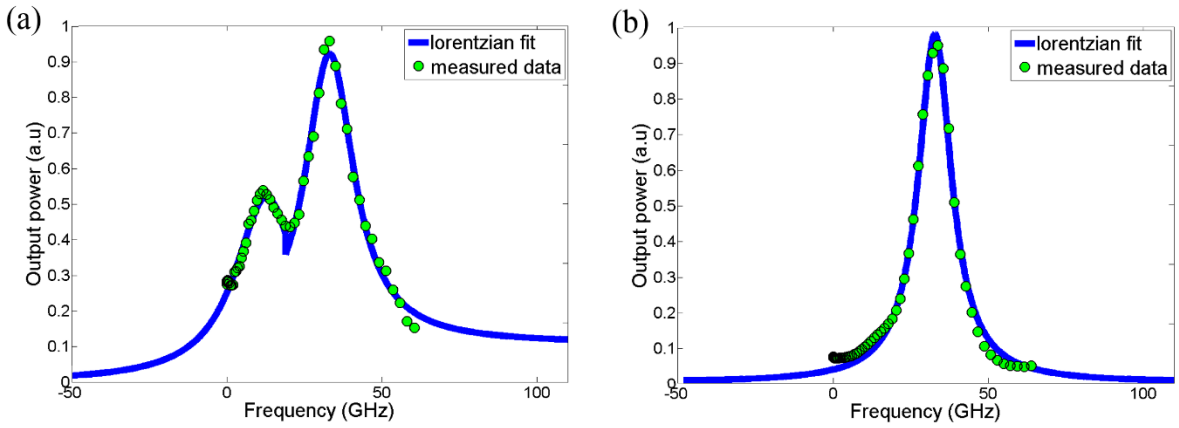

Figure 49. The high resolution measurement of the emission spectrum for (a) a single ring (b) a dark state laser at the same pump powers. The spectra reveals that the laser linewidths are ~10 GHz. The dark state is operating in a single directional mode.

REFERENCES

[1] W. D. Heiss, "Phases of wave functions and level repulsion," *Eur. Phys. J. - At. Mol. Opt. Plasma Phys.*, vol. 7, no. 1, pp. 1–4, Aug. 1999.

[2] M. V. Berry, "Physics of Nonhermitian Degeneracies," *Czechoslov. J. Phys.*, vol. 54, no. 10, pp. 1039–1047, Oct. 2004.

[3] W. D. Heiss, "The physics of exceptional points," *J. Phys. Math. Theor.*, vol. 45, no. 44, p. 444016, 2012.

[4] N. Moiseyev, *Non-Hermitian quantum mechanics*. Cambridge University Press, 2011.

[5] K. G. Makris, R. El-Ganainy, D. N. Christodoulides, and Z. H. Musslimani, "Beam Dynamics in PT Symmetric Optical Lattices," *Phys. Rev. Lett.*, vol. 100, no. 10, p. 103904, Mar. 2008.

[6] A. Guo *et al.*, "Observation of P T-symmetry breaking in complex optical potentials," *Phys. Rev. Lett.*, vol. 103, no. 9, p. 93902, 2009.

[7] Z. Lin, H. Ramezani, T. Eichelkraut, T. Kottos, H. Cao, and D. N. Christodoulides, "Unidirectional invisibility induced by P T-symmetric periodic structures," *Phys. Rev. Lett.*, vol. 106, no. 21, p. 213901, 2011.

[8] L. Feng *et al.*, "Experimental demonstration of a unidirectional reflectionless parity-time metamaterial at optical frequencies," *Nat. Mater.*, vol. 12, no. 2, pp. 108–113, 2013.

[9] B. Peng *et al.*, "Parity-time-symmetric whispering-gallery microcavities," *Nat. Phys.*, vol. 10, no. 5, pp. 394–398, May 2014.

[10] A. Regensburger, C. Bersch, M.-A. Miri, G. Onishchukov, D. N. Christodoulides, and U. Peschel, "Parity-time synthetic photonic lattices," *Nature*, vol. 488, no. 7410, pp. 167–171, 2012.

[11] B. Zhen *et al.*, "Spawning rings of exceptional points out of Dirac cones," *Nature*, vol. 525, no. 7569, pp. 354–358, Sep. 2015.

[12] C. E. Rüter, K. G. Makris, R. El-Ganainy, D. N. Christodoulides, M. Segev, and D. Kip, "Observation of parity–time symmetry in optics," *Nat. Phys.*, vol. 6, no. 3, pp. 192–195, Mar. 2010.

[13] J. Doppler *et al.*, "Dynamically encircling an exceptional point for asymmetric mode switching," *Nature*, vol. 537, no. 7618, pp. 76–79, Sep. 2016.

[14] H. Xu, D. Mason, L. Jiang, and J. G. E. Harris, "Topological energy transfer in an optomechanical system with exceptional points," *Nature*, vol. 537, no. 7618, pp. 80–83, Sep. 2016.

[15] S. L. McCall, A. F. J. Levi, R. E. Slusher, S. J. Pearton, and R. A. Logan, "Whispering-gallery mode microdisk lasers," *Appl. Phys. Lett.*, vol. 60, no. 3, pp. 289–291, 1992.

[16] K. J. Vahala, "Optical microcavities," *Nature*, vol. 424, no. 6950, pp. 839–846, Aug. 2003.

[17] I. Stamataki, S. Mikroulis, A. Kapsalis, and D. Syvridis, "Investigation on the Multimode Dynamics of InGaAsP ndash;InP Microring Lasers," *IEEE J. Quantum Electron.*, vol. 42, no. 12, pp. 1266–1273, Dec. 2006.

[18] D. Liang *et al.*, "Electrically-pumped compact hybrid silicon microring lasers for optical interconnects," *Opt. Express*, vol. 17, no. 22, pp. 20355–20364, Oct. 2009.

[19] A. L. Schawlow and C. H. Townes, "Infrared and Optical Masers," *Phys. Rev.*, vol. 112, no. 6, pp. 1940–1949, Dec. 1958.

[20] L. A. Coldren, S. W. Corzine, and M. L. Mashanovitch, *Diode Lasers and Photonic Integrated Circuits*. John Wiley & Sons, 2012.

[21] M. Asada, A. Kameyama, and Y. Suematsu, "Gain and intervalence band absorption in quantum-well lasers," *IEEE J. Quantum Electron.*, vol. 20, no. 7, pp. 745–753, 1984.

[22] L. Coldren and T. Koch, "Analysis and design of coupled-cavity lasers-Part I: Threshold gain analysis and design guidelines," *IEEE J. Quantum Electron.*, vol. 20, no. 6, pp. 659–670, 1984.

[23] S. Matsuo and T. Segawa, "Microring-resonator-based widely tunable lasers," *IEEE J. Sel. Top. Quantum Electron.*, vol. 15, no. 3, pp. 545–554, 2009.

[24] N. Olsson, W. Tsang, and R. Logan, "Active spectral stabilization of cleaved-coupled-cavity (C 3) lasers," *J. Light. Technol.*, vol. 2, no. 1, pp. 49–51, 1984.

[25] J. C. Hulme, J. K. Doylend, and J. E. Bowers, "Widely tunable Vernier ring laser on hybrid silicon," *Opt. Express*, vol. 21, no. 17, pp. 19718–19722, 2013.

[26] H. Kogelnik and C. V. Shank, "Coupled-wave theory of distributed feedback lasers," *J. Appl. Phys.*, vol. 43, no. 5, pp. 2327–2335, 1972.

[27] M. Nakamura, K. Aiki, J. Umeda, and A. Yariv, "CW operation of distributed-feedback GaAs-GaAlAs diode lasers at temperatures up to 300 K," *Appl. Phys. Lett.*, vol. 27, no. 7, pp. 403–405, 1975.

[28] K. Iga, F. Koyama, and S. Kinoshita, "Surface emitting semiconductor lasers," *IEEE J. Quantum Electron.*, vol. 24, no. 9, pp. 1845–1855, 1988.

[29] T. Chung, A. Rapaport, V. Smirnov, L. B. Glebov, M. C. Richardson, and M. Bass, "Solid-state laser spectral narrowing using a volumetric photothermal refractive Bragg grating cavity mirror," *Opt. Lett.*, vol. 31, no. 2, pp. 229–231, 2006.

[30] A. Arbabi, S. M. Kamali, E. Arbabi, B. G. Griffin, and L. L. Goddard, "Grating integrated single mode microring laser," *Opt. Express*, vol. 23, no. 4, pp. 5335–5347, 2015.

[31] S. F. Liew, B. Redding, L. Ge, G. S. Solomon, and H. Cao, "Active control of emission directionality of semiconductor microdisk lasers," *Appl. Phys. Lett.*, vol. 104, no. 23, p. 231108, 2014.

[32] M. A. Noginov *et al.*, "Demonstration of a spaser-based nanolaser," *Nature*, vol. 460, no. 7259, pp. 1110–1112, Aug. 2009.

[33] R. F. Oulton *et al.*, "Plasmon lasers at deep subwavelength scale," *Nature*, vol. 461, no. 7264, pp. 629–632, 2009.

[34] M. Khajavikhan *et al.*, "Thresholdless nanoscale coaxial lasers," *Nature*, vol. 482, no. 7384, pp. 204–207, 2012.

[35] A. M. Armani, R. P. Kulkarni, S. E. Fraser, R. C. Flagan, and K. J. Vahala, "Label-Free, Single-Molecule Detection with Optical Microcavities," *Science*, vol. 317, no. 5839, pp. 783–787, Aug. 2007.

[36] F. Vollmer and L. Yang, "Review Label-free detection with high-Q microcavities: a review of biosensing mechanisms for integrated devices," *Nanophotonics*, vol. 1, no. 3–4, pp. 267–291, 2012.

[37] S. Ezekiel and S. R. Balsamo, "Passive ring resonator laser gyroscope," *Appl. Phys. Lett.*, vol. 30, no. 9, pp. 478–480, May 1977.

[38] J. Zhu *et al.*, "On-chip single nanoparticle detection and sizing by mode splitting in an ultrahigh-Q microresonator," *Nat. Photonics*, vol. 4, no. 1, pp. 46–49, 2010.

[39] J. Wiersig, "Enhancing the Sensitivity of Frequency and Energy Splitting Detection by Using Exceptional Points: Application to Microcavity Sensors for Single-Particle Detection," *Phys. Rev. Lett.*, vol. 112, no. 20, p. 203901, May 2014.

[40] C. M. Bender and S. Boettcher, "Real spectra in non-Hermitian Hamiltonians having P T symmetry," *Phys. Rev. Lett.*, vol. 80, no. 24, p. 5243, 1998.

[41] C. M. Bender, D. C. Brody, and H. F. Jones, "Complex extension of quantum mechanics," *Phys. Rev. Lett.*, vol. 89, no. 27, p. 270401, 2002.

[42] M. V. Berry, "Optical lattices with PT symmetry are not transparent," *J. Phys. Math. Theor.*, vol. 41, no. 24, p. 244007, 2008.

[43] A. Mostafazadeh, "Pseudo-Hermiticity and generalized PT-and CPT-symmetries," *J. Math. Phys.*, vol. 44, no. 3, pp. 974–989, 2003.

[44] T. Prosen, "P T-Symmetric Quantum Liouvillean Dynamics," *Phys. Rev. Lett.*, vol. 109, no. 9, p. 90404, 2012.

[45] S. Klaiman, U. Günther, and N. Moiseyev, "Visualization of branch points in p t-symmetric waveguides," *Phys. Rev. Lett.*, vol. 101, no. 8, p. 80402, 2008.

[46] G. Castaldi, S. Savoia, V. Galdi, A. Alù, and N. Engheta, "P T Metamaterials via Complex-Coordinate Transformation Optics," *Phys. Rev. Lett.*, vol. 110, no. 17, p. 173901, 2013.

[47] R. El-Ganainy, K. G. Makris, D. N. Christodoulides, and Z. H. Musslimani, "Theory of coupled optical PT-symmetric structures," *Opt. Lett.*, vol. 32, no. 17, pp. 2632–2634, 2007.

[48] Z. H. Musslimani, K. G. Makris, R. El-Ganainy, and D. N. Christodoulides, "Optical Solitons in P T Periodic Potentials," *Phys. Rev. Lett.*, vol. 100, no. 3, p. 30402, 2008.

[49] S. Longhi, "Bloch Oscillations in Complex Crystals with P T Symmetry," *Phys. Rev. Lett.*, vol. 103, no. 12, p. 123601, 2009.

[50] K. G. Makris, R. El-Ganainy, D. N. Christodoulides, and Z. H. Musslimani, "PT-symmetric optical lattices," *Phys. Rev. A*, vol. 81, no. 6, p. 63807, 2010.

[51] M. C. Zheng, D. N. Christodoulides, R. Fleischmann, and T. Kottos, "PT optical lattices and universality in beam dynamics," *Phys. Rev. A*, vol. 82, no. 1, p. 10103, 2010.

[52] H. Ramezani, T. Kottos, R. El-Ganainy, and D. N. Christodoulides, "Unidirectional nonlinear PT-symmetric optical structures," *Phys. Rev. A*, vol. 82, no. 4, p. 43803, 2010.

[53] S. V. Dmitriev, A. A. Sukhorukov, and Y. S. Kivshar, "Binary parity-time-symmetric nonlinear lattices with balanced gain and loss," *Opt. Lett.*, vol. 35, no. 17, pp. 2976–2978, 2010.

[54] T. Kottos, "Optical physics: Broken symmetry makes light work," *Nat. Phys.*, vol. 6, no. 3, pp. 166–167, 2010.

[55] S. Longhi, "Spectral singularities and Bragg scattering in complex crystals," *Phys. Rev. A*, vol. 81, no. 2, p. 22102, 2010.

[56] Y. D. Chong, L. Ge, and A. D. Stone, "P T-Symmetry Breaking and Laser-Absorber Modes in Optical Scattering Systems," *Phys. Rev. Lett.*, vol. 106, no. 9, p. 93902, 2011.

[57] Y. N. Joglekar and J. L. Barnett, "Origin of maximal symmetry breaking in even PT-symmetric lattices," *Phys. Rev. A*, vol. 84, no. 2, p. 24103, 2011.

[58] H. Vemuri, V. Vavilala, T. Bhamidipati, and Y. N. Joglekar, "Dynamics, disorder effects, and PT-symmetry breaking in waveguide lattices with localized eigenstates," *Phys. Rev. A*, vol. 84, no. 4, p. 43826, 2011.

[59] E.-M. Graefe and H. F. Jones, "PT-symmetric sinusoidal optical lattices at the symmetry-breaking threshold," *Phys. Rev. A*, vol. 84, no. 1, p. 13818, 2011.

[60] M.-A. Miri, A. Regensburger, U. Peschel, and D. N. Christodoulides, "Optical mesh lattices with PT symmetry," *Phys. Rev. A*, vol. 86, no. 2, p. 23807, 2012.

[61] L. Chang *et al.*, "Parity-time symmetry and variable optical isolation in active-passive-coupled microresonators," *Nat. Photonics*, vol. 8, no. 7, pp. 524–529, Jul. 2014.

[62] M. Liertzer, L. Ge, A. Cerjan, A. D. Stone, H. E. Türeci, and S. Rotter, "Pump-induced exceptional points in lasers," *Phys. Rev. Lett.*, vol. 108, no. 17, p. 173901, 2012.

[63] S. Longhi, "PT-symmetric laser absorber," *Phys. Rev. A*, vol. 82, no. 3, p. 31801, 2010.

[64] M.-A. Miri, P. LiKamWa, and D. N. Christodoulides, "Large area single-mode parity–time-symmetric laser amplifiers," *Opt. Lett.*, vol. 37, no. 5, pp. 764–766, 2012.

[65] M. Kulishov and B. Kress, "Distributed Bragg reflector structures based on PT-symmetric coupling with lowest possible lasing threshold," *Opt. Express*, vol. 21, no. 19, pp. 22327–22337, 2013.

[66] M. Brandstetter *et al.*, "Reversing the pump dependence of a laser at an exceptional point," *Nat. Commun.*, vol. 5, p. 4034, Jun. 2014.

[67] B. Peng *et al.*, "Loss-induced suppression and revival of lasing," *Science*, vol. 346, no. 6207, pp. 328–332, Oct. 2014.

[68] Q. Xu, B. Schmidt, S. Pradhan, and M. Lipson, "Micrometre-scale silicon electro-optic modulator," *Nature*, vol. 435, no. 7040, pp. 325–327, May 2005.

[69] P. Dong *et al.*, "Wavelength-tunable silicon microring modulator," *Opt. Express*, vol. 18, no. 11, pp. 10941–10946, May 2010.

[70] F. Y. Gardes *et al.*, "High-speed modulation of a compact silicon ring resonator based on a reverse-biased pn diode," *Opt. Express*, vol. 17, no. 24, pp. 21986–21991, Nov. 2009.

[71] R. Grover, T. A. Ibrahim, S. Kanakaraju, L. Lucas, L. C. Calhoun, and P. T. Ho, "A tunable GaInAsP-InP optical microring notch filter," *IEEE Photonics Technol. Lett.*, vol. 16, no. 2, pp. 467–469, Feb. 2004.

[72] B. E. Little *et al.*, "Ultra-compact Si-SiO2 microring resonator optical channel dropping filters," *IEEE Photonics Technol. Lett.*, vol. 10, no. 4, pp. 549–551, Apr. 1998.

[73] B. E. Little *et al.*, "Very high-order microring resonator filters for WDM applications," *IEEE Photonics Technol. Lett.*, vol. 16, no. 10, pp. 2263–2265, Oct. 2004.

[74] H. Hodaei *et al.*, "Parity-time-symmetric coupled microring lasers operating around an exceptional point," *Opt. Lett.*, vol. 40, no. 21, pp. 4955–4958, 2015.

[75] H. Hodaei *et al.*, "Design Considerations for Single-Mode Microring Lasers Using Parity-Time-Symmetry," *IEEE J. Sel. Top. Quantum Electron.*, vol. 22, no. 5, pp. 1–7, 2016.

[76] E. A. Ultanir, D. Michaelis, F. Lederer, and G. I. Stegeman, "Stable spatial solitons in semiconductor optical amplifiers," *Opt. Lett.*, vol. 28, no. 4, pp. 251–253, Feb. 2003.

[77] A. U. Hassan, H. Hodaei, M.-A. Miri, M. Khajavikhan, and D. N. Christodoulides, "Nonlinear reversal of the PT-symmetric phase transition in a system of coupled semiconductor microring resonators," *Phys. Rev. A*, vol. 92, no. 6, p. 63807, 2015.

[78] H. Hodaei, M.-A. Miri, M. Heinrich, D. N. Christodoulides, and M. Khajavikhan, "Parity-time–symmetric microring lasers," *Science*, vol. 346, no. 6212, pp. 975–978, Nov. 2014.

[79] H. Hodaei *et al.*, "Single mode lasing in transversely multi-moded PT-symmetric microring resonators," *Laser Photonics Rev.*, vol. 10, no. 3, pp. 494–499, 2016.

[80] M. Mikulla *et al.*, "High-brightness tapered semiconductor laser oscillators and amplifiers with low-modal gain epilayer-structures," *IEEE Photonics Technol. Lett.*, vol. 10, no. 5, pp. 654–656, 1998.

[81] J. J. Plant, P. W. Juodawlkis, R. K. Huang, J. P. Donnelly, L. J. Missaggia, and K. G. Ray, "1.5-μm InGaAsP-InP slab-coupled optical waveguide lasers," *IEEE Photonics Technol. Lett.*, vol. 17, no. 4, pp. 735–737, 2005.

[82] J. N. Walpole, "Semiconductor amplifiers and lasers with tapered gain regions," *Opt. Quantum Electron.*, vol. 28, no. 6, pp. 623–645, 1996.

[83] J. N. Walpole *et al.*, "Slab-coupled 1.3-μm semiconductor laser with single-spatial large-diameter mode," *IEEE Photonics Technol. Lett.*, vol. 14, no. 6, pp. 756–758, 2002.

[84] C. M. Gentry and M. A. Popović, "Dark state lasers," *Opt. Lett.*, vol. 39, no. 14, pp. 4136–4139, Jul. 2014.

[85] H. Hodaei, A. U. Hassan, W. E. Hayenga, M. A. Miri, D. N. Christodoulides, and M. Khajavikhan, "Dark-state lasers: mode management using exceptional points," *Opt. Lett.*, vol. 41, no. 13, pp. 3049–3052, 2016.

[86] B. E. Little, S. T. Chu, H. A. Haus, J. Foresi, and J. P. Laine, "Microring resonator channel dropping filters," *J. Light. Technol.*, vol. 15, no. 6, pp. 998–1005, Jun. 1997.

[87] Z.-P. Liu *et al.*, "Metrology with PT-Symmetric Cavities: Enhanced Sensitivity near the PT-Phase Transition," *Phys. Rev. Lett.*, vol. 117, no. 11, p. 110802, Sep. 2016.

[88] J. Wiersig, "Sensors operating at exceptional points: General theory," *Phys. Rev. A*, vol. 93, no. 3, p. 33809, Mar. 2016.

[89] G. Demange and E.-M. Graefe, "Signatures of three coalescing eigenfunctions," *J. Phys. Math. Theor.*, vol. 45, no. 2, p. 25303, 2012.

[90] W. D. Heiss and G. Wunner, "Resonance scattering at third-order exceptional points," *J. Phys. Math. Theor.*, vol. 48, no. 34, p. 345203, 2015.

[91] Z. Lin, A. Pick, M. Lončar, and A. W. Rodriguez, "Enhanced Spontaneous Emission at Third-Order Dirac Exceptional Points in Inverse-Designed Photonic Crystals," *Phys. Rev. Lett.*, vol. 117, no. 10, p. 107402, Aug. 2016.

[92] M. H. Teimourpour, R. El-Ganainy, A. Eisfeld, A. Szameit, and D. N. Christodoulides, "Light transport in PT-invariant photonic structures with hidden symmetries," *Phys. Rev. A*, vol. 90, no. 5, p. 53817, 2014.